CRYOGENIC FIBRE-FED LASER METROLOGY

ADAM CHRISTIANSEN
Bachelor of Science, University of Alberta, 2018

A thesis submitted
in partial fulfilment of the requirements for the degree of

MASTER OF SCIENCE

in

INDIVIDUALIZED MULTIDISCIPLINARY

Department of Physics and Astronomy
University of Lethbridge
LETHBRIDGE, ALBERTA, CANADA

CRYOGENIC FIBRE-FED LASER METROLOGY

ADAM CHRISTIANSEN

Date of Defence: August 20, 2020

Dr. David Naylor Thesis Supervisor	Professor	Ph.D.
Dr. Jacqueline Rice Thesis Examination Committee Member	Professor	Ph.D.
Dr. Locke Spencer Thesis Examination Committee Member	Associate Professor	Ph.D.
Dr. Chad Povey Chair, Thesis Examination Committee	Instructor	Ph.D.

Abstract

Cryogenic cooling is a fundamental requirement for broadband far-infrared spectroscopic instrumentation to benefit from state-of-the-art far-infrared detectors. The precision to which the moving cryogenic components of the instrument can be measured and controlled affects its ability to recover the spectrum and exacts a low power robust position metrology system. This thesis explores a number of laser-based position metrology solutions and shows that a fibre-fed range-resolved interferometer meets the stringent precision and low power requirements of a metrology system for future space missions. Two cryogenic fibre-fed range-resoled interferometers are theoretically discussed and subsequently constructed; the first using the Clarke transform to decode three-phase signals, and the second based on sinusoidal laser frequency modulation. Experimental results of room and cryogenic ($< 4\,\mathrm{K}$) temperature testing for both systems are presented. Lessons learned, suggested improvements, and the employment of a range-resolved interferometer for cryogenic accelerometry, lunar seismology, and other applications are discussed.

Acknowledgments

When I was an undergraduate studying computer engineering at the University of Alberta, I was in search of a job for my first cooperative work term. Prof. Alexandra Pope recommended Blue Sky Spectroscopy Inc. to hire me for a summer position, where I spent my summer and my interest in experimental physics was spawned. Alexandra introduced me to my future supervisor, Prof. David Naylor, and my career was started. Before completing my undergraduate degree, I worked another cooperative job under David's supervision, who inspired me to turn my career path toward experimental physics.

The completion of the work presented in this thesis required multiple iterations of refinement. My thesis examination committee, consisting of Prof. David Naylor, Prof. Jacqueline Rice, and Prof. Locke Spencer, all provided valuable discussions, suggestions, and improvements. As the thesis examination date coincided with the wedding anniversary of Dr. Chad Povey, who served as the chair of the thesis examination committee, he generously gave his time on this day to preside over the event.

I was not well equipped to conduct cryogenic testing on my own and was only able to do so with the guidance of Dr. Ian Veenendaal, Dr. Sudhakar Gunuganti, and Brad Gom. They not only provided a helping hand, but trained me the best practices. Likewise, Rebecca Sirota and Kalle Kiiskinen contributed the design and construction of the electronic circuits, which I could not have completed alone. Gregory Tompkins provided with me with useful, if not controversial, training on practical electronics.

Experimental collaborations with Prof. Locke Spencer, Vincent Weiler, and Geof-

frey Sitwell in the cryogenic testing of coefficients of thermal expansion led to valuable experience, feedback, and data. Vincent and I had many mutually beneficial discussions on programming and field-programmable gate arrays.

The New Telescopes for Canadian Observatories programme provided support in numerous ways and allowed me unique opportunities for training and networking in fields related to astronomy and astronomical instrumentation. In order to fulfill the programme requirements, I worked at Blue Sky Spectroscopy Inc., where I worked closely with and learned from Dr. Sudhakar Gunuganti. Prof. Laurent Drissen and Prof. Suresh Sivanandam served as my programme co-supervisors, who ensured that I was being trained in skills that will suit me for a future in astronomical instrumentation.

My friends and family, who may not have always understood what exactly I was doing, always believed that I will accomplish the extraordinary. My parents, Suzy and Darryl Christiansen, were invaluable to me. Their love and support outside of the laboratory allowed me to focus on my studies and achieve the best that I possibly could.

To everyone who has influenced this work in ways large or small, thank you.

Contents

List of Tables

List of Figures

List of Abbreviations

AC	alternating current
ADC	analog-to-digital converter
BRAM	block random access memory
CFRP	carbon fibre reinforced polymer
CORDIC	coordinate rotation digital computer
CTE	coefficient of thermal expansion
CW	continuous wave
DAC	digital-to-analog converter
DC	direct current
DFB	distributed feedback
DSP	digital signal processing
DTFT	discrete-time Fourier transform
ESA	European Space Agency
FC/APC	ferrule-connector angled physical contact
FC/PC	ferrule-connector physical contact
FF	flip-flop
FIFO	first-in first-out
FIR	finite impulse response
FPGA	field-programmable gate array
FSR	full-scale range
FTS	Fourier transform spectrometer
HeNe	helium-neon
IIR	infinite impulse response
ISO	Infrared Space Observatory
JAXA	Japan Aerospace Exploration Agency
JWST	James Webb Space Telescope
LIGO	Laser Interferometer Gravitational-Wave Observatory

LUT	look-up table
LVDT	linear variable differential transformer
MPSoC	multi-processor system-on-chip
MUX	multiplexer
NASA	National Aeronautics and Space Administration
OPD	optical path difference
PC	personal computer
RAM	random access memory
RTOS	real-time operating system
SAFARI	SPICA Far-Infrared Instrument
SNR	signal-to-noise ratio
SPICA	Space Infrared telescope for Cosmology and Astrophysics
USB	Universal Serial Bus
WDM	wave division multiplexer
ZPD	zero path difference

List of Notations

A	area
B	spectrum
$\vec{B}$	magnetic field
C	capacitance
c	vacuum speed of light
$\mathcal{C}$	complex carrier signal
d	distance
Δt	time interval
Δx	linear displacement
$\Delta\phi$	phase difference
δ_{k0}	Kronecker delta function
$\delta\Delta x$	displacement uncertainty
$\delta\lambda$	wavelength uncertainty
$\delta\phi_{\mathrm{b}}$	leading three-phase signal phase uncertainty
$\delta\phi_{\mathrm{c}}$	lagging three-phase signal phase uncertainty
$\delta\phi_{\mathrm{q}}$	quadrature encoded phase uncertainty
E	energy
E_{g}	gap energy
E_{photon}	photon energy
$\vec{E}$	electric field
e	Euler's number
ϵ	permittivity of an isotropic medium
ϵ_0	vacuum permittivity
f	focal length, generic time varying function, generic frequency
f_{co}	cut-off frequency
f_{m}	modulation frequency
f_{fr}	fringe rate
f_{s}	sampling frequency
$\mathcal{F}$	Fourier transform
H	frequency response

h	Planck's constant
h	unit impulse response
η_{12}	circulator efficiency through the first and second arms
η_{23}	circulator efficiency through the second and third arms
η_{eff}	effective interferometer efficiency
η_{r}	interferometer reflection efficiency
I	intensity, generic current, interferogram
I_0	Gaussian beam intensity at the waist centre
I_{a}	reference three-phase electrical current
I_{b}	leading three-phase electrical current
I_{c}	lagging three-phase electrical current
I_{max}	maximum fringe intensity
I_{min}	minimum fringe intensity
I_{n}	neutral three-phase electrical current
j	imaginary unit
k	angular spatial frequency
$\vec{k}$	angular spatial frequency vector
L	length, inductance
LP	low-pass filter
Λ	optical path difference
Λ_0	centre optical path difference
λ	vacuum wavelength of light
λ_{c}	centre vacuum wavelength of a modulated laser
M	lens magnification, mutual inductance
m	generic integral index
μ	permeability of an isotropic medium
μ_0	vacuum permeability
N	generic integral constant, moving average filter width
n	refractive index, discrete-time signal index
ν	optical frequency
ν_{A}	optical frequency modulation amplitude
ν_{c}	centre optical frequency of a modulated laser
P	optical power
P_{12}	optical power transmitted through first and second circulator arms
P_{23}	optical power transmitted through second and third circulator arms
P_{laser}	optical power of a laser

P_{pd}	optical power measured at a photodetector
$P_{\mathcal{R}}$	reflected optical power
$P_{\mathcal{R},\mathrm{corr}}$	corrected reflected optical power
$P_{\mathcal{T}}$	transmitted optical power
$P_{\mathcal{T},\mathrm{corr}}$	corrected transmitted optical power
ϕ	generic phase term
ϕ_{b}	phase of the leading three-phase signal
ϕ_{c}	phase of the lagging three-phase signal
ϕ_{q}	quadrature encoded phase
ϕ_{Λ}	OPD dependent phase
Ψ	generic wave
R	Gaussian beam radius of curvature, electrical resistance
$\vec{r}$	position vector
ρ	radius from optical axis, resistivity
$\mathcal{R}$	reflectance
$\mathcal{R}_{\mathrm{opt}}$	optimal reflectance
$\vec{S}$	Poynting vector
σ	Gaussian window standard deviation, wavenumber
T	period
T_{m}	modulation period
$T_{\alpha\beta 0}$	Clarke transform
t	time
τ_{d}	demodulation delay
τ_{f}	interferometer time of flight delay
τ_{sig}	signal processing delay
θ_{A}	phase modulation amplitude
θ_{D}	phase demodulation amplitude
θ_{m}	phase modulation function
$\mathcal{T}$	transmittance
$\mathcal{T}_{\mathrm{opt}}$	optimal transmittance
U_0	three-phase zero quadrature signal
U_{a}	reference three-phase signal
U_{b}	leading three-phase signal
U_{c}	lagging three-phase signal
U_{d}	complex demodulated signal
$U_{\mathrm{el,gn,a}}$	reference three-phase electrical gain
$U_{\mathrm{el,gn,b}}$	leading three-phase optical electrical gain
$U_{\mathrm{el,gn,c}}$	lagging three-phase electrical gain
$U_{\mathrm{el,gn},x}$	arbitrary three-phase electrical gain

$U_{\mathrm{el,of,a}}$	reference three-phase electrical offset
$U_{\mathrm{el,of,b}}$	leading three-phase electrical offset
$U_{\mathrm{el,of,c}}$	lagging three-phase electrical offset
$U_{\mathrm{el,of},x}$	arbitrary three-phase electrical offset
U_{fm}	normalized frequency modulation signal
$U_{\mathrm{op,at}}$	optical attenuation envelope
$U_{\mathrm{op,co,at,a}}$	reference three-phase optical coupling attenuation
$U_{\mathrm{op,co,at,b}}$	leading three-phase optical coupling attenuation
$U_{\mathrm{op,co,at,c}}$	lagging three-phase optical coupling attenuation
$U_{\mathrm{op,co,at},x}$	arbitrary three-phase optical coupling attenuation
$U_{\mathrm{op,of}}$	three-phase optical offset
U_{q}	complex quadrature signal
U_x	arbitrary three-phase signal
U_α	three-phase reference quadrature signal
U_β	three-phase lagging quadrature signal
u	energy density
V	voltage, volume
V_{CC}	positive voltage supply rail
V_{EE}	negative voltage supply rail
$V_{I,\mathrm{max}}$	photodetector voltage at maximum fringe intensity
$V_{I,\mathrm{min}}$	photodetector voltage at minimum fringe intensity
V_{bias}	laser bias voltage
V_{pd}	amplified frequency modulation photodetector voltage
v	velocity
v_{max}	maximum interferometer translation velocity
$\mathcal{V}$	visibility
W	Gaussian beam radius
W_0	Gaussian beam waist radius
W_G	Gaussian window function
ω	angular frequency
x	discrete-time system input signal
y	discrete-time system output signal
z	optical axis
z_0	Rayleigh range
ζ	Gouy phase
$\mathbb{Z}$	set of integers

Chapter 1

Introduction

Space-based far-infrared telescopes employing Fourier transform spectrometers (FTS) require precise knowledge of the instrument optical path difference (OPD). The intensity of the spectrum, $B(\sigma)$, is related to the interferogram, I, by the Fourier transform:

$$B(\sigma) = \int_{-\infty}^{\infty} I(\Lambda) \mathrm{e}^{-j2\pi\sigma\Lambda}\, d\Lambda, \qquad [\mathrm{W\,m^{-2}\,cm^{-1}}] \quad (1.1)$$

where σ is the wavenumber in cm^{-1}, I is the interferogram, and j is the imaginary unit. The interferogram is measured as a function of the OPD of two interfering beams in the interferometer, necessitating precision position metrology in order to recover the spectrum by Equation 1.1.

The sensitivity of state-of-the-art infrared detectors is such that future infrared space missions require that the entire instrument, including primary and secondary telescope mirrors, be cryogenically cooled. Due the difficulty of reaching cryogenic temperatures, it is critical to employ a position metrology system that can not only precisely measure the FTS OPD at $< 4\,\mathrm{K}$, but do so with minimal thermal power dissipation. In this thesis, I set out to construct and evaluate a cryogenic range-resolved interferometer that meets the demanding performance and power requirements of cryogenic far-infrared space missions under development.

1.1 The SPICA SAFARI Instrument

The Space Infrared telescope for Cosmology and Astrophysics (SPICA) is an observatory-class mission led by European Space Agency (ESA) and Japan Aerospace Exploration Agency (JAXA) to study the formation and evolution of galaxies, black holes, and planetary systems by providing imaging spectroscopy and polarimetry over the 5 µm to 230 µm range [1]. The SPICA Far-Infrared Instrument (SAFARI) is one of three instruments on board SPICA and is responsible for the far-infrared range of 34 µm to 230 µm. In order to exploit the sensitivity of state-of-the-art far-infrared detectors, the instrumentation on board SPICA must be cryogenically cooled. In the case of SPICA, there will be three distinct temperature zones: $< 8\,\mathrm{K}$ for the telescope optics, which include the primary and secondary mirrors; $< 4\,\mathrm{K}$ for the instrumentation, and $\sim 50\,\mathrm{mK}$ for the detectors.

SAFARI is an FTS with a linear translation stage that requires position metrology with an accuracy of 10 nm rms in a 20 Hz bandwidth over a 33.5 mm mechanical range [2]. SAFARI falls into the $< 4\,\mathrm{K}$ temperature regime, and is allotted a total thermal power budget of 1.5 mW, which includes measurement, control, and actuation of moving components, and it is expected that at most 10 % of the thermal power budget will be consumed by the position metrology system, which corresponds to $< 0.15\,\mathrm{mW}$ thermal power dissipation. Under these constraints, a frequency modulation range-resolved interferometer has been adopted for SAFARI.

1.2 Thesis Overview

This thesis begins with a literature review of cryogenic position metrology techniques and applications in previous space missions. In Chapter 2, a comparison of the pros and cons of each technique illustrates that a range-resolved interferometer is the only practical solution for SAFARI. Chapter 3 introduces the key features to consider for a fibre-fed range-resolved interferometer, a range-resolved interferometer,

which covers topics from optics, signal processing, and field-programmable gate array (FPGA) programming.

Two techniques for cryogenic range-resolved interferometry are explored in Chapters 4 and 5, which present both the theory and experimental verification of the techniques and their limitations. A cryogenic range-resolved three-phase laser interferometer is presented in Chapter 4, which evolved to support differential measurement. The three-phase approach performed well when measuring changes in OPD that occur in short time intervals, but proved to be unreliable for measuring small changes that occurred over longer durations. To address this limitation, I arrived at the cryogenic sinusoidal laser frequency modulation interferometer presented in Chapter 5, which is the approach adopted by SAFARI.

Finally, Chapter 6 concludes by summarizing my findings and providing an outlook into future work and applications. The selection of the frequency modulation interferometer for future projects is discussed along with suggested improvements. The novel application of a range-resolved laser frequency modulation interferometer in cryogenic environments is not only useful for space missions such as SPICA SAFARI, but for any application involving very cold temperatures. Cryogenic material properties testing (such as coefficient of thermal expansion (CTE) and Young's modulus) and three-axis cryogenic accelerometry with the potential for lunar deployment are discussed as prospective applications.

Chapter 2

Review of Position Metrology Techniques

A range of position metrology systems have been employed in cryogenic applications, which include resistive, capacitive, eddy current, linear variable differential transformer (LVDT), optical encoder, and interferometric techniques. In this chapter, each of these techniques is reviewed and compared against the SAFARI metrology requirement presented in Section 1.1. The chapter concludes with a summary table that compares the different metrology techniques.

2.1 Resistive Sensors

The electrical resistance of a wire depends on both its geometry and the material from which it is made. A wire of length L, with cross-sectional area A, made of a material whose resistivity is ρ, has a resistance, R, described by

$$R = \frac{\rho L}{A}. \qquad [\Omega] \quad (2.1)$$

The simplest way to modify the resistance of a wire is to change its geometry. In order to measure a mechanical displacement, Δx, a force must be applied along the wire axis causing strain which results in a new wire length of $L + \Delta x$, which by Equation 2.1, effects a change in the resistance of the wire. The resistance changes according to the gauge factor, which is the ratio of the fractional change in resistance

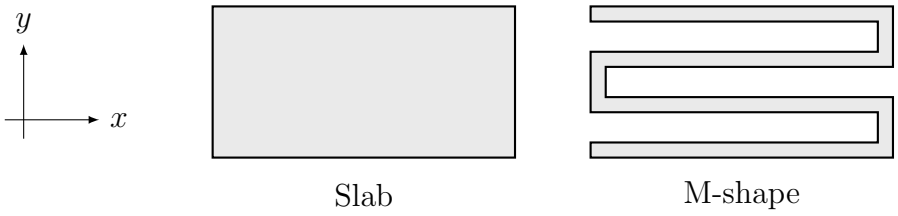

Figure 2.1: Example resistive strain gauge conductor shapes.

to the fractional change in length.

Displacement sensors which measure mechanically induced changes in resistance are called strain gauges. Early strain gauges manufactured by laminating a thin metal film between two insulating sheets were capable of measuring up to a 1 % change in length, which is commonly expressed as 10 000 µstrain [3]. Film shape selection allows the strain gauge to achieve directional sensitivity. Figure 2.1 shows two possible conductor shapes. The slab sensor is sensitive to strain in both the x- and y-directions, since it has sufficient material to see elongation in both directions when orthogonal forces are applied. However, the M-shaped conductor exhibits higher sensitivity in the x-direction. When a force is applied in the x-direction, the length of each linear conductive segment will increase, thus the resistance increases. Conversely, a force applied in the y-direction will act to stretch the film, having relatively little effect on the overall wire length and resistance.

Unlike thin film sensors which can only respond to forces that modify the overall device shape, semiconductor piezoresistive strain sensors are capable of measurement without deformation. Piezoresistive strain sensors are designed using an n-type resistor on a p-type substrate and exhibit up to two orders of magnitude greater sensitivity than metal film sensors [4,5]. When the resistor is elongated, the resistance is reduced as electron mobility increases. The opposite effect can be achieved by using a p-type resistor on an n-type substrate, which will increase in resistance with elongation similar to metal film strain gauges. Metal film strain gauges are better suited to measure

elongation than compression, however, as piezoresistive sensors do not require deformation, they are capable of measuring both with up to 1000 µstrain [3].

Resistive sensors provide high resolution measurements over small full-scale ranges (FSR) of up to 500 µm. Resolutions of 23 nm are achieved by metal film strain gauges and 0.5 nm by piezoresistive sensors. The accuracy of both sensor types is approximately 1 % FSR, which corresponds to 5 µm at the maximum FSR. Film strain gauges are capable of up to 10 kHz bandwidth, while piezoresistive sensors can exceed 100 kHz [3, 4].

Since a strain gauge is a resistor, the power dissipation increases with the square of the current. Although strain gauges can handle up to 100 mW power dissipation, in practice, the power dissipation is lower as manufacturers recommend a selection of current based on the maximum tolerable self-heating in an application [3]. For cryogenic operation, selecting a high resistance strain gauge will reduce the required current. A 10 kΩ strain gauge with a gauge factor of 100 can be operated with 0.1 mA which dissipates only 0.1 mW of power and will have a 100 mV change in output voltage under 1000 µstrain.

The small size of resistive sensors allows them to be bonded directly to the surface of a moving object. Installing the sensor in this way introduces very little overhead in a cryogenic environment, as it is a small mass that can be affixed with sufficient thermal contact. However, the small sensor size is limiting for many applications and is not suitable for typical infrared spectrometer designs. When cooling a strain gauge, changes in the sensor size due to thermal contraction can introduce spurious strain that leads to false readings. If position measurement is required during thermocycling then spurious strain is problematic, but is not an issue if measurement is required only at the target temperature.

Ferrero *et al.* [6] report on the calibration of strain gauges constructed with copper, aluminum, and stainless steel support materials to temperatures of 4.2 K. Gauge

factors varied from 1 % to 5 % for different types of strain sensors when cooling from room temperature to 77 K, and less than 1 % from 77 K to 4.2 K. The apparent strain on the sensor decreased when cooling to $\sim$ 20 K, then inverted and increased with further cooling. Effects in apparent strain at cryogenic temperatures led to the development of special strain gauges for cryogenic applications, such as the HBM C series strain gauges which use a chromium-nickel alloy [7].

2.2 Capacitive Sensors

The capacitance, C, of a capacitor with a dielectric medium of permittivity, ϵ, between two parallel conducting plates each with area, A, separated by a distance, d, is given by

$$C = \frac{\epsilon A}{d}. \qquad [\mathrm{F}] \quad (2.2)$$

A capacitive displacement sensor is a variable capacitor whose capacitance is dependent on the mechanical position of an object. It follows from Equation 2.2 that there are three ways to vary capacitance with mechanical displacement, Δx, which are illustrated in Figure 2.2. Ignoring edge effects, the moving dielectric, lateral moving plate, and axial moving plate configurations vary ϵ, A, and d, respectively. Applications that can maintain plate alignment over the full range of Δx can best make use

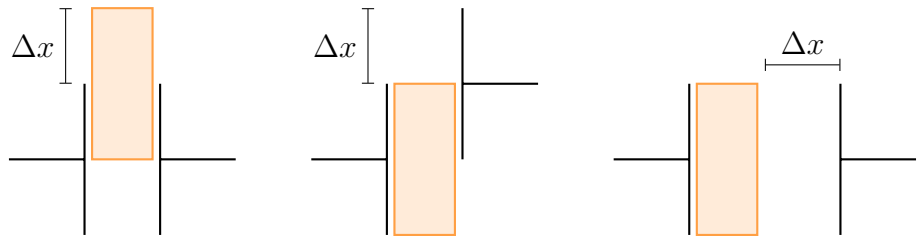

Figure 2.2: Three possible configurations for capacitive sensors illustrating how a displacement, Δx, is measured.

of the axial moving plate configuration, which offers the greatest accuracy. However, accuracy is paid for by a reduced FSR, making moving dielectric and lateral moving plate sensors better suited to longer range applications [4].

The largest capacitive sensors achieve FSRs of up to 10 mm. Although extremely sensitive capacitance micrometers have made measurements of 10^{-14} m [8] — four orders of magnitude smaller than the diameter of an atom — practical capacitive sensors have an accuracy of 5 ppm FSR. Commercially available devices offer sub-nanometre resolution and bandwidths up to 100 kHz [4, 9]. There is zero power dissipated at the point of measurement [8], and all power dissipation is due to the signal conditioning electronics, which is typically ≥ 1 W for commercially available systems [10, 11].

Nearby electric fields affect the operation of capacitive sensors, and typically guard electrodes are placed around the capacitor to mitigate external field effects and improve linearity. Accumulation of contaminants in the capacitor air-gap, such as dirt and dust, can alter the dielectric constant and affect accuracy and linearity [12]. Preventative measures can be taken to prevent contaminant buildup, such as keeping the sensor in a clean environment or a sealed housing. Some may view the use of a housing as an additional requirement, but this is standard practice in space applications.

Under ideal conditions, capacitive sensors exhibit high linearities on the order of the 0.001 % [4]. However, non-linearities can be introduced by many sources, although primarily through tilting and bowing of the plates due to mounting stress [4, 8]. Tilting is when the parallelism of the plates is not maintained, and bowing refers to effects in the plate geometry, such as undesired curvature. All sensor configurations in Figure 2.2 exhibit similar sensitivities to tilt deformities. The lateral moving plate configuration is most sensitive to bowing, since both the distance and angle between the plates changes as a function of Δx. Effects of tilting and bowing can be minimized by increasing the gap distance, at the cost of reduced accuracy due to an increase in noise.

The Infrared Space Observatory (ISO) employed capacitance micrometry in the control of its cryogenic Fabry-Pérot etalons [13–15]. Four Fabry-Pérot interferometers were flown onboard ISO: two in the Short-Wavelength Spectrometer and two in the Long-Wavelength Spectrometer. The two interferometers in the Long-Wavelength Spectrometer, the FPS and FPL, had $\leq 22.4\,\text{nm}$ resolution at an FSR of $91.8\,\mu\text{m}$ and $\leq 29.8\,\text{nm}$ resolution at an FSR of $122.2\,\mu\text{m}$, respectively. This performance was achieved with both instruments cooled to $\sim 3.2\,\text{K}$.

2.3 Eddy Current Sensors

Lenz's law states that the direction of an induced current in a conductor, I_{ind}, resulting from a change in magnetic field, $d\vec{B}_{\text{mag}}/dt$, is such that the magnetic field, $\vec{B}_{\text{ind}}$ created by I_{ind} opposes the change [16]. Although Lenz's law provides only a qualitative description of the induced current and magnetic field directions, it is sufficiently descriptive for an analysis of eddy current sensors, which rely on the phenomenon of magnetic induction. Figure 2.3 illustrates Lenz's law for three cases. When the magnet is stationary relative to the conducting sheet, no current is induced as there is no change in the magnetic flux through the conductor. However, when the distance between the conductor and the magnet changes, a current is induced to create a magnetic field opposite to $d\vec{B}_{\text{mag}}/dt$. In the case that the magnet moves toward the conductor, the magnetic flux through the conductor increases, causing the induction of a current such that $\vec{B}_{\text{ind}}$ is directed opposite to $\vec{B}_{\text{mag}}$, which compensates for the increase. Conversely, the direction of $\vec{B}_{\text{ind}}$ is the same as that of $\vec{B}_{\text{mag}}$ as the magnet moves away in response to the decrease in magnetic flux through the conductor.

Commercial eddy current sensors are available with FSRs of approximately $100\,\mu\text{m}$ up to $80\,\text{mm}$. Resolutions of $10\,\text{nm}$ are possible with FSRs of approximately $250\,\mu\text{m}$, while larger sensors with FSRs of $80\,\text{mm}$ only achieve $4\,\mu\text{m}$ resolution. Overall, this is an accuracy of approximately $0.1\,\%$ FSR at lower bandwidths, which can reach up to

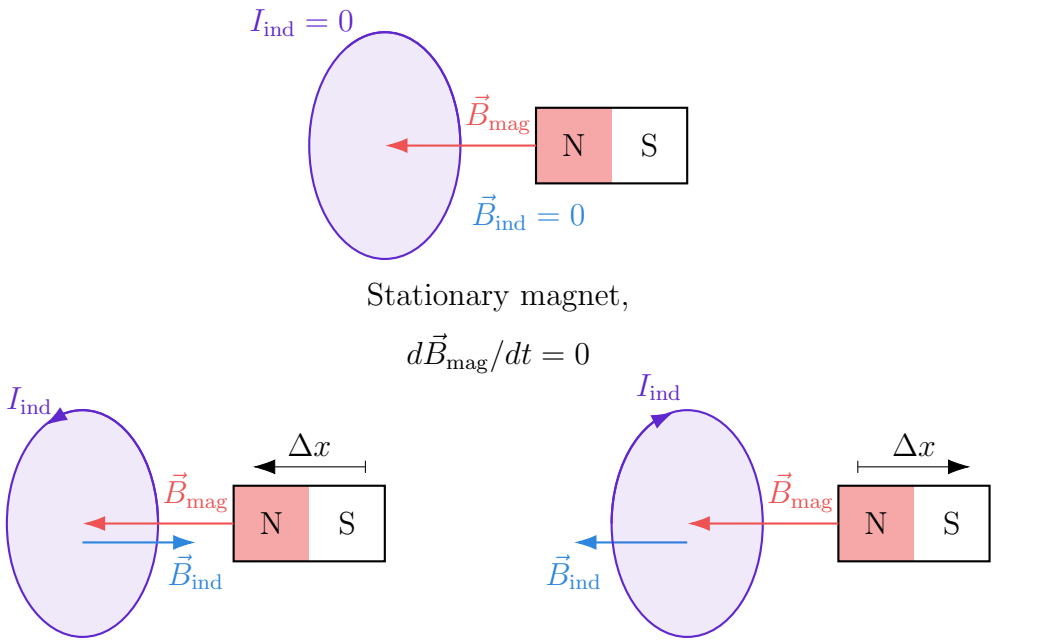

Figure 2.3: Eddy currents created in a conductive sheet using a bar magnet.

100 kHz [4, 17, 18]. Commercially available eddy current sensors dissipate 12 mW [19] to 750 mW [20] of power.

Contactless sensors are prone to contaminants, such as dirt and dust, which can accumulate in the sensor cavities. As eddy current sensors rely on magnetic fields, they are sensitive to nearby current carrying conductors, but relatively unaffected by contamination when compared to capacitive sensors [4]. However, when used cryogenically in a vacuum, contamination is generally not an issue.

Eddy current sensors may be influenced by the presence of external magnetic fields and certain types of materials. Sensors with housings fashioned from ferrous materials, such as steel, can see a factor of ~ 2 reduction in resolution compared to their non-ferrous counterparts [18]. Even sensors constructed from aluminum and other non-ferrous metals are vulnerable to magnetic field exposure, which can lead to poor performance in some applications. Sensors based on electrical currents have the

potential for Joule heating, whose effects can contribute thermal power in excess of the limits set for a cryogenic system.

Cassini's Composite Infrared Spectrometer [21] employed a differential eddy current sensor at 170 K [22] for the linear scan mechanism of its Fourier Transform spectrometer. The sensor operated over a displacement range of 15 mm and reported $< 1\,\%$ resolution.

Sagar *et al.* report on a multilayer eddy current sensor achieving an accuracy of 1.84 µm over a range of 5 mm at 4.2 K [23].

2.4 Linear Variable Differential Transformers

The LVDT is another type of inductive sensor, illustrated in Figure 2.4, in which the couplings between inductive coils of a transformer are changed by the position of a conductive core. The left loop of Figure 2.4 is comprised of an exciting AC voltage source, V_s, which powers an inductive coil, L_s, to produce a magnetic field. There exist mutual inductances between L_s, L_1, and L_2, which will be named $M_1 = \sqrt{L_s L_1}$ and $M_2 = \sqrt{L_s L_2}$. The mutual inductance $M_{12} = \sqrt{L_1 L_2}$ will be omitted from this

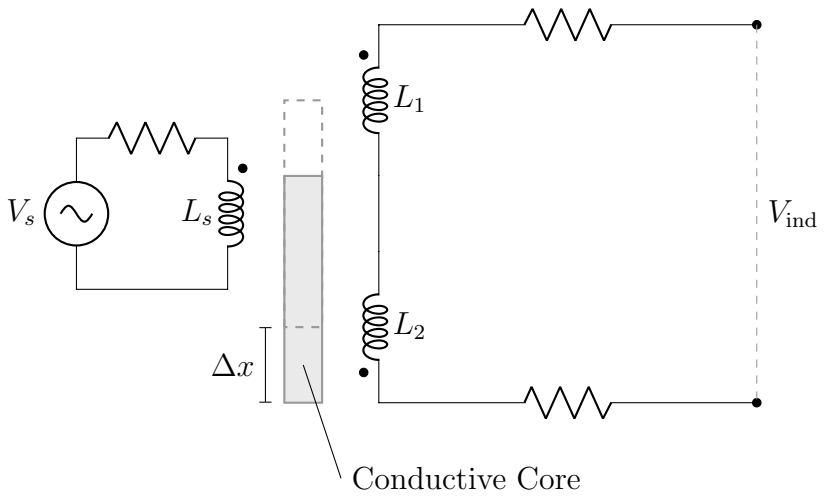

Figure 2.4: Schematic of an LVDT. The dashed gray box is the centre position of the core. Although not pictured here, typically the core is inserted through the three coils.

analysis for simplicity. M_1 and M_2 are related to the displacement of the conducting core from its centre position, Δx, by $M_2 - M_1 \propto \Delta x$. In the case that an inductor is excited by a signal of constant frequency, the voltage across the inductor varies linearly with the current, thus the output voltage, V_{ind}, is proportional to ΔM. The output voltage is then linear with the displacement of the conductive core, allowing for a measurement of displacement to be obtained from V_{ind}.

The inductance of the source coil, L_s, determines the sensor bandwidth, which is generally limited to 1 kHz. Greater excitation frequencies produce eddy currents in the core that adversely impact performance [24]. With the use of conditioning circuits accuracies of 0.25 % FSR can be achieved. For low FSRs of 500 µm, resolutions of a 5 nm are possible, but the largest commercially available FSRs of 500 mm deliver resolutions of only 1 µm [4]. Power dissipation can range from 2.5 mW [25] up to 500 mW [26] in commercially available LVDTs.

Small inductors are used to reduce space and increase response time [27], which have an added side effect of reduced sensitivity to electrical noise due to the low coil impedance. In combination with their simple design, modules can be made robust to both mechanical and electrical environmental factors. Large FSRs are achieved with moderate resolutions, enabling the use of LVDTs in long range applications [4].

Although LVDTs are considered a contactless sensor, often the sensor housing has mechanical contact to keep the core centred between the coils, unless used in an application where the alignment of the core and coils is maintained over the entire FSR by design. Similar to eddy current sensors, LVDTs are sensitive to external magnetic fields [28] and Joule heating, which may limit their adoption in certain applications.

The Spitzer Space Telescope employed a pair of redundant LVDT position sensors in the cryogenic scan mirror mechanism for its multi-band imaging photometer at temperatures ≤ 13 K. [29–32]. The sensors measure the position of a mirror mechanism which pivots over a range of 15° around a single axis. Since the mechanism is

not fast scanning, the bandwidth required is $\sim 10\,\text{Hz}$.

The SPIRE instrument onboard Herschel employed a Heidenhain optical encoder [33] along with an LVDT that could provide redundant position measurement [34]. The LVDT had a limited range and dissipated approximately $0.1\,\text{mW}$ of thermal power, but was never used.

2.5 Optical Encoders

Optical encoders consist of a glass scale and a read-head, illustrated in Figure 2.5. Reflective lines at even intervals along the scale are illuminated by a source such as an LED, and the reflected power is collected by a detector. As the read-head moves relative to the scale, the reflected power is modulated and the peaks correspond to the distance between the reflective lines. Not pictured in Figure 2.5 is a second scale offset by $\pi/2$ in phase, which serves to generate the quadrature signal.

The FSR of an optical encoder is limited by the length of the scale, which in principle, can be built arbitrarily long. Typically, high resolution encoders achieve a resolution of $6\,\text{nm}$ with an accuracy of $5\,\mu\text{m/m}$. Certain encoders are capable of

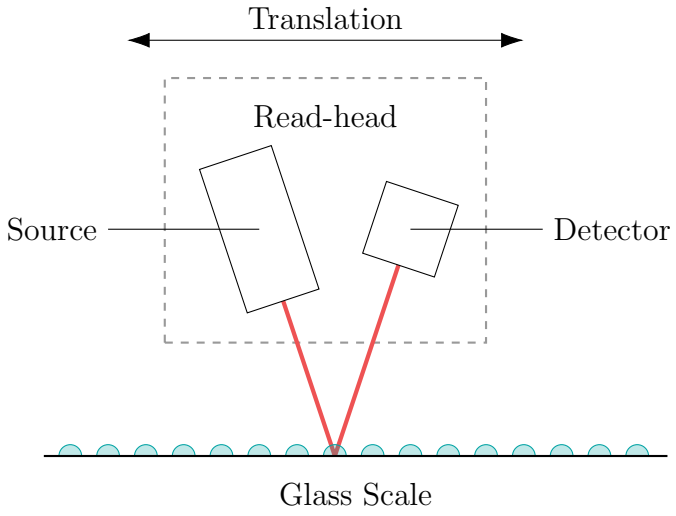

Figure 2.5: Simplified operation of an optical encoder.

accuracies of 0.5 µm/m at the cost of a reduced FSR. Optical encoders are suitable for applications requiring high bandwidths and are capable of exceeding 100 kHz [4].

The cryogenic operation of optical encoders poses a number of challenges. Fundamentally, the scale must be at least as long as the maximum displacement to be measured, therefore, the mass of the scale increases with the required displacement. For a cryogenic system to reach its target temperature, it is critical that the thermal load be limited to a maximum tolerable value, which may be exceeded due to the relatively large mass added by an optical encoder. Additionally, the size and shape can possibly violate volume and placement constraints, as the encoder must be placed entirely inside the cryogenically cooled volume.

Adopting an optical encoder may require extra consideration during the initial design, as one cannot easily be retrofitted to an instrument due to the size, shape, and mass. There are two practical ways to mount the encoder: the scale can be fixed and the read-head moved, or the read-head fixed can the scale moved. Typically, the scale is fixed and the read-head is mounted to the moving part of the instrument. As the mass of the moving mechanism increases, so does the required driving force, which will lead to an increase in thermal power dissipation. Additionally, mass is a cost driver for placing instrument in orbit, limiting the adoption of an optical encoder short range applications.

An easily overlooked challenge in using an optical encoder in astronomical instrumentation occurs during launch [35]. Due to the extreme forces involved, onboard equipment is susceptible to damage during launch if not secured properly. Glass scales in optical encoders are particularly fragile, which introduce additional launch risks.

Optical encoders have been used in space on missions such as Herschel [36,37] and AKARI [35,38]. Herschel used a modified Heidenhain LIP401A Moiré fringe encoder which achieved an accuracy of 10 nm at cryogenic temperatures [39, 40]. A modified

Heidenhain LIP401P encoder was flown on AKARI and provided an accuracy of 1 µm at temperatures of $\sim 3\,\mathrm{K}$ [35]. Heidenhain encoders typically dissipate up to 1 W of power [33], and the thermal power dissipation of the modified encoder was 1.2 mW at cryogenic temperatures [34].

The James Webb Space Telescope (JWST) employs a computational pattern recognition optical encoder which analyzes images of linear and rotary scales [41]. Unlike traditional encoders which are fabricated with repetitive scales patterns that provide relative displacement measurements, the JWST scales encode absolute displacement. Evaluation of the encoder performance at 100 K showed an accuracy of 60 nm rms [42].

2.6 Interferometers

The combination of multiple waves that results in an intensity which differs from the sum of each constituent intensity is known as interference. It is this principle that optical interferometers are built upon, which enables properties of light such as wavelength and phase to be measured. Michelson sought to provide a robust definition of the metre, which using the Michelson interferometer design, was once defined as 1 650 763.73 wavelengths of the orange-red emission line of ^{86}Kr [43]. To date, the Laser Interferometer Gravitational-Wave Observatory (LIGO) is the most displacement sensitive interferometer ever constructed. LIGO was designed to detect the miniscule fluctuations in space-time produced by gravitational waves as predicted by Einstein's general theory of relativity [44]; LIGO is capable of measuring displacements of $10^{-18}\,\mathrm{m}$ [45].

Although there are many interferometer designs, the simplest is the Michelson [46–48], which is depicted in Figure 2.6 (and discussed further in Subsection 3.1.5). In this configuration, the beamsplitter cube and fixed mirror are positioned such that the length of the first arm is constant, but the length of the second arm can be changed due to the moving mirror. Assuming that the input intensity, I_{in}, is

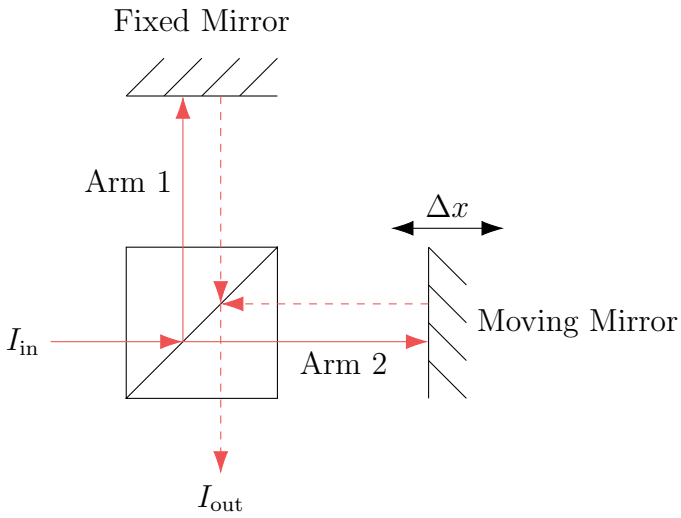

Figure 2.6: A Michelson interferometer constructed with a beamsplitter cube.

constant, the output intensity, I_{out}, will vary as a function of the displacement, Δx, of the moving mirror. It is this principle that all range-resolved interferometers, such as those discussed in Chapters 4 and 5, are built upon.

In theory, the FSR of a continuous wavelength laser interferometer is limited by the coherence length of the laser, which can exceed 10 000 km [47]. In practice, however, commercially available interferometers can reach FSRs of up to 60 m [49], although some techniques relying on frequency modulation can only support smaller FSRs of < 1 m [50]. Interferometers offered by Renishaw achieve resolutions of 39 pm [51], which corresponds to $\ll 1$ ppm FSR. The practical bandwidth is limited by the photodetection and processing electronics allowing it to exceed 100 kHz, and in some cases reach up to 16 MHz [49]. Commercial units are available with < 1 mW laser output power [49].

Homodyne interferometers may suffer $1/f$ noise at the photodetectors, which limits the measurement accuracy of slowly moving or stationary objects. Significant levels of $1/f$ noise have the potential to lead to the detection of false fringes [52]. All interferometers require a clear optical path, and if the beam is broken then there is an irrecoverable loss of displacement information.

Traditionally, interferometers were large instruments which required a clear line of sight for the propagation of the laser beam, however, fibre optic interferometers can be manufactured to occupy very little space. Fibre optic interferometers offer the ability to route the fibre through compact spaces and to be retrofitted to existing designs. Since fibre optic cables have very low signal attenuation, typically $< 0.20\,\mathrm{dB/km}$ for 1550 nm wavelengths [53], cabling can be made long enough to deliver metrology to difficult to access locations with minimal signal losses. Commercial lasers operating at 1550 nm are not designed for cryogenic temperatures, and the ability to separate the laser from the environment via cabling is necessary for cryogenic operation. Furthermore, by distancing the laser from the cryogenic environment, only the fibre itself contributes to the thermal load, and the electronics can be isolated to minimize parasitic electrical effects on instrumentation in the cryogenic volume. Only the photons that do not return to the fibre will be absorbed into the cryogenic volume and contribute to the thermal load. In practice, the thermal power dissipation can be made extremely small by attenuating the signal to $< 1\,\mathrm{mW}$ before it enters the cryogenically cooled volume.

Interferometers have been used in the cryogenic testing of astronomical instrumentation. Notable examples include the testing of a novel angle-scanned Fabry-Pérot interferometer for astronomical instrumentation [54, 55] and thermal expansion properties of carbon fibre reinforced polymer composites for space telescope mirrors from room to cryogenic temperatures [56, 57].

2.7 Summary and Comparison

The performance of each technique discussed in this chapter is summarized in Table 2.1. Recall that the SAFARI metrology requirement, outlined in Section 1.1, calls for 10 nm rms accuracy at 20 Hz bandwidth over a 33.5 mm FSR. Additionally, the system must be cryogenic and dissipate no more than 0.1 mW of thermal power.

Table 2.1: Comparison of position metrology techniques. The thermal power is quoted as the power dissipated within a cryogenic environment.

Type	**Performance**		**Pros**	**Cons**	**Space Missions**
Resistive	FSR Bandwidth Resolution Accuracy Power Thermal Power (Cryogenic)	500 µm > 100 kHz 0.5 nm 1 % FSR < 100 mW < 1 mW†	High precision High bandwidth Small thermal load Bond directly to component	Short range	None to date‡
Capacitive	FSR Bandwidth Resolution Accuracy Power Thermal Power (Cryogenic)	10 mm 100 kHz < 1 nm 5 ppm FSR ≥ 1 W 0 mW	High precision High bandwidth Small thermal load	Short range Stress-induced non-linearity Contamination of air gap Susceptible to electric fields	ISO [13–15]
Eddy Current	FSR Bandwidth Resolution Accuracy Power Thermal Power (Cryogenic)	80 mm 100 kHz 10 nm 0.1 % FSR 12 mW to 750 mW Unavailable‡	High precision High bandwidth	Joule heating Susceptible to magnetic fields	Cassini [21, 22]
LVDT	FSR Bandwidth Resolution Accuracy Power Thermal Power (Cryogenic)	500 mm 1 kHz 5 nm 0.25 % FSR 2.5 mW to 500 mW 0.112 mW [34]	Long range High precision Robust	Joule heating Susceptible to magnetic fields	Herschel [34, 36, 37] Spitzer [29–32]
Optical Encoder	FSR Bandwidth Resolution Accuracy Power Thermal Power (Cryogenic)	> 1 m > 100 kHz 6 nm 5 ppm FSR < 1 W 1.2 mW [34]	Long range High precision High bandwidth	High power Massive Large thermal load Fragile	Herschel [34, 36, 37] AKARI [35, 38] JWST [41, 42]
Interferometer	FSR Bandwidth Resolution Accuracy Power Thermal Power (Cryogenic)	> 1 m > 100 kHz < 1 nm < 1 ppm FSR < 1 mW < 0.1 mW†	Long range High precision High bandwidth Low power Small thermal load Ability to route fibres	Susceptible to beam breakage	None to date

† Estimate based on reasonable operating conditions.
‡ To the best of my current knowledge.

It can be seen from Table 2.1 that resistive and capacitive sensors do not satisfy the range requirement of SAFARI. The inductive eddy current and LVDT sensors cannot achieve the required accuracy over a 33.5 mm range, and Joule heating due to induced currents may dissipate additional thermal power. An optical encoder can satisfy the metrology requirements, however, it produces significant thermal power and is relatively massive.

An interferometer is the only candidate that can satisfy both the SAFARI metrology performance requirements and thermal power requirement. For these reasons, SAFARI has adopted a frequency modulation range-resolved interferometer to provide position metrology at $< 4\,\mathrm{K}$ [2].

2.8 Conclusions

In this chapter, cryogenic applications of resistive, capacitive, inductive, optical encoder, and interferometric position metrology techniques were introduced and compared. An evaluation of each technique against the SAFARI metrology requirements shows that an interferometer concept is best suited to provide position metrology for the SAFARI instrument. In this thesis I will discuss two cryogenic range-resolved laser interferometers: a three-phase interferometer in Chapter 4 and a frequency modulation interferometer in Chapter 5; the latter being the approach adopted by SAFARI.

Chapter 3

Practical Considerations for a Fibre Optic Range-resolved Laser Interferometer

The work discussed throughout this thesis involves a number of topics in photonics and signal processing. In this chapter I provide an introduction to photonics and an overview of techniques and considerations in the development of a ranged-resolved interferometer.

3.1 Optics

Topics in this thesis deal with concepts related to light, or more formally, electromagnetic radiation. One must be careful to consider the wave nature of light in its propagation, and its particulate nature in its interactions with matter. Because work throughout this thesis deals with lasers, all light (and waves in general) will be considered monochromatic, meaning that they have only a single frequency component.

3.1.1 Electromagnetic Radiation

When considering the propagation of electromagnetic radiation, we are examining the behaviours of its intrinsic electric and magnetic fields. To begin, consider linearly polarized electromagnetic plane waves (covered in Subsection 3.1.2), travelling in the direction of the Poynting vector, $\vec{S}$, with an electric field, $\vec{E}$, and a magnetic field, $\vec{B}$,

such that $\vec{S}$, $\vec{E}$, and $\vec{B}$ are all orthogonal to each other, in the relation [47]

$$\vec{S} \propto \vec{E} \times \vec{B}. \qquad [\mathrm{W/m^2}] \quad (3.1)$$

In a vacuum, light propagates at a speed of c, which is approximately 3×10^8 m/s. The definition of c comes from the vacuum permittivity, ϵ_0, and the vacuum permeability, μ_0. For a given medium, permittivity is its ability to electrically polarize in the presence of a electric field, and permeability is its ability to magnetize in the presence of a magnetic field. In vacuum the speed of propagation of the wave is related to the permittivity and permeability by [47]

$$c = \frac{1}{\sqrt{\epsilon_0 \mu_0}}. \qquad [\mathrm{m/s}] \quad (3.2)$$

Likewise, the local speed of light in some isotropic medium depends on the local permittivity and permeability, ϵ and μ, respectively. It is common to relate the local speed of light to the vacuum speed of light by the refractive index, n. The refractive index is a unitless quantity which relates the electromagnetic properties of a medium to those of a vacuum by

$$n = \sqrt{\frac{\epsilon \mu}{\epsilon_0 \mu_0}}. \quad (3.3)$$

The magnitudes of the $\vec{E}$ and $\vec{B}$ fields are related by [47]

$$|\vec{E}| = \frac{c}{n}|\vec{B}|, \qquad [\mathrm{V/m}] \quad (3.4)$$

and the energy densities of the $\vec{E}$ field, u_E, and $\vec{B}$ field, u_B, are [47]

$$u_E = \frac{\epsilon}{2}|\vec{E}|^2, \qquad [\mathrm{J/m^3}] \quad (3.5a)$$

$$u_B = \frac{1}{2\mu}|\vec{B}|^2, \qquad [\mathrm{J/m^3}] \quad (3.5b)$$

which by Equation 3.4, requires that $u_E = u_B$, and the total energy density of the wave can be expressed as $u = 2u_E = 2u_B$. Using this relation and Equation 3.2, expressions for the energy densities are [47]

$$u = \epsilon|\vec{E}|^2 = \frac{1}{\mu}|\vec{B}|^2. \qquad [\mathrm{J/m^3}] \quad (3.6)$$

Imagine that electromagnetic waves are propagating through free space, and from our perspective, travelling left to right. We can select a prism in free space such that its axis is parallel to $\vec{S}$, which is the direction of propagation. In some time interval, Δt, the total energy contained in the prism will exit through the face on the right. This prism has a volume, V, which is the product of its length, $c\Delta t$, and the area of the face, A, as illustrated in Figure 3.1.

$\vec{S}$ contains the amount of energy, E, transmitted through an area, A, in the time Δt. The model presented in Figure 3.1 is exactly this situation, which is then described by [47]

$$|\vec{S}| = \frac{E}{\Delta t A} = \frac{uV}{\Delta t A} = \frac{uc\Delta t A}{\Delta t A} = uc. \qquad [\mathrm{W/m^2}] \quad (3.7)$$

From Equations 3.6 and 3.7, the definition for the magnitude of the Poynting

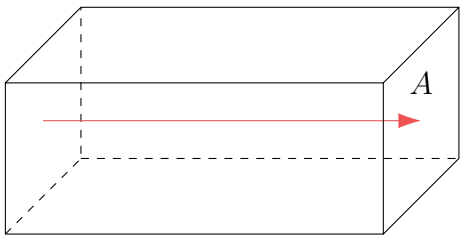

Figure 3.1: A model for energy transferred by an electromagnetic wave. The wave travels from left to right in the direction of the arrow through a prism of length $c\Delta t$. The left and right faces of the prism have an area, A, to make a total volume, V.

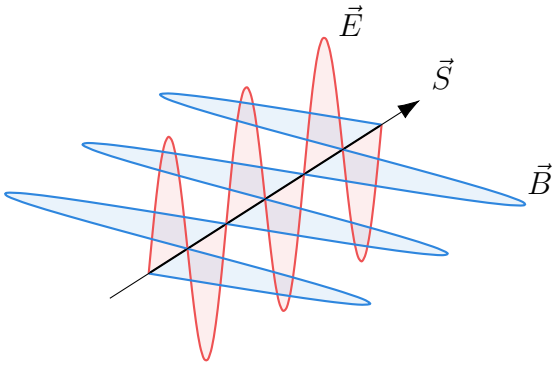

Figure 3.2: Propagation of electromagnetic radiation showing the Poynting vector.

vector can be formulated as [47]

$$|\vec{S}| = \frac{1}{\mu}|\vec{E}||\vec{B}|. \qquad [\mathrm{W/m^2}] \quad (3.8)$$

Naturally, it follows from Equation 3.8 that the missing coefficient from Equation 3.1 is $c^2\epsilon$. Thus, the full definition of the Poynting vector is [47]

$$\vec{S} = \frac{1}{\mu}\vec{E} \times \vec{B}. \qquad [\mathrm{W/m^2}] \quad (3.9)$$

An electromagnetic wave will travel with constant optical frequency, ν. However, of equal importance is the angular spatial frequency vector, $\vec{k}$, which depends on the direction of propagation according to

$$\vec{k} = \frac{\vec{S}}{|\vec{S}|}\frac{2\pi\nu}{c}. \qquad [\mathrm{rad/m}] \quad (3.10)$$

Upon examining $\vec{E}$ and $\vec{B}$ more closely, it can be seen that their forms are quite similar. Using $\vec{k}$ and an angular frequency, $\omega = 2\pi\nu$, both $\vec{E}$ and $\vec{B}$ fields are expressed

as a function of a position vector, $\vec{r}$, and time, t, by

$$\vec{E} = \vec{E}_0 \cos\left(\vec{k} \cdot \vec{r} - \omega t\right), \qquad \text{[V/m]} \quad (3.11a)$$

$$\vec{B} = \vec{B}_0 \cos\left(\vec{k} \cdot \vec{r} - \omega t\right). \qquad \text{[A/m]} \quad (3.11b)$$

Equation 3.11 illustrates the similarity in propagation of $\vec{E}$ and $\vec{B}$ fields, although their amplitudes, $\vec{E}_0$ and $\vec{B}_0$, are orthogonal, as described by $\vec{S}$ in Equation 3.9. An illustration of $\vec{S}$, $\vec{E}$, and $\vec{B}$ according to Equations 3.9 and 3.11 is shown in Figure 3.2.

A single photon contains energy, E_{photon}, proportional to its frequency, ν,

$$E_{\text{photon}} = \text{h}\nu, \qquad \text{[J]} \quad (3.12)$$

where h is Planck's constant [47]. When a photon impinges on a detector, the detector response depends the photon energy, E_{photon}, given by Equation 3.12. One such detector is the semiconductor detector, which is a photonic device that can absorb a photon to create an electrical current. An electron in the semiconductor must gain sufficient energy, called the gap energy, E_{g}, to transition from the valence band to the conduction band and become a charge carrier. Therefore, it is necessary that the photon carries energy $E_{\text{photon}} \geq E_{\text{g}}$, and the photon frequency must satisfy the inequality

$$\nu \geq \frac{E_{\text{g}}}{\text{h}}, \qquad \text{[Hz]} \quad (3.13)$$

to be absorbed by the semiconductor [48].

3.1.2 Wave Equation

There are infinitely many ways which light can propagate, all being solutions to the wave equation,

$$\left(\frac{\partial^2}{\partial x^2}+\frac{\partial^2}{\partial y^2}+\frac{\partial^2}{\partial z^2}\right)\Psi-\frac{1}{c^2}\frac{\partial^2\Psi}{\partial t^2}=0, \tag{3.14}$$

where x, y, and z are Cartesian coordinates, c is the speed of the wave, and $\Psi(x,y,z,t)$ is the wave function [48]. There exist three simple solutions to the wave equation: plane, spherical, and cylindrical waves, however, only the discussion of plane and spherical waves pertain to the contents of this thesis.

Plane Waves

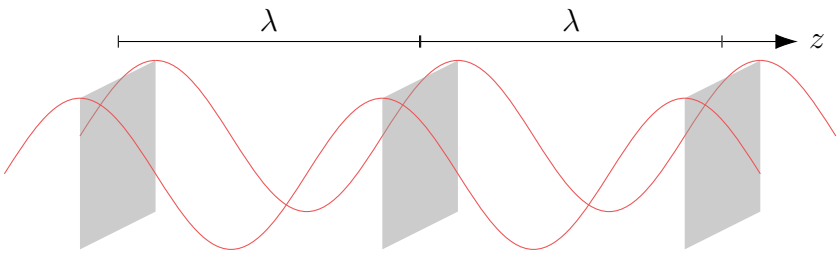

Figure 3.3: Wavefronts of a linearly polarized plane wave in the vertical direction.

The plane wave solution to Equation 3.14 defines the wavefronts to be parallel planes, as shown in Figure 3.3. Consider z to be the optical axis of a plane wave, which is the direction of propagation. For this wave to be considered a plane wave, the wavefronts must each form a planar surface oriented such that z is parallel to their normals, and the distance between them is the wavelength, λ [47, 48].

Spherical Waves

A spherical wave is characterized by wavefronts which are thin spherical shells that either emanate from or converge to a point. The distance between these shells is the

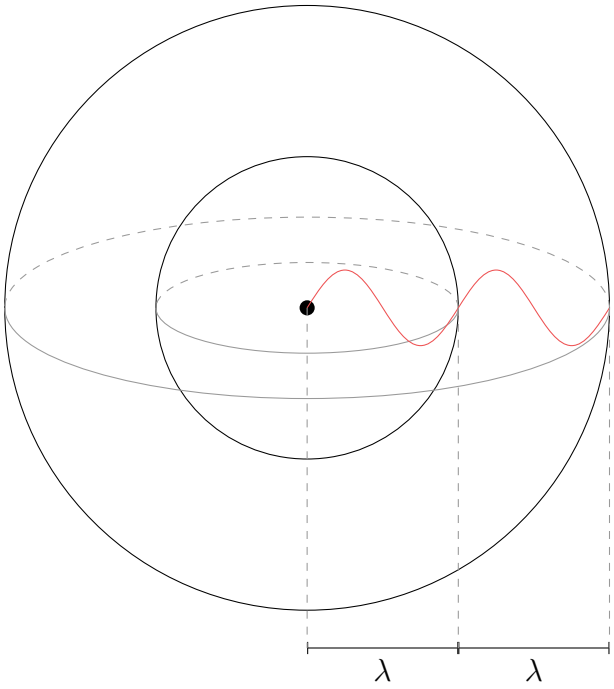

Figure 3.4: Wavefronts of a spherical wave illustrated as thin spherical shells.

wavelength, λ, of the waves. Illustrated in Figure 3.4, the wavefronts of a spherical wave are shown as concentric spherical shells.

Due to the linearity of Equation 3.14, the superposition of any number of waves must also be a wave, which allows any wave, such as a plane wave, to be expressed as the superposition of infinitely many spherical waves [48]. Figure 3.5 shows the superposition of five spherical wave sources each with a wavelength, λ, arranged linearly to create an extended source. Distances in increments of λ measured normal to the extended source exhibit the tendency to form planar wavefronts as we observe the waves travelling from near-field to far-field. Photonic systems are better discussed in terms of Gaussian beams, which conversely, exhibit plane wave properties in the near-field and spherical wave properties in the far-field [47, 48].

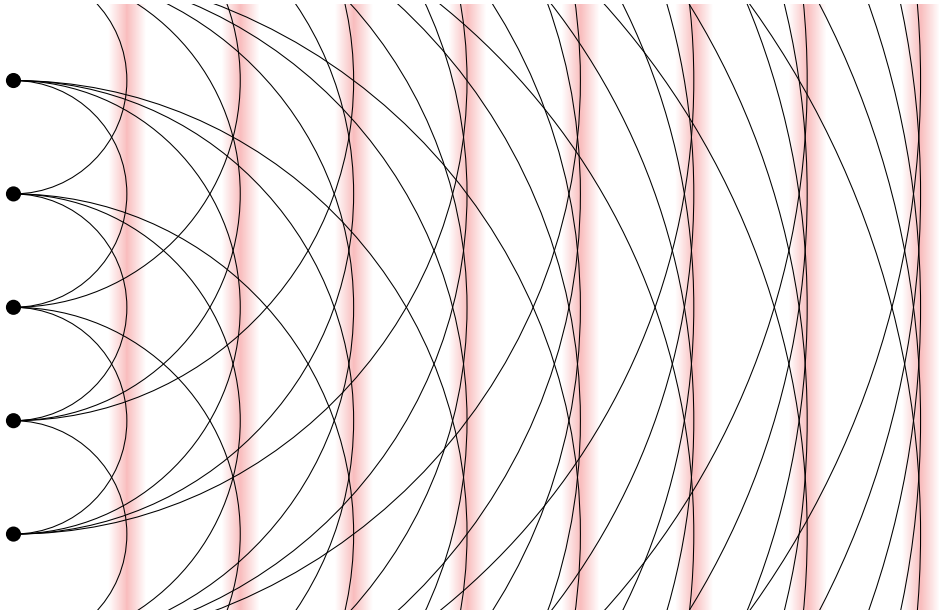

Figure 3.5: A plane wave constructed from an extended source or spherical waves. The wavefronts become more apparently planar as the distance from the extended source increases.

3.1.3 Gaussian Beams

It can be shown that when light encounters an optical component, the component performs a Fourier transform on the $\vec{E}$ and $\vec{B}$ fields [48]. The Fourier transform, $\mathcal{F}$, of a Gaussian, such as e^{-ax^2}, for some constants, A and a, is [58]

$$\mathcal{F}\left\{A\mathrm{e}^{-ax^2}\right\}(\nu) = \int_{-\infty}^{\infty} A\mathrm{e}^{-ax^2}\mathrm{e}^{-j2\pi x\nu}\,dx = A\sqrt{\frac{\pi}{a}}\mathrm{e}^{-\pi^2\nu^2/a}, \tag{3.15}$$

where the output is Gaussian in ν instead of x. Therefore, when a Gaussian beam, whose intensity is a Gaussian distribution, is transformed by an optical component, the transformed beam maintains a Gaussian intensity distribution. Regardless of how many optical components are in a system, if a Gaussian beam enters, then the beam that exits will also be Gaussian, provided that each component is appropriately sized to avoid beam truncation [48]. Since I will be working with single mode fibre coupled and free space components, the preferred treatment of light is as a Gaussian beam.

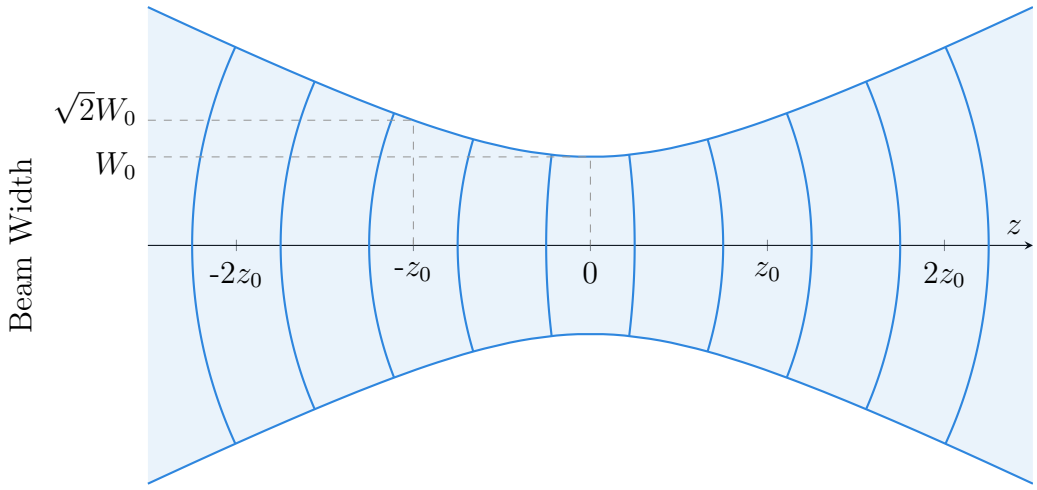

Figure 3.6: Profile of a Gaussian beam showing wavefront bending from the near-field ($z = 0$) to the far-field ($z \to \pm\infty$).

A wave is said to be paraxial when its wavefront normals are parallel to or form small angles with the beam axis, z [48]. The Gaussian beam is a paraxial solution to the wave equation, Equation 3.14, and its paraxial nature can be seen in the wavefronts of Figure 3.6. Although plane and spherical waves provide relatively simple models of light, a more realistic model of wave propagation is that of a Gaussian beam, which is planar in nature in the near-field, and becomes spherical in the far-field, as illustrated by Figure 3.6.

Suppose that a Gaussian beam is generated with a wavelength, λ, in some isotropic medium. The beam radius, W, increases with z according to [48]

$$W(z) = W_0\sqrt{1 + \left(\frac{z}{z_0}\right)^2}, \qquad \text{[m]} \quad (3.16)$$

and is most narrow at $z = 0$ where its waist radius, W_0, is

$$W_0 = \sqrt{\frac{\lambda z_0}{\pi}}. \qquad \text{[m]} \quad (3.17)$$

The *Rayleigh range*, z_0, is the distance from the beam waist where the cross sectional area doubles, or in other words, $W(z_0) = \sqrt{2}W_0$. The shape of a Gaussian beam, such as in Figure 3.6, is fully described by W_0, z_0, and the position of the beam waist, z.

Near the beam waist location at $z = 0$, a Gaussian beam is approximated by a plane wave. As z increases, the wavefronts will bend and the beam is better approximated by a spherical wave. Subsequently, the radius of curvature, R, of the wavefront changes as a function of the distance from the beam waist [48].

$$R(z) = z\left[1 + \left(\frac{z_0}{z}\right)^2\right]. \qquad \text{[m]} \quad (3.18)$$

In Equation 3.18, clearly the beam is a plane wave at $z = 0$ where $R(0) = \infty$, and a spherical wave at $z = \infty$, as a result of

$$\lim_{z\to\infty} R(z) = z. \qquad \text{[m]} \quad (3.19)$$

Because the wavefront is not planar everywhere, the phase, ϕ, of the wave is a function of both z and the radial distance, ρ, from the z-axis. In addition, a phase retardation, called the *Gouy effect*, is observed due to the superposition of all waves in the beam. The Gouy phase shift, ζ, in Equation 3.20, is the difference in the phase of a Gaussian beam compared to a plane wave propagating in the same direction [48], and is given by

$$\zeta(z) = \arctan\frac{z}{z_0}. \qquad \text{[rad]} \quad (3.20)$$

The Gouy effect is most significant within the depth of focus of the beam, which is the region where $-z_0 \leq z \leq z_0$. For a point on the z axis, a phase shift of $\zeta(z_0) = \pi/4$

is observed at the Rayleigh range, and an additional shift of $\pi/4$ is observed over the region from z_0 to $z = \infty$. A total phase shift of $\pi/2$ is observed over $z = 0$ to $z = \infty$, and the phase shift from $z = -\infty$ to $z = \infty$ is π. For a point off the z-axis, the phase of the beam is described by

$$\phi(\rho, z) = kz - \zeta(z) + \frac{k\rho^2}{2R(z)}. \qquad \text{[rad]} \quad (3.21)$$

In Equation 3.21, $k = 2\pi/\lambda$ is the angular spatial frequency of the wave, also called the angular wavenumber. Equation 3.21 has three terms: the first is the phase of a plane wave, the second accounts for the Gouy effect, and the third is the phase of a spherical wave. From this equation it can be seen that the wavefronts are planar in the near-field (relative to the beam waist) and spherical in the far-field, as shown in Figure 3.6.

The intensity, I, at any arbitrary point is [48]

$$I(\rho, z) = \frac{I_0}{1 + (z/z_0)^2} \exp\left[-\frac{2\rho^2}{W(z)^2}\right], \qquad \text{[W/m}^2\text{]} \quad (3.22)$$

where for a beam carrying power, P, the intensity, I_0, at $z = 0$ and $\rho = 0$ is

$$I_0 = \int_0^\infty 2\pi\rho I(\rho, z)\, d\rho = \frac{2P}{\pi {W_0}^2}. \qquad \text{[W/m}^2\text{]} \quad (3.23)$$

Transmission Through a Lens

It was previously shown that the shape of a Gaussian beam is described by three parameters: the beam waist location, z the beam waist radius, W_0, and the Rayleigh range, z_0. Optical systems discussed in this thesis involve the transmission of light through a lens, for which the transformed beam parameters must be obtained.

A lens with a focal length f is centred at $z = 0$ on the optical axis as shown in Figure 3.7. Note that $f > 0$ for this lens since it is converging, and conversely, a

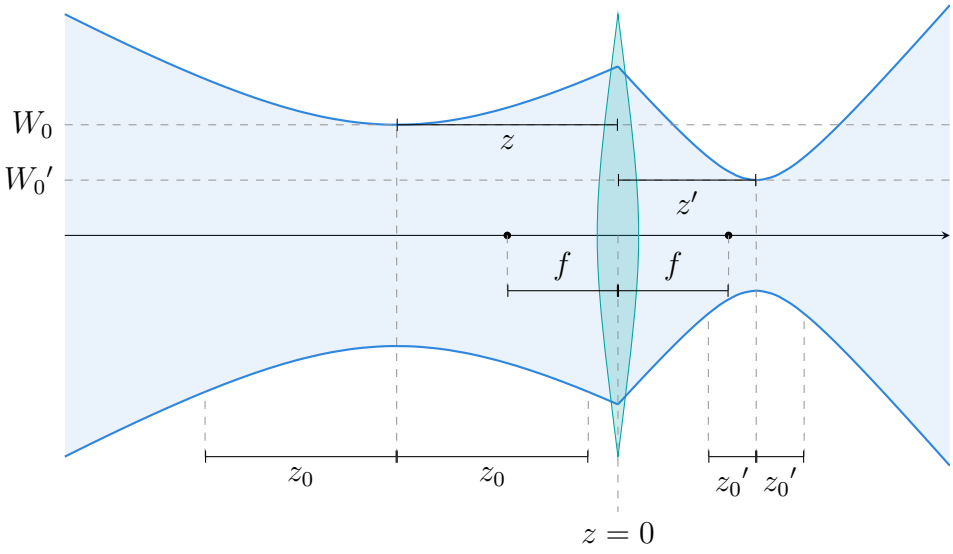

Figure 3.7: A converging lens transforming a Gaussian beam.

diverging lens would require $f < 0$. The incident beam waist is a distance z from the lens, and the transformed beam waist is a distance z' from the lens.

The transformation of the beam parameters to produce the new beam waist radius, W_0', waist location, z', and Rayleigh range, z_0', can be expressed in terms of the lens magnification, M, which relates the beam location and geometry to the position of the lens [48].

$$M = \frac{|f/(z-f)|}{\sqrt{1+(z_0/(z-f))^2}}. \tag{3.24}$$

Using the magnification, the transformed waist radius, W_0', waist location, z', and

Rayleigh range, z_0', are [48]

$$W_0' = MW_0, \quad \text{[m]} \quad (3.25a)$$

$$z' = M^2(z - f) + f, \quad \text{[m]} \quad (3.25b)$$

$$z_0' = M^2 z_0. \quad \text{[m]} \quad (3.25c)$$

3.1.4 Interference

The interference of any number of waves is a process which produces a wave whose intensity differs from the sum of the input intensities. As shown by Equation 3.4, it is possible to formulate intensity from $\vec{E}$ or $\vec{B}$, although the convention is to use $\vec{E}$. Formally, the intensity, I, is defined as [47]

$$I = \left\langle |\vec{S}| \right\rangle, \quad \text{[W/m}^2\text{]} \quad (3.26)$$

where $\langle |\vec{S}| \rangle$ is the time average of $|\vec{S}|$. For a sinusoid with an angular frequency of ω, the period, T, of the signal is $T = 2\pi/\omega$. Recall that the time average of any periodic function, $f(t)$, such as a sinusoid, is

$$\langle f(t) \rangle = \frac{1}{T} \int_{t_0}^{t_0+T} f(t)\, dt. \quad (3.27)$$

Since we are only concerned with the $\vec{E}$ field at this point, we will instead express the intensity in terms of $\vec{E}$, which through Equations 3.4 and 3.8, is

$$I = \frac{c\epsilon}{2} \left\langle \vec{E}^2 \right\rangle, \quad \text{[W/m}^2\text{]} \quad (3.28)$$

where $\vec{E}^2 = \vec{E} \cdot \vec{E}$. As c and ϵ are properties of the medium, they are ignored for this section of the discussion, and it is assumed that interference occurs in a single isotropic medium. With this simplification, we will be considering relative intensities, and we will use intensity defined as

$$I = \left\langle \vec{E}^2 \right\rangle = \frac{1}{2}|\vec{E}|^2. \qquad [\mathrm{W/m^2}] \quad (3.29)$$

Consider two monochromatic waves of the same spatial and optical frequencies, but arbitrary amplitudes and phases, $\vec{E}_{01}$, $\vec{E}_{02}$, ϕ_1, and ϕ_2,

$$\vec{E}_1 = \vec{E}_{01} \cos\left(\vec{k}_1 \cdot \vec{r} - \omega t + \phi_1\right), \qquad [\mathrm{V/m}] \quad (3.30a)$$

$$\vec{E}_2 = \vec{E}_{02} \cos\left(\vec{k}_2 \cdot \vec{r} - \omega t + \phi_2\right). \qquad [\mathrm{V/m}] \quad (3.30b)$$

The interference of the waves in Equations 3.30a and 3.30b will result in an intensity expression with three components,

$$\begin{aligned} I &= \left\langle \left(\vec{E}_1 + \vec{E}_2\right)^2 \right\rangle \\ &= \left\langle \vec{E}_1^2 + \vec{E}_2^2 + 2\vec{E}_1 \cdot \vec{E}_2 \right\rangle \\ &= \left\langle \vec{E}_1^2 \right\rangle + \left\langle \vec{E}_2^2 \right\rangle + 2\left\langle \vec{E}_1 \cdot \vec{E}_2 \right\rangle. \end{aligned} \qquad [\mathrm{W/m^2}] \quad (3.31)$$

Each of the three components in Equation 3.31 will correspond to one term in the interference equation:

$$I = I_1 + I_2 + I_{12}. \qquad [\mathrm{W/m^2}] \quad (3.32)$$

The three terms that comprise Equation 3.32 each have a distinct physical meaning that can be traced back to Equation 3.31. Respectively, the three terms are:

1. $I_1 = \langle \vec{E}_1^2 \rangle$ is the intensity of $\vec{E}_1$.
2. $I_2 = \langle \vec{E}_2^2 \rangle$ is the intensity of $\vec{E}_2$.

3. $I_{12} = 2\langle \vec{E}_1 \cdot \vec{E}_2 \rangle$ is the *interference term*, which captures both the phase and amplitude departures between $\vec{E}_1$ and $\vec{E}_2$.

The interference term takes on a value that is dependent on the phase difference, $\Delta\phi = \phi_2 - \phi_1$, between $\vec{E}_1$ and $\vec{E}_2$ [47]:

$$I_{12} = 2\sqrt{I_1 I_2}\cos\Delta\phi, \qquad [\mathrm{W/m^2}] \quad (3.33)$$

and the full equation for the resulting intensity then becomes

$$I = I_1 + I_2 + 2\sqrt{I_1 I_2}\cos\Delta\phi. \qquad [\mathrm{W/m^2}] \quad (3.34)$$

In the special case when $I_1 = I_2 = I_0$, Equation 3.34 becomes

$$I = 4I_0\cos^2\frac{\Delta\phi}{2}, \qquad [\mathrm{W/m^2}] \quad (3.35)$$

For cases of total constructive interference, when $\Delta\phi = 2m\pi \ \forall m \in \mathbb{Z}$, Equation 3.34 takes on a value of $I_{\max}$. Conversely, for cases of total destructive interference, when $\Delta\phi = (2m+1)\pi \ \forall m \in \mathbb{Z}$, Equation 3.34 takes on a value of $I_{\min}$. These values are properly defined as

$$I_{\max} = I_1 + I_2 + 2\sqrt{I_1 I_2}, \qquad [\mathrm{W/m^2}] \quad (3.36a)$$

$$I_{\min} = I_1 + I_2 - 2\sqrt{I_1 I_2}. \qquad [\mathrm{W/m^2}] \quad (3.36b)$$

When fringes are produced, the visibility, $\mathcal{V}$, is an indicator of the fringe quality [47]. The definition of visibility,

$$\mathcal{V} = \frac{I_{\max} - I_{\min}}{I_{\max} + I_{\min}} = \frac{2\sqrt{I_1 I_2}}{I_1 + I_2}, \quad (3.37)$$

is the contrast between a bright fringe and a dark fringe, which takes on a value in the interval $[0, 1]$. This measurement of fringe contrast tells us that bright fringes are indistinguishable from dark fringes when $\mathcal{V} = 0$, since that would require $I_{\max} = I_{\min}$. Conversely, bright fringes have strong contrast against a pure dark background as $I_{\min}$ tends to zero, giving the best possible fringe visibility, $\mathcal{V} = 1$.

3.1.5 Michelson Interferometer

The simplest interferometer design is the Michelson [46–48], which uses two optical paths to produce a phase difference between two beams created from the same source. One possible Michelson interferometer configuration based on a beamsplitter cube is illustrated in Figure 3.8. In this configuration, light with intensity I_{in} enters the beamsplitter cube from the left and is split into two beams, I_1 and I_2, which are directed toward the fixed and moving mirrors, respectively. The beam directed toward the moving mirror will be called the *probing beam*. Both beams reflect off the mirrors and return to the beamsplitter and interfere, carrying an intensity I_{out} out of the beamsplitter.

In order to account for losses in the system, assume that the beamsplitter has

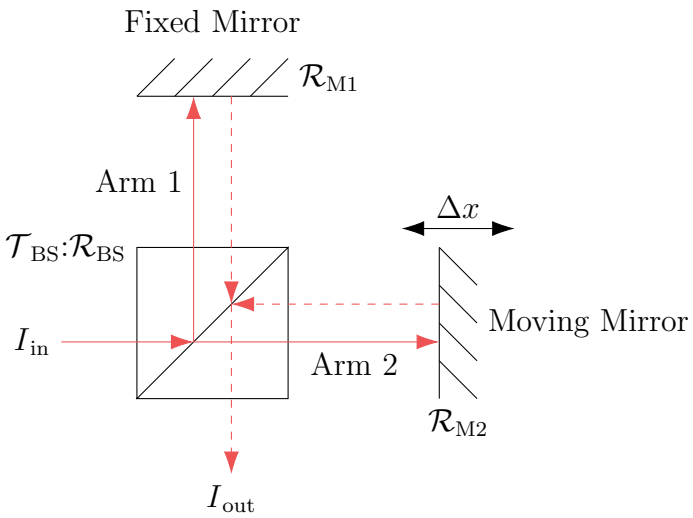

Figure 3.8: A Michelson interferometer.

transmittance and reflectance, $\mathcal{T}_{\mathrm{BS}}$ and $\mathcal{R}_{\mathrm{BS}}$, respectively, and that top and right mirrors have reflectance, $\mathcal{R}_{\mathrm{M1}}$ and $\mathcal{R}_{\mathrm{M2}}$, respectively. It is assumed that $\mathcal{T}_{\mathrm{BS}}$ and $\mathcal{R}_{\mathrm{BS}}$ are the same for light entering from any direction, and do not exhibit any polarization dependence. While losses due to absorption in the beamsplitter are not explicitly accounted for, absorption is implicitly considered by requiring that $\mathcal{T}_{\mathrm{BS}} + \mathcal{R}_{\mathrm{BS}} \leq 1$. In Figure 3.8, the beam travelling through the first arm undergoes one reflection at the beamsplitter, one reflection at the fixed mirror, and one transmission at the beamsplitter. Similarly, the beam through the second arm undergoes one transmission at the beamsplitter, one reflection at the moving mirror, and one reflection at the beamsplitter. Since the input beam undergoes the similar transmissions and reflections in each interferometer arm, the relationship of the input intensity and the final intensities from each arm, I_1 and I_2, that interfere to form I_{out}, is

$$I_1 = \mathcal{T}_{\mathrm{BS}}\mathcal{R}_{\mathrm{BS}}\mathcal{R}_{\mathrm{M1}}I_{\mathrm{in}}, \qquad [\mathrm{W/m^2}] \quad (3.38a)$$

$$I_2 = \mathcal{T}_{\mathrm{BS}}\mathcal{R}_{\mathrm{BS}}\mathcal{R}_{\mathrm{M2}}I_{\mathrm{in}}. \qquad [\mathrm{W/m^2}] \quad (3.38b)$$

Initially, the moving mirror is an equal distance from the beamsplitter as the fixed mirror. This condition is called zero path difference (ZPD), because the optical path length that light travel in each arm is equal; thus the OPD between the two mirrors is zero. When the mirror is displaced by Δx, the OPD, Λ, is

$$\Lambda = 2\Delta x, \qquad [\mathrm{m}] \quad (3.39)$$

with the factor of 2 to account for light travelling once toward the mirror and once away from it, and the phase difference between the two beams in the interferometer is

$$\Delta\phi = 2\pi\frac{\Lambda}{\lambda}. \qquad [\mathrm{rad}] \quad (3.40)$$

Equations 3.34, 3.38, and 3.40 can be used to model this interferometer, leading to

$$\begin{aligned} I_{\text{out}} &= I_1 + I_2 + 2\sqrt{I_1 I_2}\cos\left(2\pi\frac{\Lambda}{\lambda}\right) \\ &= \mathcal{T}_{\text{BS}}\mathcal{R}_{\text{BS}} I_{\text{in}}\left[\mathcal{R}_{\text{M1}} + \mathcal{R}_{\text{M2}} + 2\sqrt{\mathcal{R}_{\text{M1}}\mathcal{R}_{\text{M2}}}\cos\left(2\pi\frac{\Lambda}{\lambda}\right)\right]. \end{aligned} \qquad [\text{W/m}^2] \quad (3.41)$$

From Equation 3.41, the maximum and minimum intensity is

$$I_{\text{max}} = \mathcal{T}_{\text{BS}}\mathcal{R}_{\text{BS}} I_{\text{in}}\left[\mathcal{R}_{\text{M1}} + \mathcal{R}_{\text{M2}} + 2\sqrt{\mathcal{R}_{\text{M1}}\mathcal{R}_{\text{M2}}}\right], \qquad [\text{W/m}^2] \quad (3.42a)$$

$$I_{\text{min}} = \mathcal{T}_{\text{BS}}\mathcal{R}_{\text{BS}} I_{\text{in}}\left[\mathcal{R}_{\text{M1}} + \mathcal{R}_{\text{M2}} - 2\sqrt{\mathcal{R}_{\text{M1}}\mathcal{R}_{\text{M2}}}\right], \qquad [\text{W/m}^2] \quad (3.42b)$$

which are the intensities of the bright and dark fringes, respectively.

Bright and dark fringes are then observed at specific positions in the OPD. For an integer, m, bright fringes occur in the OPD at integer multiples of λ, $\Lambda = m\lambda$, while dark fringes occur at half integer multiples, $\Lambda = \left(m + \frac{1}{2}\right)\lambda$, which take on intesnties I_{max} and I_{min}, respectively. Note that ZPD is a special case where $m = 0$, therefore, ZPD will always have the maximum intensity, I_{max}. An illustration of the bright and dark fringe locations is shown in Figure 3.9.

Figure 3.9 demonstrates that a Michelson interferometer with a single beam naïvely encodes displacement information. By tracking the bright and dark fringes, one is able to measure the distance that the mirror travels, however, the direction of travel is

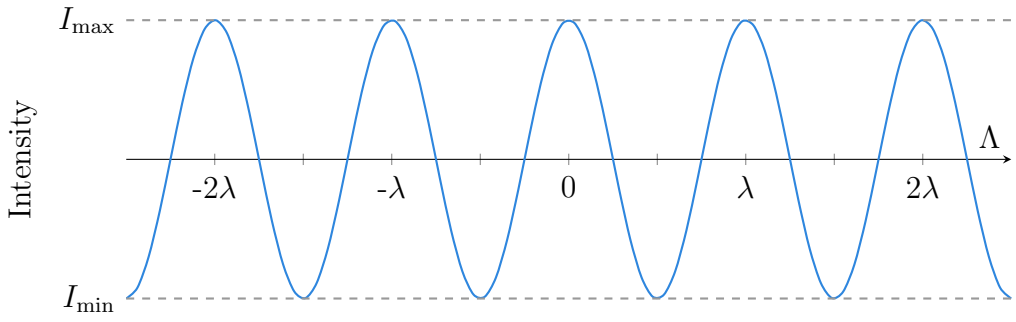

Figure 3.9: Fringes from a Michelson interferometer.

unknown, so the displacement cannot be measured. In order to measure displacement, additional information must be encoded into the probing beam.

3.2 Quadrature Encoding

In the most general terms, a quadrature signal represents a relative quantity as a continuous data stream using the phase shared by a sine and a cosine. Any quadrature measurement is necessarily relative. Because a quadrature signal is a stream that encodes changes in a quantity over time, it is not possible to represent a quantity in absolute terms. To illustrate, consider a stepper motor. Stepper motors are typically quadrature encoded, and a quadrature signal is given to step the motor to a new position from its current position. For example, a signal may be used to give the instructions, "rotate 3/4 of a turn anticlockwise from the current position." However, due to the relative nature of quadrature encoding, it is not possible to deliver a quadrature signal with the command, "rotate to an angle of exactly $3\pi/2$," as quadrature encoding itself has no notion of an absolute quantity.

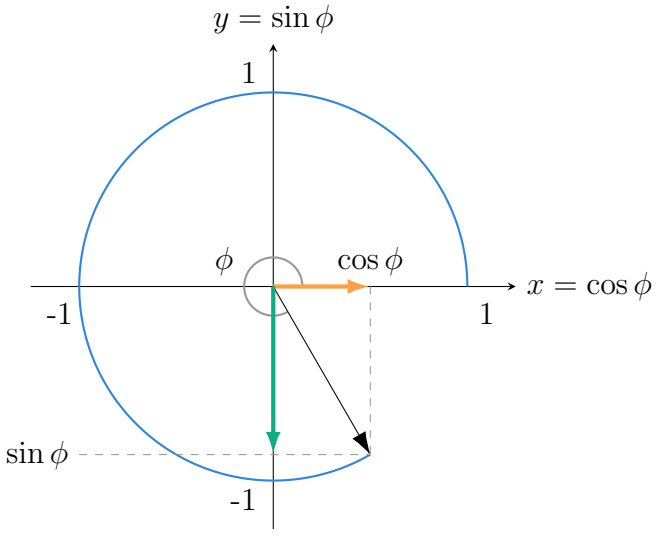

Figure 3.10: A quadrature encoded phase of $\phi = 5\pi/3$ on the unit circle. The quadrature vectors on the x and y axes sum to the encoded phase vector at an angle ϕ.

In order to model a quadrature system, imagine for a moment a sine and a cosine with a shared phase term, ϕ. These two sinusoids represent a parametric equation in cartesian coordinates, x and y,

$$\begin{cases} x = \cos\phi \\ y = \sin\phi \end{cases} \quad \phi \in (-\infty, \infty). \qquad \text{[rad]} \quad (3.43)$$

A more digestible form of Equation 3.43 is to consider the system in polar coordinates, where the angle is ϕ and the radius is a constant (with a value of 1), as shown in Figure 3.10. In this case, when given the values of x and y, ϕ can be recovered by an arctangent:

$$\phi = \arctan\frac{y}{x} = \arctan\frac{\sin\phi}{\cos\phi} = \arctan\left(\tan\phi\right). \qquad \text{[rad]} \quad (3.44)$$

One challenge with Equation 3.44 is that arctangent produces a value in the interval $(-\pi, \pi]$, where the value of ϕ can take any real number. In Figure 3.10, a phase of $\phi = 5\pi/3$ is shown, however, there are infinitely many angles that could be used to produce the same curve, $\phi = 5\pi/3 + 2m\pi$ for any $m \in \mathbb{Z}$. From a single arctangent, it is impossible to know the absolute phase in an open interval, but with a stream of phase values, phase unwrapping can be performed to accumulate a large change in phase from a reference starting value. Using Equation 3.44 to convert a quadrature stream to a phase stream indexed by m, the unwrapped phase, ϕ_{unwrap}, is

$$\phi_{\text{unwrap},m} = \begin{cases} \phi_m & m = 0 \\ \phi_{\text{unwrap},m-1} + (\phi_m - \phi_{m-1}) + 2\pi & \phi_m - \phi_{m-1} < -\pi \\ \phi_{\text{unwrap},m-1} + (\phi_m - \phi_{m-1}) - 2\pi & \phi_m - \phi_{m-1} > \pi \\ \phi_{\text{unwrap},m-1} + (\phi_m - \phi_{m-1}) & \text{otherwise.} \end{cases} \qquad \text{[rad]} \quad (3.45)$$

Phase unwrapping through Equation 3.45 decodes a quadrature stream into a stream of phase values. It is important to note that phase unwrapping produces a continuous signal, which is no longer bound by a modulus of 2π. Since this signal belongs to the open interval $(-\infty, \infty)$, it encodes any displacement over an infinite range.

Quadrature encoding is angular by definition, and a conversion is necessary to

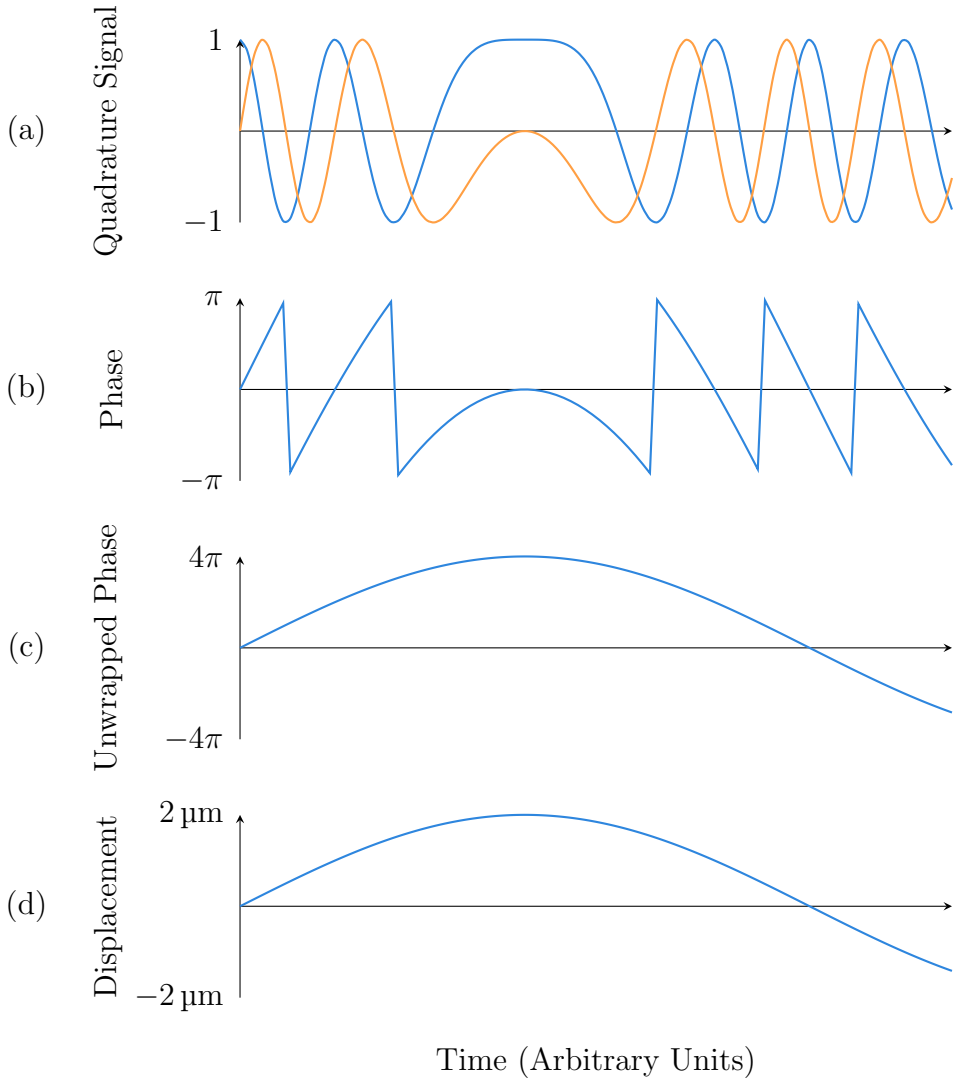

Figure 3.11: Conversion from a quadrature signal to displacement using $k = 2\pi\ \mu\text{m}^{-1}$. In (a), the quadrature signal is shown (cosine and sine are blue and orange, respectively), which encodes the phase in (b). Phase unwrapping gives the unwrapped phase in (c), from which displacement in (d) is found.

recover a displacement. In general terms, Equation 3.10 shows the angular spatial frequency vector, $\vec{k}$, of a wave travelling in an arbitrary-dimensional space. For this analysis, the scalar angular spatial frequency, k, described by

$$k = \left|\vec{k}\right| = \frac{2\pi}{\lambda}, \qquad \text{[rad/m]} \quad (3.46)$$

is required. The displacement, Δx, is related to the unwrapped phase and k by the following equation:

$$\Delta x = \frac{\phi_{\text{unwrap}}}{k}. \qquad \text{[m]} \quad (3.47)$$

As an illustration, suppose that a Michelson interferometer is set up to produce a quadrature signal with a 1 µm monochromatic source. The displacement in OPD of the moving mirror is encoded in this quadrature signal, and the angular spatial frequency would be $k = 2\pi\,\mu\text{m}^{-1}$. For this signal, the conversion from the quadrature signal to displacement is shown in Figure 3.11.

The fringe rate, f_{fr}, of the quadrature signal depends on the wavelength, λ, of the laser and the velocity, v, of the moving mirror.

$$f_{\text{fr}} = \left|\frac{2v}{\lambda}\right|. \qquad \text{[Hz]} \quad (3.48)$$

In order for a system to accurately track displacement, the sampling frequency, f_{s}, must be at least twice f_{fr}, called the Nyquist frequency [59]. Therefore, the maximum tolerable instantaneous velocity, v_{max}, can be formulated as

$$v_{\text{max}} = \frac{1}{4}\lambda f_{\text{s}}. \qquad \text{[m/s]} \quad (3.49)$$

Considering realistic values of $\lambda = 1550\,\text{nm}$ and $f_{\text{s}} = 1\,\text{MHz}$, Equation 3.49 imposes the restriction $v_{\text{max}} = 38.75\,\text{cm/s}$. Although this v_{max} may seem large, it is the maximum tolerable *instantaneous* velocity, which is more readily achieved than

average velocity over a range of travel. When such high instantaneous velocities are involved, decoding a rapidly changing displacement may require the use of specialized high-speed hardware.

3.3 Field-Programmable Gate Arrays

Due to their performance and flexibility, field-programmable gate arrays (FPGA) are now commonplace in digital signal processing (DSP) applications. FPGAs represent a class of reconfigurable hardware which can be programmed for the needs of a specific application [60, 61]. Configurables are not only intrinsically parallelized, but parallelized at the hardware level, leading to a large potential for performance improvements over conventional processors.

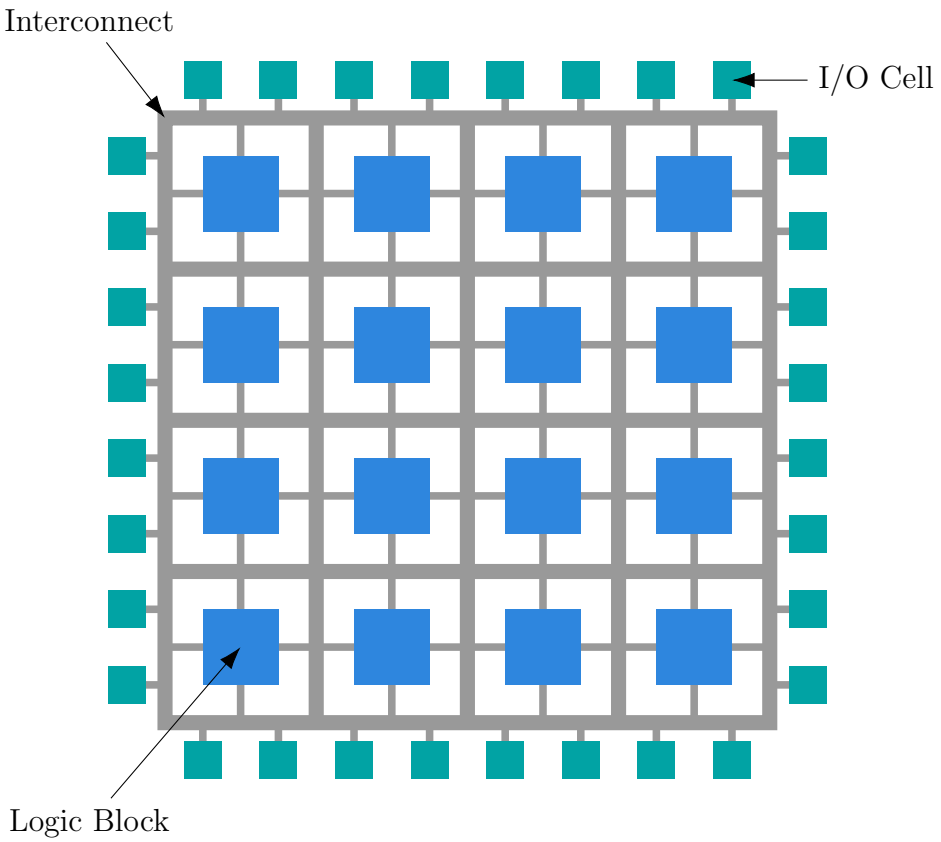

Figure 3.12: The fabric of an FPGA.

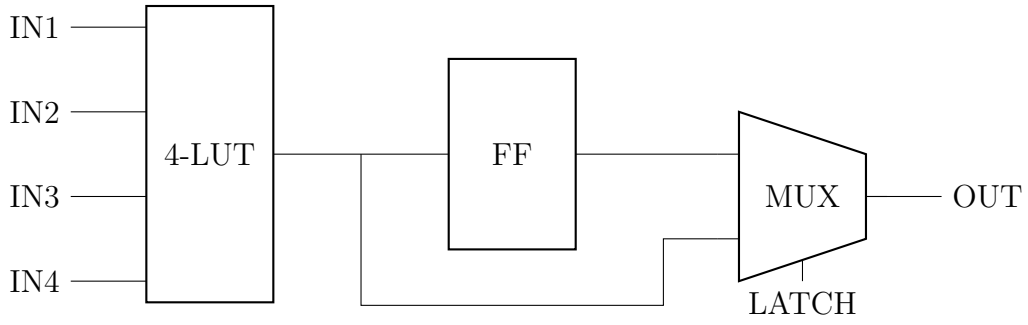

Figure 3.13: One possible structure of a logic block. Clocking is omitted for simplicity.

The fabric of an FPGA is shown in Figure 3.12. An interconnect provides routing for signals, such as data and clocks, between components on the die, and I/O cells enable unidirectional and bidirectional ports from off-chip to the FPGA logic through the interconnect. Logic blocks form the basis of tangible computational power in two ways: each block is configured to implement a small part of the overall logic, and logic requiring many logic blocks are implemented by cascaded logic blocks through the interconnect.

There are many ways to design a logic block, meaning there is no standard structure. Despite a lack of convention, one way to visualize the behaviour of a logic block is through look-up table (LUT), flip-flop (FF), and multiplexer (MUX) primitives.

Figure 3.13 shows the contents of a logic block model. For this logic block, both the LUT and the LATCH input into the MUX are configurable. LUTs are the primary units which implement logic and are a realization of a truth table determined during logic synthesis. A 4-LUT, such as the one presented in Figure 3.13, can implement any logic expression of four or fewer variables. The FF stage of a logic block is used as a local storage for the LUT output. In tandem with the MUX, the LUT and FF may be used as either a function, register, or a combination of both.

FPGAs are not limited to only these resources. In certain applications, higher level structures such as first-in first-out (FIFO) queues or random access memories (RAM) may be required for temporal or spatial optimizations. Typically structures like these

will be backed by another primitive, block random access memories (BRAM), which are "baked into" the interconnect. On a high-level, BRAMs behave similarly to RAM, but since it is part of the die, BRAM accesses are much lower latency than RAM accesses which must go off chip. The importance of BRAMs is that they allow for performant storage and retrieval of high volumes of data without contributing to logic block utilization. A practical example of where BRAMs are used in this work is for storing tables of precomputed values and buffering and delaying data streams.

Another important resource is the DSP slice, which implements dedicated high speed multiplication, addition, and accumulation. Of course, the equivalent operations could be implemented in fabric using LUTs, but at the cost of reduced performance and increased power consumption. DSP slices are key to high-speed signal processing, allowing compound expressions such as $(a + b) \times c$ to be completed in a single clock cycle.

3.3.1 Multi-Processor Systems-on-Chip

Improvements in configurable logic allow for even more versatility through traditional computer processors implemented in FPGA fabrics, called *soft processors*. Soft processors improve accessibility to FPGAs in the sense that the development overhead is reduced. A system with an implemented soft processor may be programmed in a higher level language, such as C, while performance critical logic is implemented in the fabric. Such designs are limiting, since they require fabric resources be sacrificed to support a soft processor.

Multi-processor systems-on-chip (MPSoC) solve this issue by integrating a multiprocessor and an FPGA fabric into the same die [66]. This architecture allows for an interconnect between all components of the chip, meaning that peripherals such as RAM, serial interfaces, Ethernet ports, and others can be shared between the processor and FPGA, as illustrated in Figure 3.14. In addition, interrupts and high-

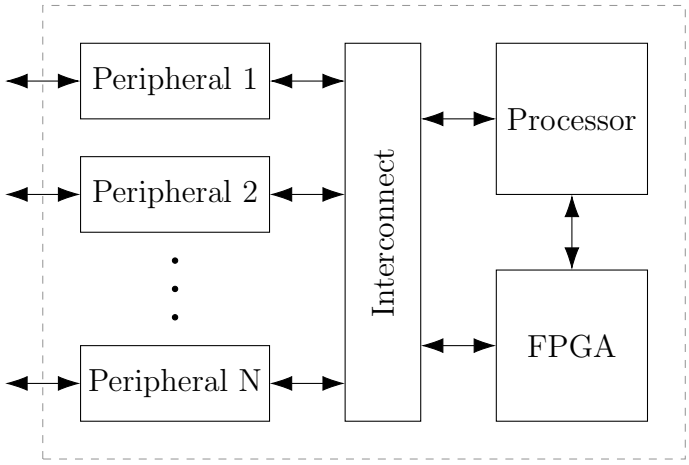

Figure 3.14: General architecture of an MPSoC.

speed traffic between the processor and the FPGA may bypass the interconnect.

Throughput and latency requirements are key drivers for adopting a hardware-based DSP system. Due to the intrinsic parallelism of an FPGA, throughputs on the order of Gb/s are achievable on low-cost devices. For many applications, this kind of performance is not possible on conventional processors which are limited by the number of possible concurrent processes. A position metrology system must also achieve low latency in order to minimize the delay between a displacement and the instant that it is reported. Thus, the FPGA selected for this work is a Xilinx Artix-7

Table 3.1: Specifications of the selected FPGA and MPSoC evaluation boards [62–65].

	FPGA	MPSoC
Board	Digilent Arty A7-100T	Digilent Cora Z7-10
FPGA/MPSoC Part	XC7A100TCSG324-1	XC7Z010-1CLG400C
On-chip ADC	12-bit, 1 MHz	12-bit, 1 MHz
LUTs	63400	17600
FFs	126800	35200
BRAM	608 kB	270 kB
DSP Slices	240	80
Max Fabric Clock	450 MHz	450 MHz
RAM	256 MB	512 MB
Accessible I/O Pins	77	75
Processor	—	Dual Core ARM Cortex-A9

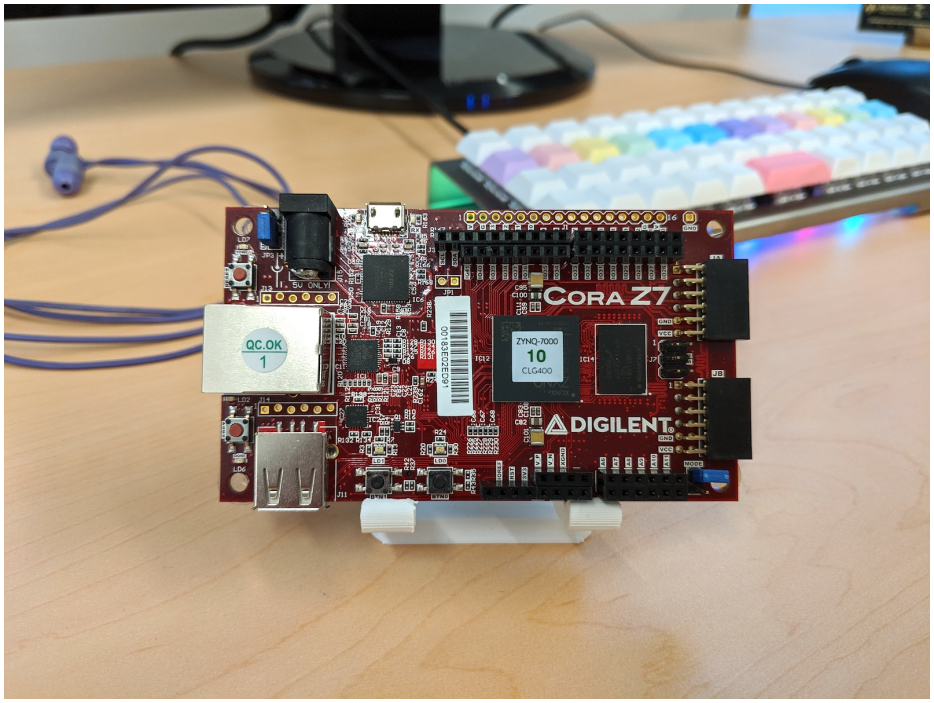

Figure 3.15: A Digilent Cora Z7-10 FPGA [64].

Series FPGA designed for low-latency signal processing [63], and the MPSoC is a Xilinx Zynq-7000 with a fabric equivalent to that of a low grade Artix-7 [65], both on low-cost Digilent evaluation boards [62,64]. The specifications of these two boards are compared in Table 3.1. A Digilent Cora Z7-10 with a Xilinx MPSoC is shown in Figure 3.15.

3.4 Conclusions

In this chapter I have provided background and an overview of the practical issues and considerations for the development of a range-resolved laser interferometer. This includes an introduction to photonics, Gaussian beam optics, quadrature position encoding, and FPGA hardware.

Chapter 4

Three-Phase Cryogenic Interferometry

In Chapter 2, a review of cryogenic position metrology systems was presented. Range-resolved interferometry was determined to be a desirable approach for the SAFARI instrument. It must be appreciated that to perform position metrology at cryogenic temperatures, the instrument itself must not only survive extreme conditions, but also be designed such that physical changes in the instrument caused by the cryogenic environment have minimal effect on its operation.

4.1 Theory

In this section, the foundations of three-phase range-resolved interferometry will be introduced. These foundations form the basis for the interferometer design and implementation.

4.1.1 Underlying Mathematics of Three-Phase Position Encoding

Displacement information can be quadrature encoded (covered in Section 3.2), although in the general case a minimum of any two sinusoids can be used. In the design of a three-phase interferometer, we will consider an encoding scheme based on three sinusoids. Consider three-phase signals, U_{a}, U_{b}, and U_{c}, each sharing the same OPD dependent phase term, ϕ_{Λ}, but with different individual phases, ϕ_{b} and

ϕ_c, measured relative to the phase of U_a. They can be expressed in matrix form as

$$\begin{bmatrix} U_a \\ U_b \\ U_c \end{bmatrix} = \begin{bmatrix} \cos(\phi_\Lambda) \\ \cos(\phi_\Lambda + \phi_b) \\ \cos(\phi_\Lambda + \phi_c) \end{bmatrix}. \tag{4.1}$$

In principle, all three phases can take any value as long as they are each unique among themselves. However, in the case that all phases are unique integer multiples of $2\pi/3$, solving for displacement is greatly simplified. This is the principle that I have used in this chapter, where ideally

$$\begin{bmatrix} U_a \\ U_b \\ U_c \end{bmatrix} = \begin{bmatrix} \cos(\phi_\Lambda) \\ \cos(\phi_\Lambda + 2\pi/3) \\ \cos(\phi_\Lambda - 2\pi/3) \end{bmatrix}. \tag{4.2}$$

U_a, with a phase of zero, is considered to be the reference signal. Relative to U_a, the

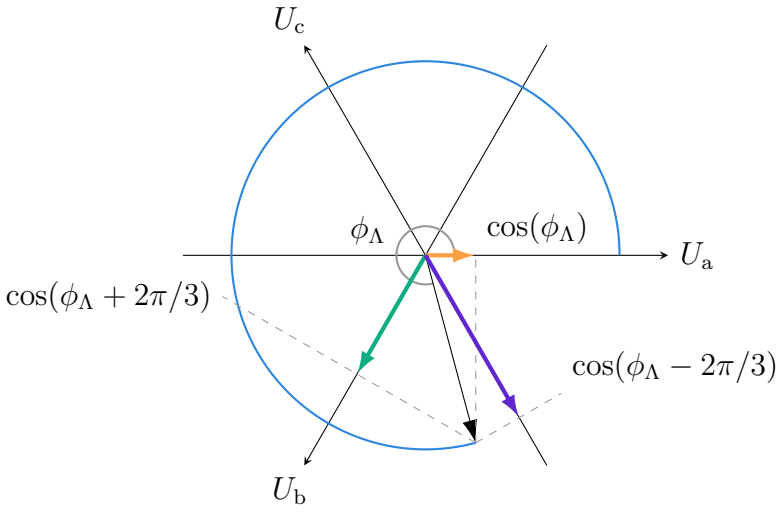

Figure 4.1: An example of a three-phase encoded OPD of $\phi_\Lambda = 19\pi/12$ on the unit circle. The three-phase vectors on the U_a, U_b, and U_c axes sum to the encoded phase vector at an angle ϕ_Λ. The magnitude of resultant vector is scaled by 2/3 so that it can be drawn on the unit circle along with the three-phase vectors.

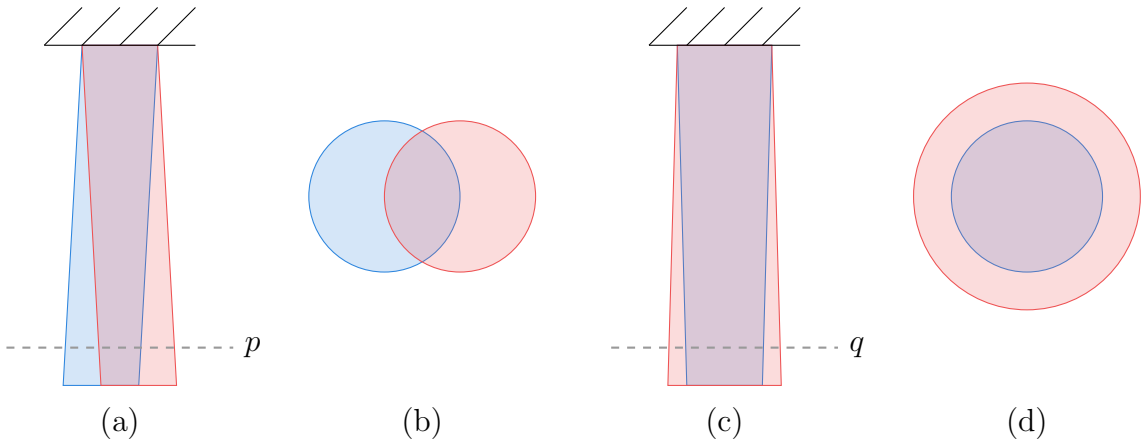

Figure 4.2: Shearing and dilution comparing the incident beam (blue) to the reflected beam (red) from a plane mirror. Beam shearing is shown from a side view in (a) with the resulting overlap at the plane p in (b). Dilution is shown from a side view in (c) with the resulting overlap at the plane q in (d).

leading signal is U_{b} and the lagging signal is U_{c}.

In a similar fashion to quadrature encoding on the unit circle in Figure 3.10, the illustration in Figure 4.1 shows the three-phase axes separated by $2\pi/3$, which encode phase as a sum of three-phase vectors. Note that the encoded phase vector length is scaled by $2/3$, which will become apparent from the discussion of Equation 4.12.

Despite Equation 4.2 showing the definition of ideal normalized three-phase signals, in practice, it is unlikely that the phases will be $2\pi/3$, and the signals will carry non-unity amplitudes and non-zero offsets, which may themselves vary with displacement. Both of these are physical consequences that will be discussed in terms of measuring the displacement of a single arm in a Michelson interferometer, whose configuration was shown in Figure 3.8. The system is a photonic device, which will have both optical and electrical aspects that must be considered.

Due to the number of electrical and optical effects under consideration, the nomenclature can quickly become unwieldly. In this section, all signals are represented by U accompanied by a subscript to provide additional context. Subscripts adhere to the following set of naming rules:

- U_{op} denotes an optical signal.
- U_{el} denotes an electrical signal.
- U_{co} denotes an optically coupled signal.
- U_{at} denotes an optically attenuated signal.
- U_{gn} denotes gain.
- U_{of} denotes offset.
- U_{a}, U_{b}, U_{c}, or U_x denote a reference, leading, lagging, or arbitrary signal, respectively.

Optical attenuations are due to coupling, shearing, and dilution, illustrated in Figure 4.2. The three-phase signals will experience attenuations, $U_{\text{op,co,at,a}}$, $U_{\text{op,co,at,b}}$, and $U_{\text{op,co,at,c}}$, due to the coupling efficiencies when splitting a single signal into three. Shearing and dilution are OPD dependent phenomena which affect each signal equally by an envelope of $U_{\text{op,at}}(\Lambda)$. Shearing is caused by misalignment of components affecting the beam overlap, while dilution due to Gaussian beam expansion may be present in the absence of shearing. The consequence of shearing and dilution are seen through Equation 3.37 as a reduction in fringe visibility, which is in effect a variation in gain with displacement resulting from optical effects.

Electrical gains in the photodetection circuitry contribute unique signal gains, $U_{\text{el,gn,a}}$, $U_{\text{el,gn,b}}$, and $U_{\text{el,gn,c}}$, and offsets, $U_{\text{el,of,a}}$, $U_{\text{el,of,b}}$, and $U_{\text{el,of,c}}$.

The three-phase signal definition in Equation 4.1 is modified to include optical and electrical effects in the system. Each signal experiences an equal optical attenuation, $U_{\text{op,at}}$, and optical offset, $U_{\text{op,of}}$, however, electrical and coupler effects are signal specific. For example, U_{a} experiences a net gain of $U_{\text{el,gn,a}}U_{\text{op,co,at,a}}$ and offset of $U_{\text{el,of,a}}$. Accounting for these parameters, the full definition for the sampled

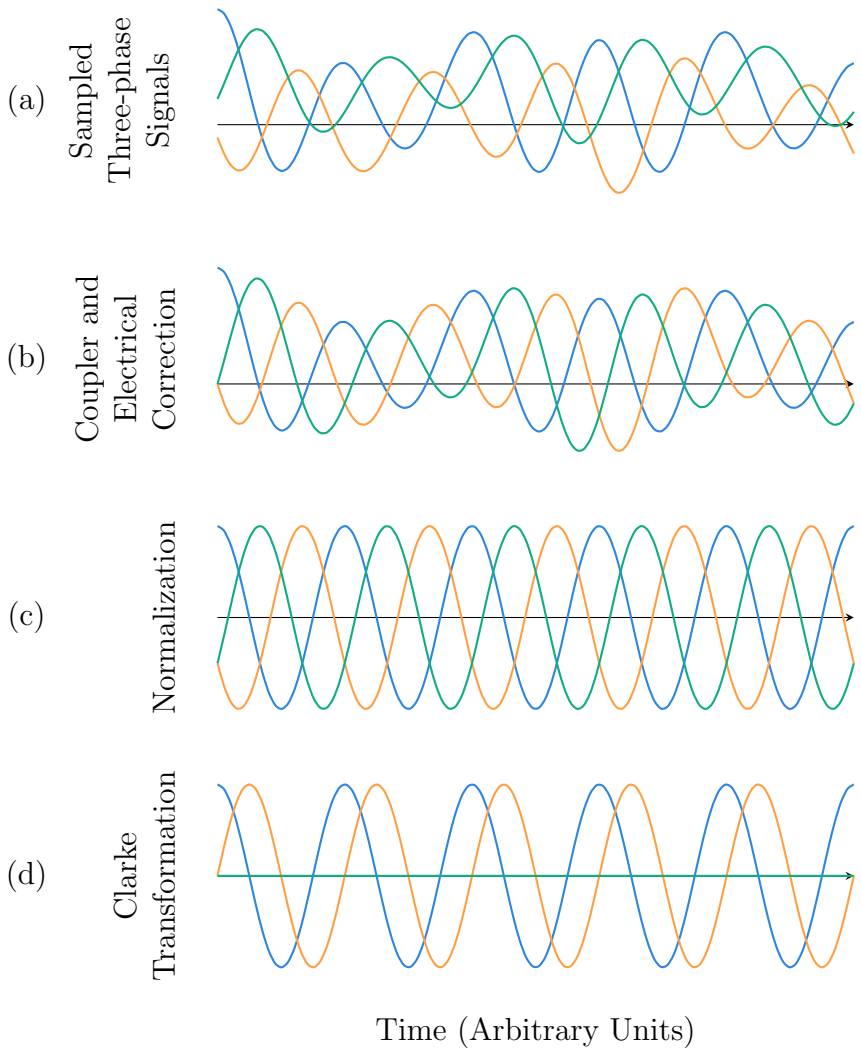

Figure 4.3: An overview of the three-phase quadrature recovery process. In (a), three-phase signals are shown as measured by independent detectors with their own gain and offset. Removal of electrical gain and coupler attenuation is shown in (b), and the further removal of optical attenuations and offsets to produce the visibility normalized signals in (c). A quadrature signal is recovered from (c) using the Clarke transformation (see text for details) and shown in (d).

three-phase signals is determined,

$$\begin{bmatrix} U'_{\mathrm{a}} \\ U'_{\mathrm{b}} \\ U'_{\mathrm{c}} \end{bmatrix} = \begin{bmatrix} U_{\mathrm{el,gn,a}} U_{\mathrm{op,co,at,a}} \left[U_{\mathrm{op,at}} \left(\Lambda \right) \cos \left(\phi_{\Lambda} \right) + U_{\mathrm{op,of}} \right] + U_{\mathrm{el,of,a}} \\ U_{\mathrm{el,gn,b}} U_{\mathrm{op,co,at,b}} \left[U_{\mathrm{op,at}} \left(\Lambda \right) \cos \left(\phi_{\Lambda} + \phi_{\mathrm{b}} \right) + U_{\mathrm{op,of}} \right] + U_{\mathrm{el,of,b}} \\ U_{\mathrm{el,gn,c}} U_{\mathrm{op,co,at,c}} \left[U_{\mathrm{op,at}} \left(\Lambda \right) \cos \left(\phi_{\Lambda} + \phi_{\mathrm{c}} \right) + U_{\mathrm{op,of}} \right] + U_{\mathrm{el,of,c}} \end{bmatrix}. \tag{4.3}$$

The attenuation $U_{\mathrm{op,at}}$ directly affects the interference signal, while $U_{\mathrm{el,gn,a}}U_{\mathrm{op,co,at,a}}$ represent combined effects of the optical system after interference and throughout photodetection. For this reason, $U_{\mathrm{op,at}}$ is applied before $U_{\mathrm{el,gn,a}}U_{\mathrm{op,co,at,a}}$ in Equation 4.3. Equations 4.2 and 4.3 are both describing a three-phase system, although Equation 4.3 highlights the complexity introduced when considering physical effects of the system.

Ultimately, a quadrature signal is extracted using Equation 4.3. The processing stages are summarized in Figure 4.3, which demonstrates the transformations to the three-phase signals at each step, and the model Equation 4.3 is shown in Figure 4.3a.

4.1.2 Correction of Optical Coupling Attenuation and Electrical Gain

The linearity of coupling attenuation and electrical gain allows for correction via a naïve calibration procedure. Assuming that the interferometer presented in Figure 3.8 is used, the first step of the procedure is to translate the moving mirror over its entire range, and record the minimum and maximum power of U'_{a}, U'_{b}, U'_{c}. Assuming the power of the input source does not change, none of the three-phase signals will take on a value outside of its recorded interval. Given an arbitrary three-phase signal from Equation 4.3, U'_x, the values of $U_{\mathrm{el,gn},x}U_{\mathrm{op,co,at},x}$ and $U_{\mathrm{el,of},x}$ are computed by

$$U_{\mathrm{el,gn},x}U_{\mathrm{op,co,at},x} = \frac{\max\left(U'_x\right) - \min\left(U'_x\right)}{2}, \tag{4.4a}$$

$$U_{\mathrm{el,of},x} = \frac{\max\left(U'_x\right) + \min\left(U'_x\right)}{2}. \tag{4.4b}$$

Using this strategy, values for $U_{\mathrm{el,gn},x}$ and $U_{\mathrm{op,co,at},x}$ cannot be computed, only the product $U_{\mathrm{el,gn},x}U_{\mathrm{op,co,at},x}$ is determined. Knowledge of these values on their own is not necessary, as they only exist as their product in Equation 4.3. Nevertheless, the calibration values obtained from Equation 4.4 allow for the signal to be partially

corrected by applying

$$U''_x = \frac{U'_x - U_{\mathrm{el,of},x}}{U_{\mathrm{el,gn},x} U_{\mathrm{op,co,at},x}}, \tag{4.5}$$

through the removal of electrical gains and coupler attenuations. The correction process is equivalent to projecting the signal into the interval $[U_{\mathrm{op,at}}(\Lambda) + U_{\mathrm{op,of}}, U_{\mathrm{op,at}}(\Lambda) - U_{\mathrm{op,of}}]$. The application of Equations 4.4 and 4.5 to the model signals in Equation 4.3 produces the partially corrected signals

$$\begin{bmatrix} U''_{\mathrm{a}} \\ U''_{\mathrm{b}} \\ U''_{\mathrm{c}} \end{bmatrix} = \begin{bmatrix} U_{\mathrm{op,at}}(\Lambda)\cos(\phi_\Lambda) + U_{\mathrm{op,of}} \\ U_{\mathrm{op,at}}(\Lambda)\cos(\phi_\Lambda + \phi_{\mathrm{b}}) + U_{\mathrm{op,of}} \\ U_{\mathrm{op,at}}(\Lambda)\cos(\phi_\Lambda + \phi_{\mathrm{c}}) + U_{\mathrm{op,of}} \end{bmatrix}, \tag{4.6}$$

shown in Figure 4.3b.

4.1.3 Visibility Normalization

Normalization corrects for the change in visibility with OPD by establishing two invariants for each three-phase signal in the ideal case: the amplitude is unity and offset is zero. Effectively, the normalization process removes the signal envelope. These transformations are necessary to recover the encoded displacement and are performed using a memoryless procedure that exploits two essential three-phase properties.

Instantaneous Zero-sum Property

At any instant, the sum of three-phase signals is zero. Consider three-phase signals in an analogous physical system as a set of electrical signals, specifically, in a loop with a three-phase source providing power to a balanced load. Electrical engineering nomenclature will be used, where three-phase power systems are common and the terms *hot* and *neutral* describe wires which deliver current to a source and provide a return path for the current, respectively. This circuit is constructed in a Y configuration, as shown in Figure 4.4, where three hot currents I_{a}, I_{b}, and I_{c}, and a neutral

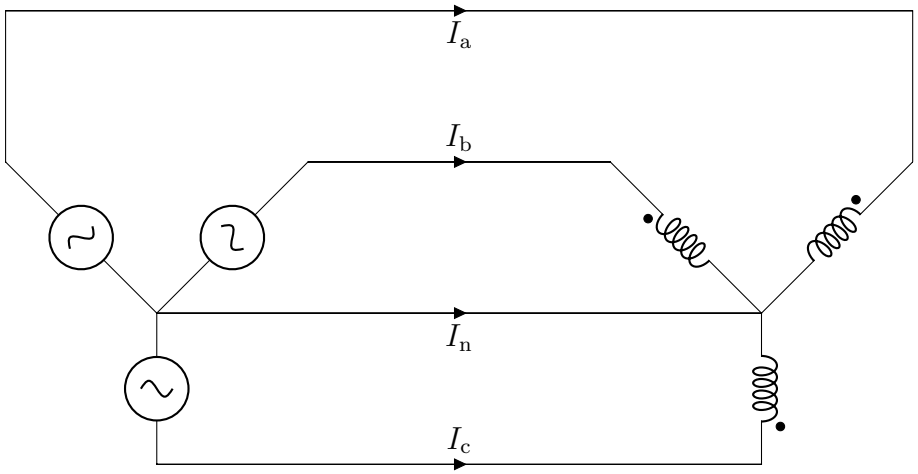

Figure 4.4: A three-phase circuit in Y configuration. Power is delivered to the load on the right from the three-phase source on the left.

current, I_n, are provided to a load. There is a time-dependent current distribution in I_a, I_b, and I_c, however, conservation of energy dictates that the superposition of these three signals must satisfy $I_a + I_b + I_c = I_n = 0$, which is the instantaneous zero-sum property. It should be noted that in practice, $I_n \neq 0$, as no real three-phase system can be perfectly balanced. We will see later that the same expression holds for a three-phase interferometer in the application of a visibility normalization procedure, where instantaneous imbalances in the system are corrected.

Unlike the circuit in Figure 4.4, three-phase signals generated by an optical component will not have a neutral signal in the conventional sense. As always, conservation of energy still applies, and the generation of optical three-phase signals will have coupling inefficiencies that result in losses. Thus, the "neutral" optical three-phase signal is considered to be the sum of losses in the splitting process. Under the assumption that these losses are constant and do not vary with time, or that the time varying component of the losses are negligible, a simple normalization procedure that exploits the instantaneous zero-sum is formulated.

For any set of $N \geq 2$ sinusoids, each having the same phase term, ϕ, and each leads exactly one other signal by $2\pi/N$ and lags exactly one other signal by $2\pi/N$,

the zero-sum property,

$$\sum_{m=0}^{N-1} \cos\left(\phi + \frac{2m\pi}{N}\right) = 0, \tag{4.7}$$

holds [67]. Three-phase signals are a special case of Equation 4.7 when $N = 3$, which is canonically

$$U_{\mathrm{a}} + U_{\mathrm{b}} + U_{\mathrm{c}} = 0. \tag{4.8}$$

A natural consequence of Equation 4.8 is Equation 4.9, which is used to compute $U_{\mathrm{op,of}}$ by eliminating the sinusoidal components of the three-phase signals.

$$U_{\mathrm{op,of}} = \frac{U''_{\mathrm{a}} + U''_{\mathrm{b}} + U''_{\mathrm{c}}}{3}. \tag{4.9}$$

The optical offset is eliminated by Equation 4.9, producing a new set of three-phase signals with only the optical attenuation remaining,

$$\begin{bmatrix} U'''_{\mathrm{a}} \\ U'''_{\mathrm{b}} \\ U'''_{\mathrm{c}} \end{bmatrix} = \begin{bmatrix} U_{\mathrm{op,at}}(\Lambda)\cos(\phi_\Lambda) \\ U_{\mathrm{op,at}}(\Lambda)\cos(\phi_\Lambda + \phi_{\mathrm{b}}) \\ U_{\mathrm{op,at}}(\Lambda)\cos(\phi_\Lambda + \phi_{\mathrm{c}}) \end{bmatrix}. \tag{4.10}$$

Constant Power Property

For three-phase signals with a constant amplitude, the power delivery is constant. In fact, such a relationship is generalizable to any $N \geq 3$ sinusoids, each having the same phase term, ϕ, and each leading exactly one other signal by $2\pi/N$ and lagging exactly one other signal by $2\pi/N$. Formally, for sinusoids of unity amplitude, the relationship is

$$\sum_{m=0}^{N-1} \cos^2\left(\phi + \frac{2m\pi}{N}\right) = \frac{N}{2}. \tag{4.11}$$

This identity can describe a physical system in which N sinusoids, each with unity amplitude, and thus carrying power of $1/2$, deliver a total power of $N/2$.

The identity in Equation 4.11 does not completely model the system, since the

three-phase optical attenuation, $U_{\mathrm{op,at}}$, is an OPD varying signal. A generalization of Equation 4.11 can include an envelope for each sinusoid, such as $U_{\mathrm{op,at}}(\Lambda)$, which then becomes

$$\sum_{m=0}^{N-1}\left[U_{\mathrm{op,at}}(\Lambda)\cos\left(\phi+\frac{2m\pi}{N}\right)\right]^2 = U_{\mathrm{op,at}}(\Lambda)^2\frac{N}{2}. \tag{4.12}$$

Three-phase signals are a specific case of Equation 4.12 when $N = 3$, which can be stated as

$$U_{\mathrm{a}}'''^2 + U_{\mathrm{b}}'''^2 + U_{\mathrm{c}}'''^2 = \frac{3}{2}U_{\mathrm{op,at}}(\Lambda)^2, \tag{4.13}$$

or more conveniently,

$$U_{\mathrm{op,at}}(\Lambda) = \sqrt{\frac{2}{3}(U_{\mathrm{a}}'''^2 + U_{\mathrm{b}}'''^2 + U_{\mathrm{c}}'''^2)}. \tag{4.14}$$

From the offset corrected three-phase signals in Equation 4.15, fully normalized three-phase signals are recoverable through division by $U_{\mathrm{op,at}}$ from Equation 4.14. The normalized form,

$$\begin{bmatrix}U_{\mathrm{a}}\\U_{\mathrm{b}}\\U_{\mathrm{c}}\end{bmatrix} = \frac{1}{U_{\mathrm{op,at}}(\Lambda)}\begin{bmatrix}U_{\mathrm{a}}'''\\U_{\mathrm{b}}'''\\U_{\mathrm{c}}'''\end{bmatrix} = \begin{bmatrix}\cos(\phi_\Lambda)\\\cos(\phi_\Lambda+\phi_{\mathrm{b}})\\\cos(\phi_\Lambda+\phi_{\mathrm{c}})\end{bmatrix}, \tag{4.15}$$

with the exception of any present phase error, is similar to the set of ideal three-phase signals presented in Equation 4.2, represented by the waveform in Figure 4.3c.

4.1.4 Clarke Transform

Although three-phase signals encode displacement information as phase, for most applications, a quadrature signal is generally preferred. The Clarke transformation, originally reported in 1943 by electrical engineer, Edith Clarke, for analyzing three-phase circuits such as Figure 4.4, converts three-phase signals into a quadrature signal

[68]. The conversion is a linear combination of three-phase signals, which is commonly represented as the 3×3 transformation matrix

$$T_{\alpha\beta 0} = \begin{bmatrix} 2/3 & -1/3 & -1/3 \\ 0 & \sqrt{3}/3 & -\sqrt{3}/3 \\ 1/3 & 1/3 & 1/3 \end{bmatrix}. \tag{4.16}$$

Conversion from three-phase to quadrature signals produces three new signals: a reference quadrature signal, U_α; a lagging quadrature signal, U_β; and a zero signal, U_0, which are

$$\begin{bmatrix} U_\alpha \\ U_\beta \\ U_0 \end{bmatrix} = T_{\alpha\beta 0} \begin{bmatrix} U_\mathrm{a} \\ U_\mathrm{b} \\ U_\mathrm{c} \end{bmatrix} = \frac{1}{3} \begin{bmatrix} 2U_\mathrm{a} - U_\mathrm{b} - U_\mathrm{c} \\ \sqrt{3}\left(U_\mathrm{b} - U_\mathrm{c}\right) \\ U_\mathrm{a} + U_\mathrm{b} + U_\mathrm{c} \end{bmatrix} = \begin{bmatrix} \cos\left(\phi_\Lambda\right) \\ \sin\left(\phi_\Lambda\right) \\ 0 \end{bmatrix}. \tag{4.17}$$

These recovered quadrature signals are presented in Figure 4.3d.

The simplicity of the Clarke transform relies on phase relationships of $2\pi/3$. While one could perform a full reconstruction of the signals in the case that they are not equally separated by $2\pi/3$, I chose to use the Clarke transform and perform an error analysis to determine the error incurred as the phase separation departs from $2\pi/3$.

There are three important observations to be made. First, $U_\alpha = U_\mathrm{a}$, which allows for optimizations in the computation. Second, $U_0 = 0$ only when all three-phase signals have identical amplitudes and perfect phase separation. Lastly, the Clarke transformation uses Equation 4.8 for the computation of U_α and U_0, although U_β requires the identity

$$\cos\phi_1 - \cos\phi_2 = -2\sin\left(\frac{\phi_1 + \phi_2}{2}\right)\sin\left(\frac{\phi_1 - \phi_2}{2}\right). \tag{4.18}$$

4.1.5 Phase Unwrapping

Through quadrature encoding, the cosine and sine components represent values on the horizontal and vertical axes of a plane, respectively, which in polar coordinates, describe an angle, ϕ_{q}, as discussed in Section 3.2. From Equation 4.17, the cosine and sine components are U_α and U_β, respectively. An arctangent is used to determine the angle prescribed by these two values, which related back to U_{a}, U_{b}, and U_{c}, becomes

$$\phi_{\mathrm{q}} = \arctan\frac{U_\beta}{U_\alpha} = \arctan\frac{(\sqrt{3}/3)\,(U_{\mathrm{b}} - U_{\mathrm{c}})}{(1/3)\,(2U_{\mathrm{a}} - U_{\mathrm{b}} - U_{\mathrm{c}})} = \arctan\frac{\sqrt{3}}{3}\frac{U_{\mathrm{b}} - U_{\mathrm{c}}}{U_{\mathrm{a}}}. \quad \text{[rad]} \quad (4.19)$$

Departures of U_{a}, U_{b}, and U_{c} from $2\pi/3$ phase separation influences uncertainty of the unwrapped phase. Uncertainty in unwrapped phase, $\delta\phi_{\mathrm{q}}$, depends on the uncertainties in phase of U_{b}, and U_{c}, which are $\delta\phi_{\mathrm{b}}$ and $\delta\phi_{\mathrm{c}}$, respectively. The error in phase of U_{a} is not considered, because it carries the phase to which U_{b} and U_{c} are referenced. Applying statistical error propagation, the equation,

$$\delta\phi_{\mathrm{q}} = \left[\left(\frac{\partial\phi_{\mathrm{q}}}{\partial\phi_{\mathrm{b}}}\right)^2 {\delta\phi_{\mathrm{b}}}^2 + \left(\frac{\partial\phi_{\mathrm{q}}}{\partial\phi_{\mathrm{c}}}\right)^2 {\delta\phi_{\mathrm{c}}}^2\right]^{1/2}, \quad \text{[rad]} \quad (4.20)$$

describes the uncertainty in unwrapped phase. The two partial derivatives in Equation 4.20 are given by:

$$\frac{\partial\phi_{\mathrm{q}}}{\partial\phi_{\mathrm{b}}} = -\frac{\sqrt{3}U_{\mathrm{a}}}{3U_{\mathrm{a}}^2 + (U_{\mathrm{b}} - U_{\mathrm{c}})^2}\sin\left(\phi_\Lambda + \phi_{\mathrm{b}}\right), \quad (4.21a)$$

$$\frac{\partial\phi_{\mathrm{q}}}{\partial\phi_{\mathrm{c}}} = \frac{\sqrt{3}U_{\mathrm{a}}}{3U_{\mathrm{a}}^2 + (U_{\mathrm{b}} - U_{\mathrm{c}})^2}\sin\left(\phi_\Lambda + \phi_{\mathrm{c}}\right). \quad (4.21b)$$

By combining Equations 4.21a and 4.21b, the full expression of phase uncertainty is

$$\delta\phi_{\mathrm{q}} = \left|\frac{\sqrt{3}U_{\mathrm{a}}}{3U_{\mathrm{a}}^2 + (U_{\mathrm{b}} - U_{\mathrm{c}})^2}\right| \sqrt{\sin^2\left(\phi_\Lambda + \phi_{\mathrm{b}}\right){\delta\phi_{\mathrm{b}}}^2 + \sin^2\left(\phi_\Lambda + \phi_{\mathrm{c}}\right){\delta\phi_{\mathrm{c}}}^2}. \quad \text{[rad]} \quad (4.22)$$

In Figure 4.5, the theoretical phase error calculated by Equation 4.22 is shown at

(a)

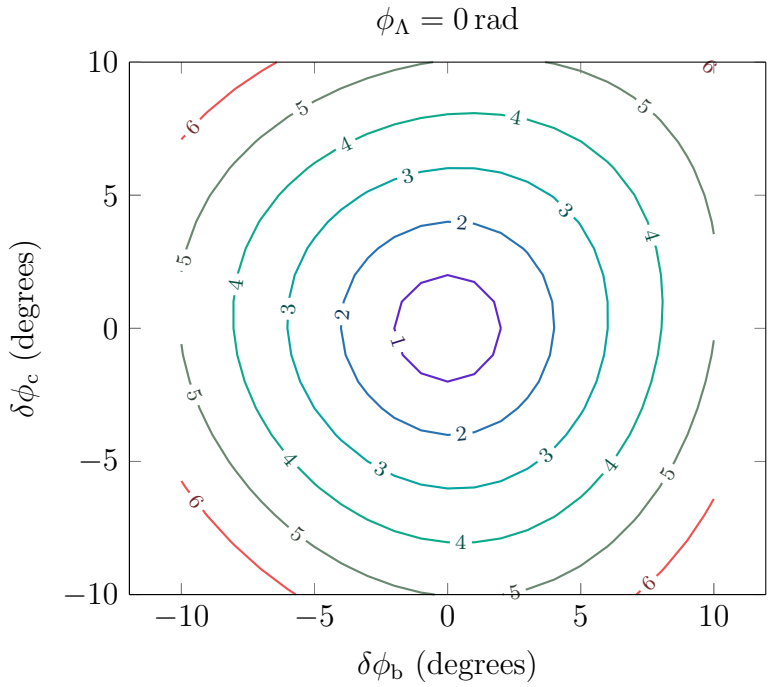

(b)

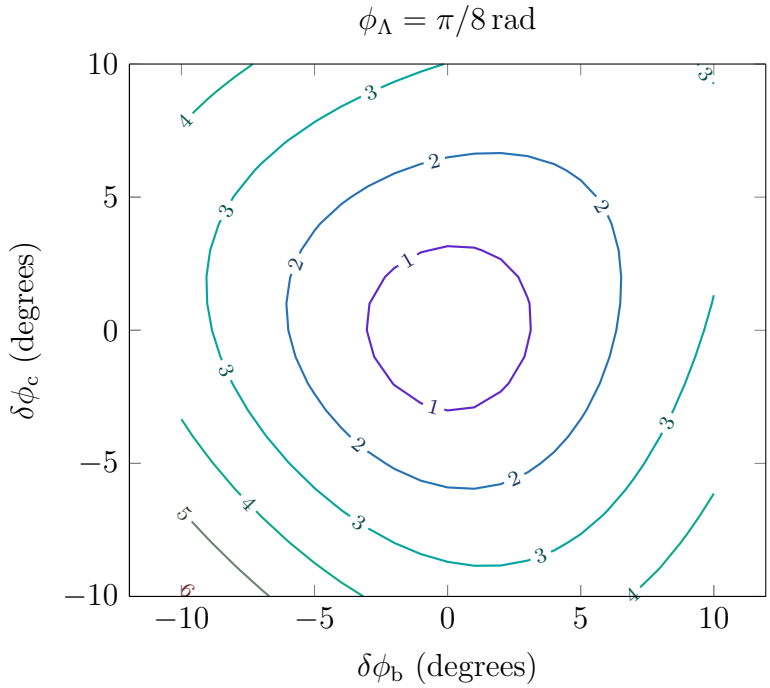

Figure 4.5: The theoretical phase errors when $\phi_\Lambda = 0\,\text{rad}$ in (a) and $\phi_\Lambda = \pi/8\,\text{rad}$ in (b). The contours show the resulting encoded phase error in units of degrees. The error varies as a function of the encoded phase, ϕ_Λ, which causes the contour bending observed in (b).

two difference OPDs, where $\phi_\Lambda = 0\,\text{rad}$ in Figure 4.5a and $\phi_\Lambda = \pi/8\,\text{rad}$ in Figure 4.5b. Figure 4.5 highlights the phase error OPD dependence, which affects the instantaneous values of U_a, U_b, and U_c. The OPD dependent effects are observed as changes in the error distribution between Figure 4.5a and Figure 4.5b.

The terms in Equation 4.22 which depend on ϕ_Λ in general cannot be computed outside of a simulation of the system, such as Figure 4.5, since ϕ_Λ is not known. As an approximation, each instance of sine squared can be replaced by $\max(\sin^2\phi) = 1$, giving

$$\delta\phi_\text{q} \approx \left|\frac{\sqrt{3}U_\text{a}}{3U_\text{a}^2 + (U_\text{b} - U_\text{c})^2}\right| \left[{\delta\phi_\text{b}}^2 + {\delta\phi_\text{c}}^2\right]^{1/2}, \qquad \text{[rad]} \quad (4.23)$$

which is an overestimate of $\delta\phi_\text{q}$. However, there is still a dependence on ϕ_Λ through U_a, U_b, and U_c. Assuming that both $\delta\phi_\text{b}$ and $\delta\phi_\text{c}$ are small, the dependence on U_a, U_b, and U_c can be removed from Equation 4.23 by rewriting $U_\text{a} \approx U_\alpha$ and $U_\text{b} - U_\text{c} = (\sqrt{3}/3)U_\beta$, leading to

$$\begin{aligned}\left|\frac{\sqrt{3}U_\text{a}}{3U_\text{a}^2 + (U_\text{b} - U_\text{c})^2}\right| &= \left|\frac{\sqrt{3}U_\alpha}{3U_\alpha^2 + 3U_\beta^2}\right| \\ &= \left|\frac{\sqrt{3}U_\alpha}{3\left(U_\alpha^2 + U_\beta^2\right)}\right| \\ &\approx \frac{\sqrt{3}}{3}\left|U_\alpha\right|.\end{aligned} \quad (4.24)$$

It can be shown that the global maximum of Equation 4.24 is

$$\max\left(\left|\frac{\sqrt{3}U_\text{a}}{3U_\text{a}^2 + (U_\text{b} - U_\text{c})^2}\right|\right) \approx \max\left(\frac{\sqrt{3}}{3}\left|U_\alpha\right|\right) \approx \frac{\sqrt{3}}{3}. \quad (4.25)$$

By combining Equations 4.23 and 4.25, the approximation

$$\delta\phi_\text{q} \approx \frac{\sqrt{3}}{3}\sqrt{{\delta\phi_\text{b}}^2 + {\delta\phi_\text{c}}^2}, \qquad \text{[rad]} \quad (4.26)$$

can be formed.

4.1.6 Displacement

The measured displacement, Δx, of the interferometer depends on two factors: the laser wavelength, λ, and the factor between the mechanical displacement and optical path length of the interferometer. For the Michelson interferometer shown in Figure 3.8, this factor is 2, since a change Δx in mechanical displacement of the moving mirror corresponds to a change of $2\Delta x$ in the optical path length. These facts lead to the definition of displacement,

$$\Delta x = \frac{1}{2}\lambda\frac{\phi_\mathrm{q}}{2\pi} = \frac{1}{4\pi}\lambda\phi_\mathrm{q}. \qquad [\mathrm{m}] \quad (4.27)$$

The leading coefficient of 1/2 in Equation 4.27 is to compensate for the factor of 2 relating mechanical displacement to optical path length. Using a statistical error analysis, the uncertainty in displacement, $\delta\Delta x$, is described by

$$\delta\Delta x = \left[\left(\frac{\partial\Delta x}{\partial\lambda}\right)^2\delta\lambda^2 + \left(\frac{\partial\Delta x}{\partial\phi_\mathrm{q}}\right)^2{\delta\phi_\mathrm{q}}^2\right]^{1/2} = \frac{1}{4\pi}\sqrt{\phi_\mathrm{q}^2\delta\lambda^2 + \lambda^2{\delta\phi_\mathrm{q}}^2}, \qquad [\mathrm{m}] \quad (4.28)$$

where $\delta\phi_\mathrm{q}$ is found by Equation 4.22. Because laser linewidths are narrow, $\delta\lambda$ will be small enough that $\phi_\mathrm{q}^2\delta\lambda^2 \ll \lambda^2{\delta\phi_\mathrm{q}}^2$. Equation 4.28 can then be expressed as the approximation

$$\delta\Delta x \approx \frac{\lambda}{4\pi}\delta\phi_\mathrm{q}. \qquad [\mathrm{m}] \quad (4.29)$$

With the approximation for $\delta\phi_\mathrm{q}$ in Equation 4.26, Equation 4.29 can be rewritten with dependence on only λ and phase errors as

$$\delta\Delta x \approx \frac{\sqrt{3}\lambda}{12\pi}\sqrt{{\delta\phi_\mathrm{b}}^2 + {\delta\phi_\mathrm{c}}^2}. \qquad [\mathrm{m}] \quad (4.30)$$

Figure 4.6 compares Equations 4.28 and 4.30. In Figure 4.6a, the theoretical error is calculated by Equation 4.28 with the wavelength $\lambda = 1550\,\mathrm{nm}$ and uncertainty $\delta\lambda = 0.01\,\mathrm{nm}$, at $\phi_\Lambda = 0\,\mathrm{rad}$. The laser specifications in Appendix A show the

(a)

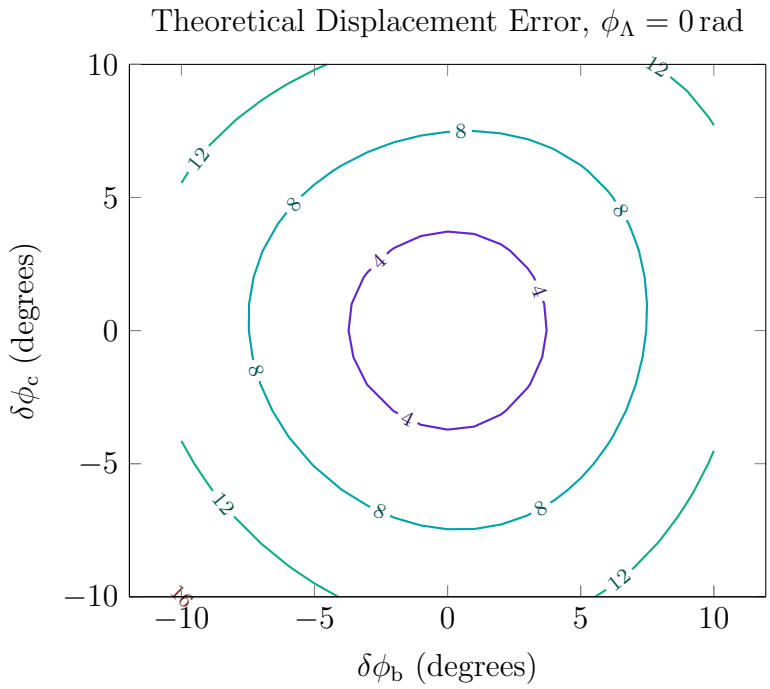

(b)

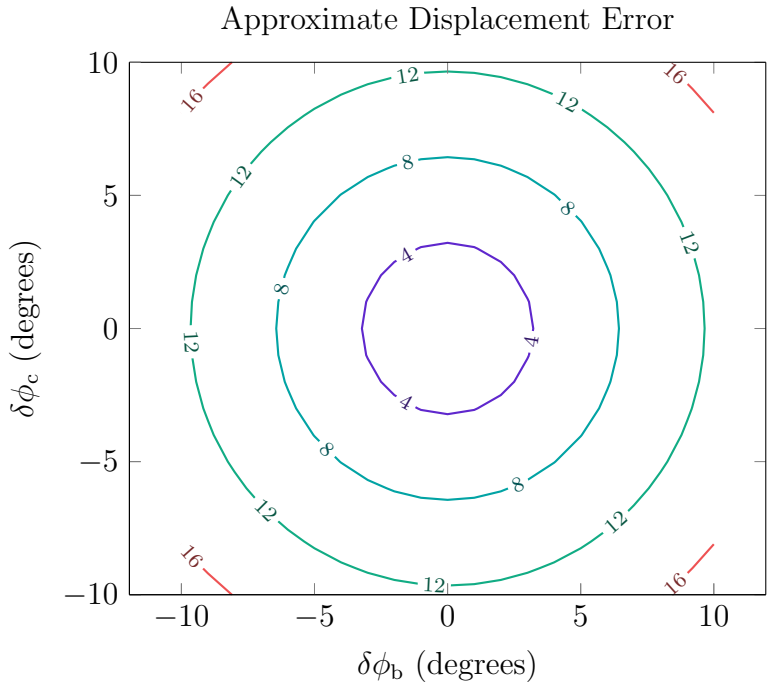

Figure 4.6: The theoretical displacement error at $\phi_\Lambda = 0\,\text{rad}$ when $\lambda = 1550\,\text{nm}$ and $\delta\lambda = 0.01\,\text{nm}$ in (a), and the approximate displacement error $\lambda = 1550\,\text{nm}$ in (b). The contours show the resulting displacement error in units of nanometres.

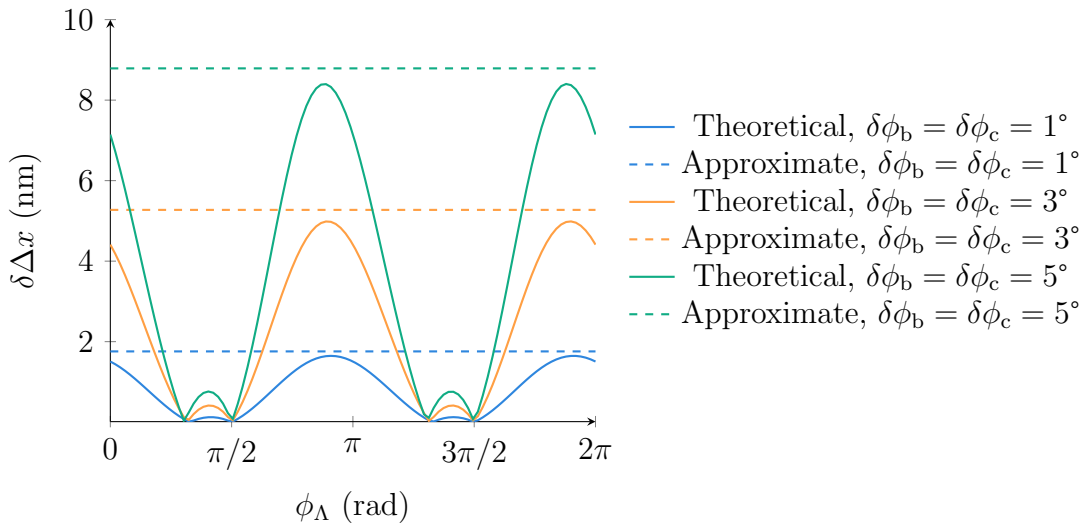

Figure 4.7: Comparison of theoretical and approximate displacement errors. The theoretical error curves demonstrate the dependence of the error on the OPD. The approximations show an overestimation of the worst case theoretical error.

linewidth of the laser to be 800 kHz, which at 1550 nm, corresponds to 0.000 006 nm in wavelength. In practice, the laser temperature can be controlled to a precision of 0.1 K with a temperature tuning coefficent of 0.1 nm/K, resulting in a continuous wave (CW) stability of 0.01 nm. With better temperature control the CW stability can be improved before hitting the limit of the laser linewidth, thereby $\delta\lambda = 0.01$ nm. The approximation from Equation 4.30 is plotted in Figure 4.6b using the same wavelength, $\lambda = 1550$ nm. Visually, the error approximation is more conservative than the theoretical error, but as its computation does not depend on the OPD, it provides a simple approximation of the worst case theoretical error.

To demonstrate the influence that OPD has on $\delta\Delta x$, Figure 4.7 shows a comparison of the theoretical error calculated by Equation 4.28 to the approximate error in Equation 4.30 with a select number of $\delta\phi_b$ and $\delta\phi_c$ values. From this plot, it is clear that the approximation is an overestimate, calculated to be 6 % greater than the maximum displacement error.

4.2 Initial Implementation

In this section, the design of the three-phase interferometer is presented. This discussion includes both the photonic and DSP design.

4.2.1 Interferometer

The interferometer is shown in Figure 4.9 and the contents of the photonics module are shown in Figure 4.10. From start to finish, the interferometer consists of many components, which are explained below.

Laser: The laser used is an Eblana Photonics DX1-DM single-mode 1550 nm distributed feedback (DFB) laser [69]. The DX1-DM was selected for its compact form factor and ability to operate from a standard 5 V power supply. During interferometer operation, the laser was kept stable at a known optical power and wavelength. The laser specification is found in Appendix A.

Optical Coupler: A custom 3×3 coupler from Oz Optics is used to split a single fibre-coupled signal across three output fibres. It is manufactured using a fused biconical taper, where three fibres are aligned parallel with their claddings together, heated, and then drawn from each end. This process creates a coupling region, in

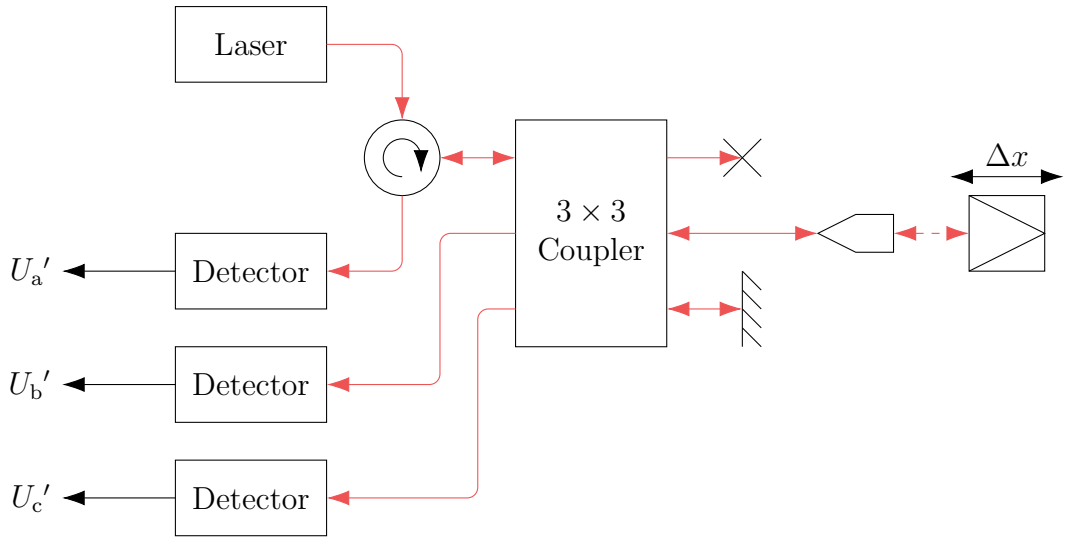

Figure 4.8: Schematic of the three-phase interferometer.

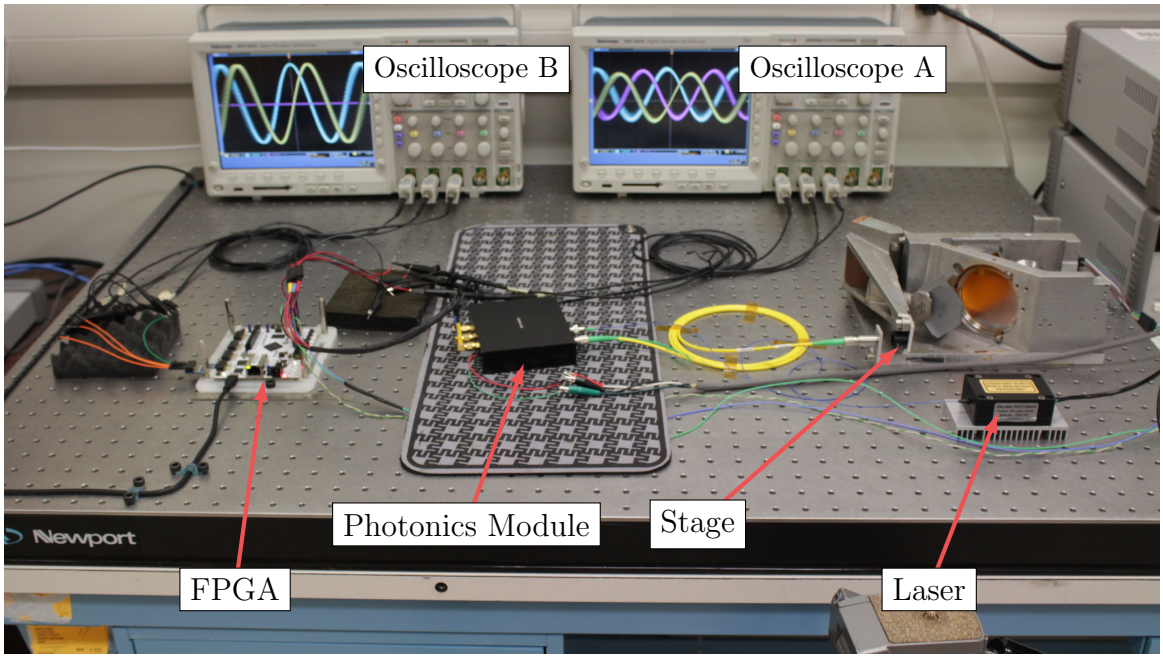

Figure 4.9: Three-phase interferometer bench top setup. The laser is guided into the photonics module, which houses the fibre circulator, 3×3 fibre coupler, and the photodetection circuit board. The probing beam is guided from the photonics module to a stage. The detected three-phase signals are carried to an FPGA by SMA cables. Oscilloscope A shows a waveform of the three-phase signals from the photonics module, and Oscilloscope B shows the quadrature signal produced by the FPGA-based signal processing procedure.

which evanescent waves can spread energy from fibre to fibre. Conservation of energy requires each output signal to undergo a phase shift. The better balanced the coupling regions are, the closer the phase shift is to $2\pi/3$ [48].

Collimator: To form the probing beam, a custom aspheric Kovar collimator from Oz Optics with a focal length of 18 mm was procured. Kovar was selected as it has a similar CTE to glass, which helps to maintain alignment as the instrument is cooled to $< 4\,\mathrm{K}$.

Corner Cube Prism Retroreflector: The retroreflector is a commercial-off-the-shelf Thorlabs PS974M-C prism fabricated from N-BK7 glass [70].

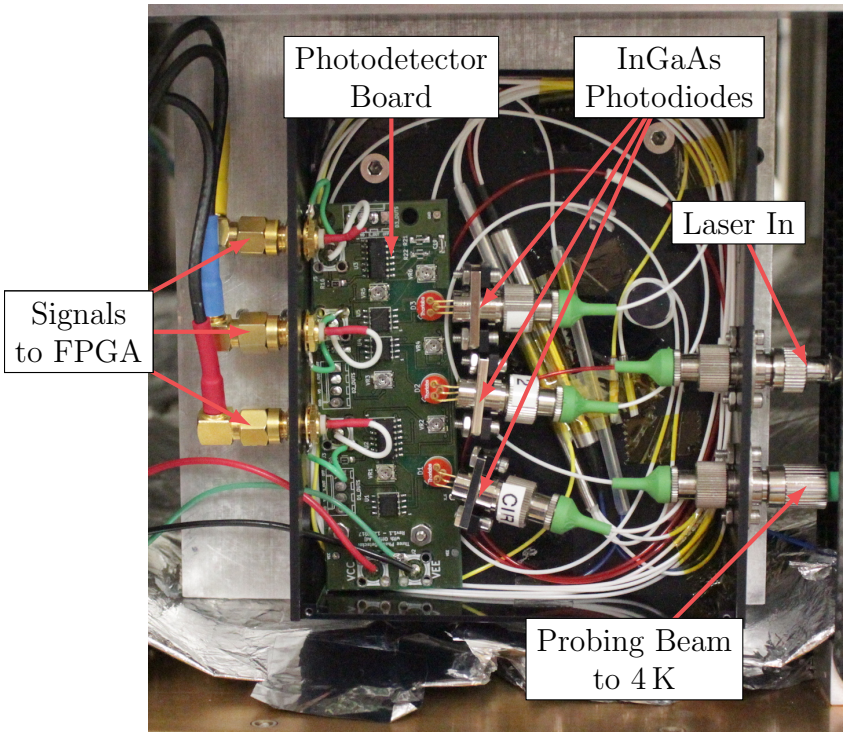

Figure 4.10: A three-phase photonics module containing a fibre circulator, 3×3 fibre coupler, and photodetection circuit board. On the right side, a laser enters through the top fibre, and the probing beam travels down the bottom fibre. On the left side the detected three-phase signals are carried to the signal processing FPGA by SMA cables.

4.2.2 Photodetection Circuit

The photodetection circuit shown in Figure 4.11 consists of three amplifiers. The circuitry is powered by a 5 V bipolar supply, where V_{CC} and V_{EE} denote the positive and negative rails, respectively. An image of the circuit board and the photonics is shown in Figure 4.10.

From left to right, the roles of the three amplifiers are described.

Offset Adjustment

The first op amp is set up as a voltage follower. An adjustable DC voltage is provided to the non-inverting input for offset adjustment.

Preamplification

The second op amp provides offset adjustment of the signal from a Thorlabs FGA01FC InGaAs photodiode [71]. It is important to note that since the amplifier is inverting, the resulting intermediate signal has a reversed polarity.

The photoconductive photodiode is reversed biased to increase the size of the diode depletion region, which in turn increases the detector responsivity. However, this also increases the noise floor, which reduces the overall signal-to-noise ratio (SNR) of the photodetection circuitry. This trade-off is necessary for high speed applications.

Postamplification

The third op amp provides gain adjustments via a variable resistor to equalize the effects of $U_{\mathrm{el,gn},x}U_{\mathrm{op,co,at},x}$ across all three signals. Together with the offset adjustment from the first amplifier, the signals are transformed into the appropriate 1 V range to be sampled by a Xilinx XADC [72]. To compensate for the second op amp inverting the signal, this amplifier is also inverting to retain the original signal polarity in the output signal, V_{pd}.

This amplifier also imposes restrictions due to its cut-off frequency, which is dependent on R_f and C_f:

$$f_{\mathrm{co}} = \frac{1}{2\pi R_f C_f}. \qquad [\mathrm{Hz}] \quad (4.31)$$

With $R_f = 4.7\,\mathrm{k\Omega}$ and $C_f = 1.5\,\mathrm{nF}$, the cut-off frequency is then $f_{\mathrm{co}} = 23\,\mathrm{kHz}$. This value is important since it sets the maximum allowable interferometer fringe rate, which limits the maximum translation velocity, v_{max}, to

$$v_{\mathrm{max}} = \frac{1}{2}\lambda f_{\mathrm{co}}. \qquad [\mathrm{m/s}] \quad (4.32)$$

In Equation 4.32, division by 2 is necessary to convert from optical to mechanical path. Solving Equation 4.32 using $f_{\mathrm{co}} = 23\,\mathrm{kHz}$ and the laser wavelength of 1550 nm

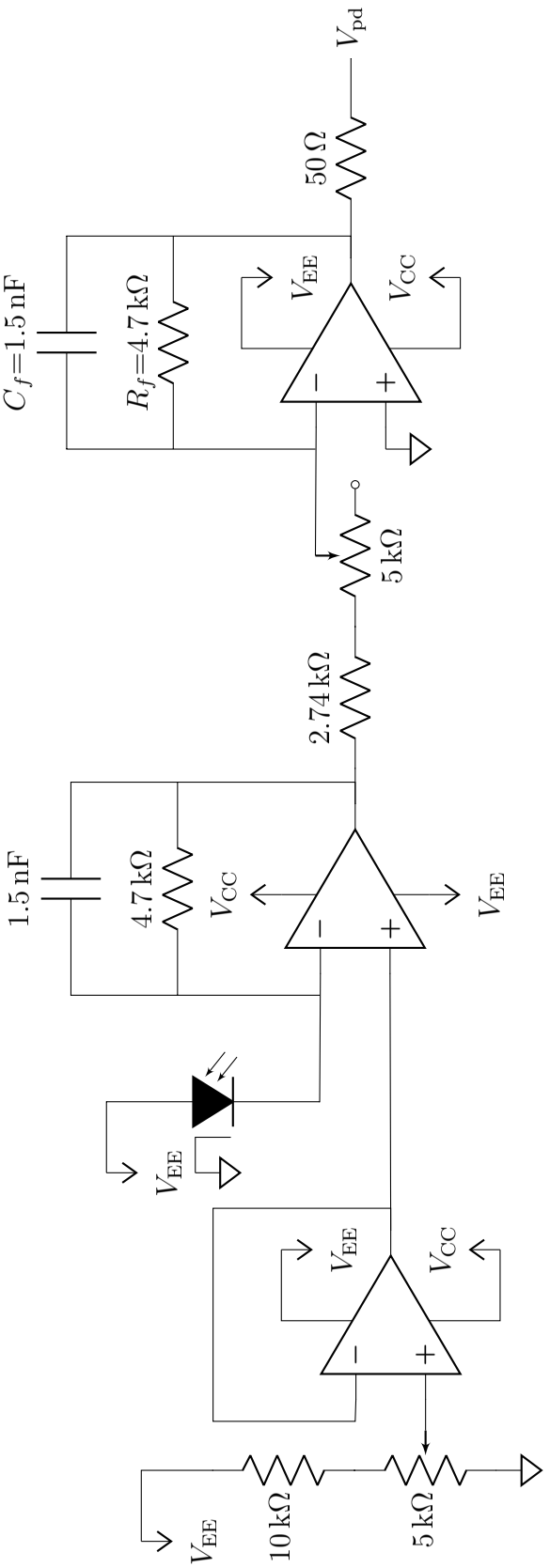

Figure 4.11: One of three photodetection circuits in the three-phase detection system.

yields a maximum translation velocity of 18 mm/s before the filter created by the third op amp begins to saturate.

As the rate of sensitive far-infrared cryogenic detectors is less than 10 Hz, the typical velocities in an FTS are less than 1 mm/s. The maximum measurable velocity for this three-phase interferometer implementation is an order of magnitude greater than the FTS requirements.

4.2.3 FPGA-based Signal Processing

To minimize processing latency, the three-phase signal processing is FPGA-based using a Xilinx XC7A35T Artix-7 Series FPGA [63] on a Digilent Arty A7-100T development board [62]. The design of the processing hardware is shown in Figure 4.12, which includes external connections to and from the FPGA.

The FPGA features an on-chip 12-bit, 1 MHz, 1 V range analog-to-digital converter (ADC) [72] which is used to sample three-phase signals generated by the photonics, U'_{a}, U'_{b}, and U'_{c}. Each three-phase signal is sampled using the same ADC, and its built-in channel sequencer is used to cycle through each. Effectively, the sampling rate is then 333 kHz on each channel. There is a phase shift of 1 µs between adjacent signals, and 2 µs between the first and third sampled channels. The maximum translation velocity dictated by the cut-off frequency, $f_{\mathrm{co}} = 23\,\mathrm{kHz}$, is $v_{\max} \approx 1.8\,\mathrm{cm/s}$. At this velocity, the 1 µs sampling delay corresponds to a phase delay of 25° between adjacent channels, at which point the signals can no longer be treated as proper three-phase signals. For translation velocities of $< 50\,\mu\mathrm{m/s}$ discussed in this thesis, the phase delay is 0.07° between adjacent channels which would contribute $< 0.2\,\mathrm{nm}$ displacement error.

Sampled three-phase signals are fed to the calibration procedure, which implements Equation 4.4 for each channel to determine coupling attenuation and electrical gains and offsets, $U_{\mathrm{el,gn},x}U_{\mathrm{op,co,at},x}$ and $U_{\mathrm{el,of},x}$. A full scan of the entire OPD is required to determine the global extrema for each signal. Gain correction uses the calibrated

parameters to correct each signal via Equation 4.5.

Gain corrected signals are then normalized using a procedure based on Equations 4.9, 4.10, 4.14, and 4.15. The normalization process is implemented as a streaming operation and no prior calibration is required. Normalized three-phase signals are converted into a quadrature signal via Equation 4.17, the Clarke Transformation.

A Digilent Pmod DA4 12-bit 8-channel digital-to-analog converter (DAC) is used to output analog three-phase and quadrature signals. A digital quadrature signal is also output simply by inverting the sign bit. These signals can be inspected or forwarded to another device, such as a motion controller.

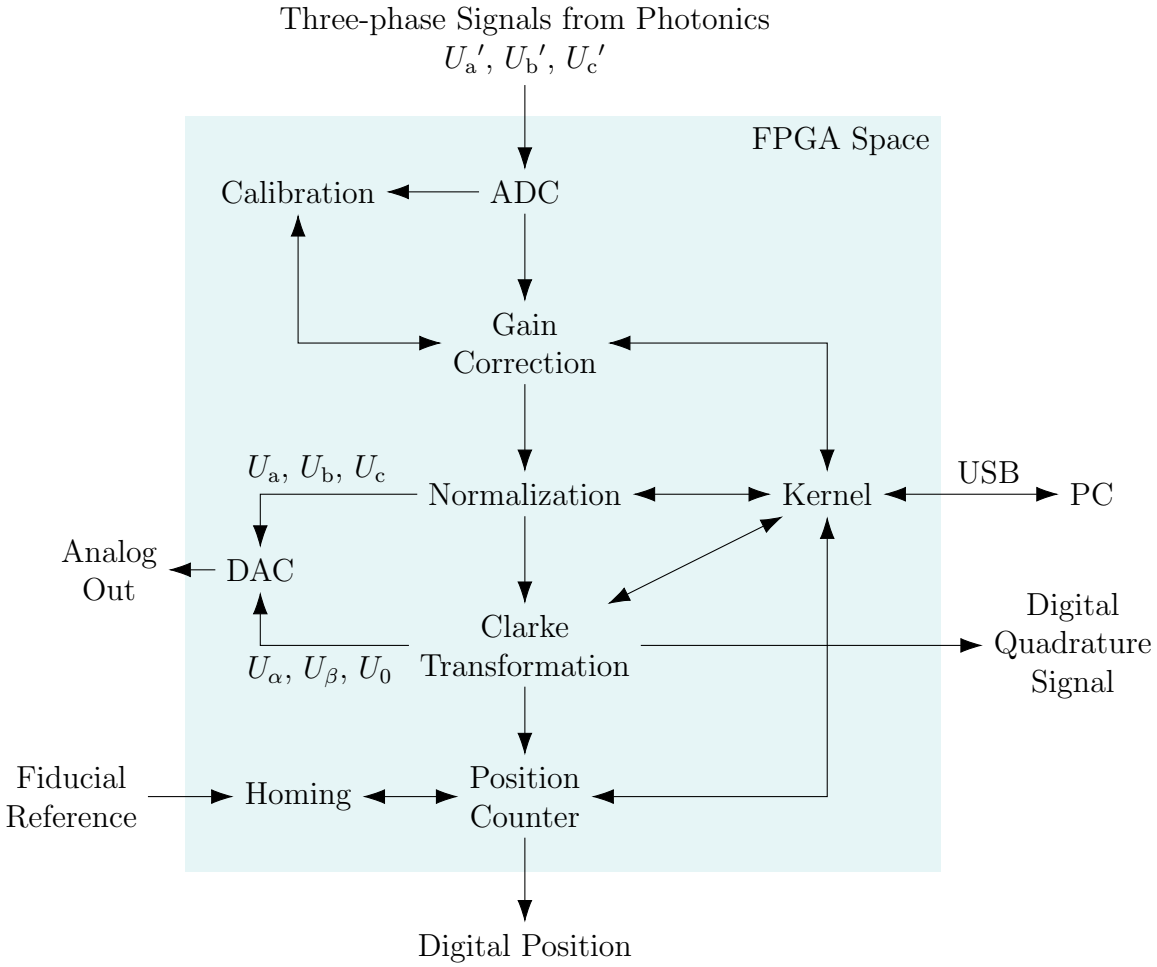

Figure 4.12: Data flow paths in the three-phase FPGA hardware design.

The quadrature signal is processed by the position counter, which tracks the change in quadrature encoded position relative to some starting point. Homing is performed based on an external cryogenic fiducial reference, such as an optical limit switch or Hall effect sensor, which tells the system the location of the zero position. The quadrature signal is converted into an angle using a coordinate rotation digital computer (CORDIC) arctangent [73]. Using Equation 3.45, phase unwrapping is performed on this angle to produce a position. This position is output on a 32-bit digital bus as radix-16 fixed-point number.

The kernel gives instructions to each subsystem, aggregates data, and communicates with a PC over Universal Serial Bus (USB) serial. Serial communication uses a datagram-based protocol with the FPGA acting as a slave that responds to requests, which are reads and writes to a register interface.

4.2.4 Performance at Room Temperature in the Laboratory

The three-phase interferometer was set up on the bench with a fixed OPD using a setup similar to the interferometer shown in Figure 4.9, but with the stage removed and replaced with a post at a fixed position to which the retroreflector was mounted. The entire interferometer was enclosed in a box to provide thermal isolation and minimize changes in refractive index due to air flow through the free space segment of the interferometer. Two thermometers were installed inside the enclosure to measure the ambient air temperature. Displacement and temperature data were collected for over a period of 64 h at a rate of 1 sample/ min and is shown in Figure 4.13.

Figure 4.13 demonstrates that the system initially measures a change in OPD proportional to the change in temperature. The OPD is comprised of both the free space segment and the fibre between the 3×3 coupler and the collimator. The CTE of the stainless steel bench in the free space segment is $\sim 10\,\mathrm{ppm/K}$ at room temperature [74], and larger than that of the optical fibre, which is assumed to be

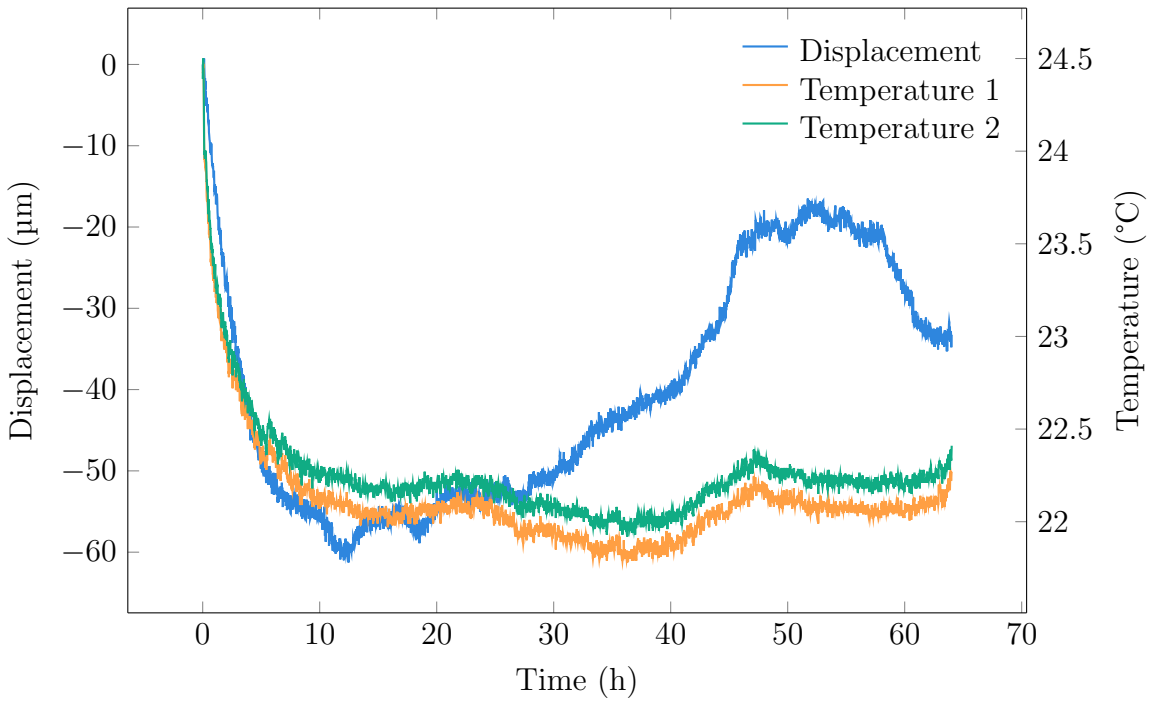

Figure 4.13: Three-phase displacement measurement of a fixed OPD over a period of $\sim 64\,\text{h}$. The interferometer was enclosed in a box and the ambient air temperature in the enclosure was measured with two thermometers. Displacement and temperature were sampled at 60 s intervals. The experiment was run over a weekend when no researchers were in the laboratory, and the 0 s mark corresponds to 17:00 on Friday. The initial contraction in the first $\sim 5\,\text{h}$ was due to a drop in temperature in the laboratory when the lights were turned off and the researchers left.

similar to silica at $< 1\,\text{ppm/K}$ [75]. However, the free space OPD segment will have an optical path length of $\leq 30\,\text{cm}$ in most applications, while the optical path length of the fibre-couple OPD segment is 1 m, as there is an extra metre of fibre between the coupler and the collimator than between the coupler and the fixed reference reflector. Even though the CTE of the fibre is relatively small, its thermal expansion will have a considerable effect on the displacement measurement as its optical path length is typically an order of magnitude larger than that of the free space segment.

At approximately the 30 h mark of Figure 4.13, the measured displacement no longer follows the temperature curves. The thermometers measured the ambient air temperature inside of the enclosure, not the temperature of the fibre or the surface

temperature stainless steel optical bench. One possible explanation for the discrepancy is that the thermometer readings do not accurately represent the temperature of the aluminum. Additionally, there are also performance issues at DC involving slowly varying OPDs. Negative performance impacts due to low fringe rates causing $1/f$ noise to become the dominant source will be discussed further in Subsection 4.3.3.

4.3 Differential Cryogenic Implementation

The initial three-phase interferometer design in Section 4.2 displayed poor performance, believed to be due to thermal expansion in the fibres and $1/f$ noise, as shown by the experiment in Subsection 4.2.4. To minimize the impact of fibre thermal expansion, a differential design was created using a custom armoured fibre.

4.3.1 Differential Interferometer

The differential design is similar to the initial three-phase design, sharing the same photonics, electronics, and signal processing procedure. The change from the initial to the differential design is that a second probing beam is introduced, and both beams are then carried by a custom armoured differential fibre, shown in Figure 4.15. The schematic of the differential interferometer is shown in Figure 4.14, illustrating that the fixed reflector is removed, and a second fibre guides a signal to $< 4\,\mathrm{K}$ by means of a differential fibre.

The custom armoured differential fibre consisting of two single mode fibres sharing a stainless steel tubing is shown in Figure 4.15. Since both fibres are now the same length, are physically close for their entire lengths, and are enclosed in a common armoured tubing, they will both experience the same thermal environment.

In order to leverage the enhanced resolution offered by the differential design, the retroreflectors must be mounted on opposite sides of the target, such that when the target travels at velocity, v, the folding factor of the interferometer causes the OPD

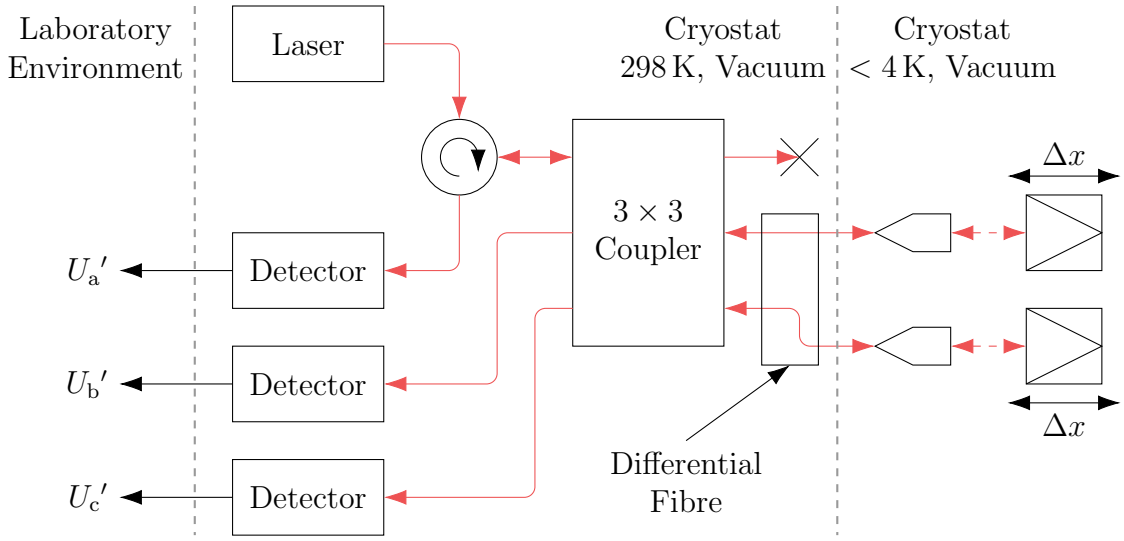

Figure 4.14: Schematic of the differential three-phase interferometer.

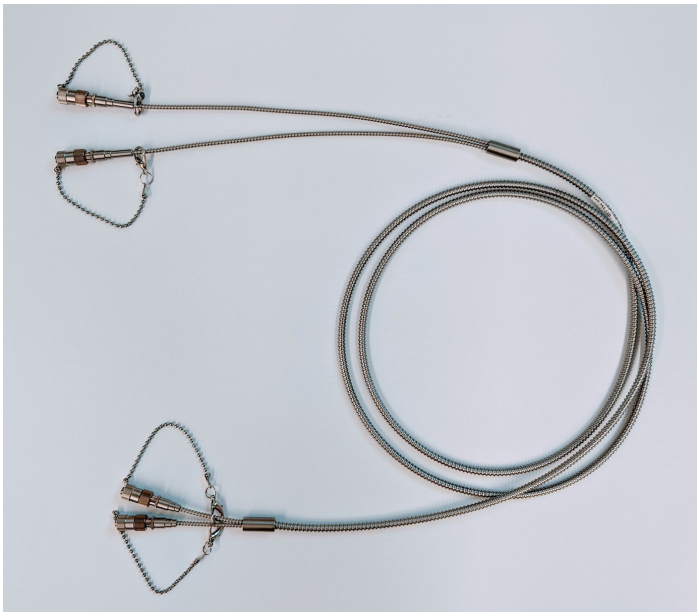

Figure 4.15: Custom differential armoured fibre. Two single mode fibres share a common stainless steel tubing with minimal divergence at each end. The overall length of the fibre is 2 m.

to change at a rate of $4v$. The resolution is improved due to the factor of 4 relating the mechanical path length to OPD. If it is not possible to mount both retroreflectors on the target, one of the retroflectors can be fixed elsewhere, making operation the same as the initial design with a factor of 2 relating mechanical path length to OPD,

but the interferometer retains the ability to reject common-mode thermal expansion.

4.3.2 Performance at 4 K in Vacuum

The differential three-phase interferometer was installed in a cryostat to measure the displacement of a rotary translation stage [76], as shown in Figure 4.16. Two retroreflectors were installed on opposite sides of the stage, allowing the interferometer to run in fully differential mode. The stage was driven with a sinusoidal displacement profile with a small amplitude at $< 4\,\mathrm{K}$, allowing the stage motion to be approximated as linear. A relatively linear section of travel was captured by reading a digital position value from the FPGA at 10 kHz using a Teensy++ 2.0 microcontroller [77] connected via digital headers on each board. A quadratic fit was applied to the data to produce a residual, and the mechanical displacement, fit, and residual are shown in Figure 4.17.

Buffering limitations in the sampling method allowed for only short duration acquisitions. Averaging the uncertainty over the whole acquisition is equivalent to reporting it in a 55 Hz bandwidth. The accuracy of the system was determined from the

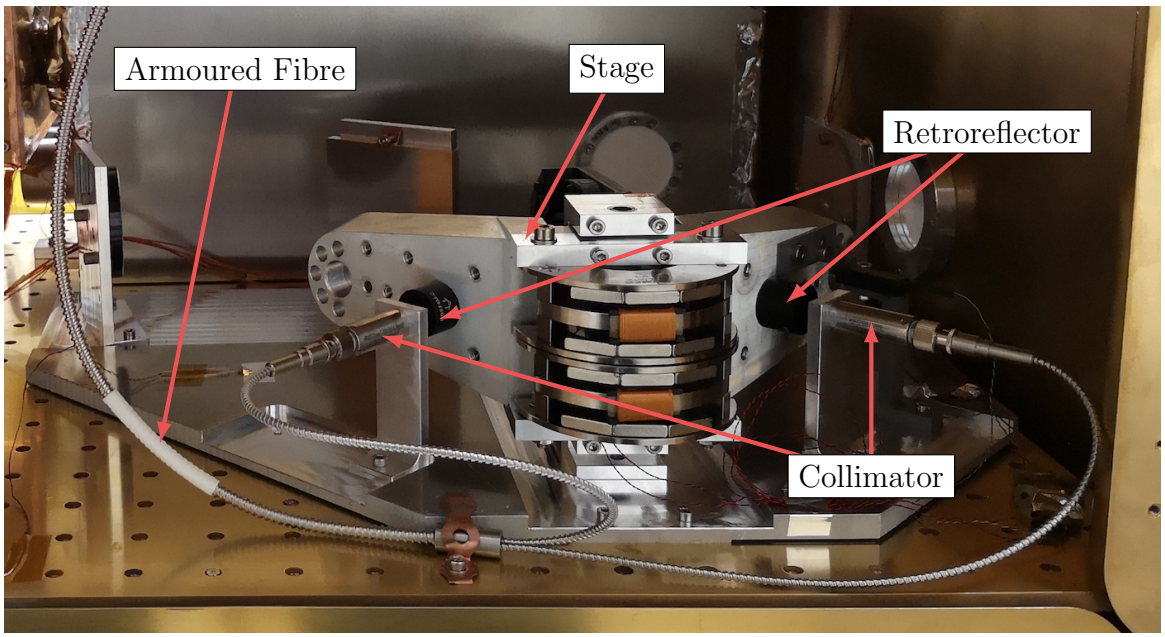

Figure 4.16: Differential three-phase interferometer installed in the 4 K volume of a cryostat to measure the displacement a rotary translation stage.

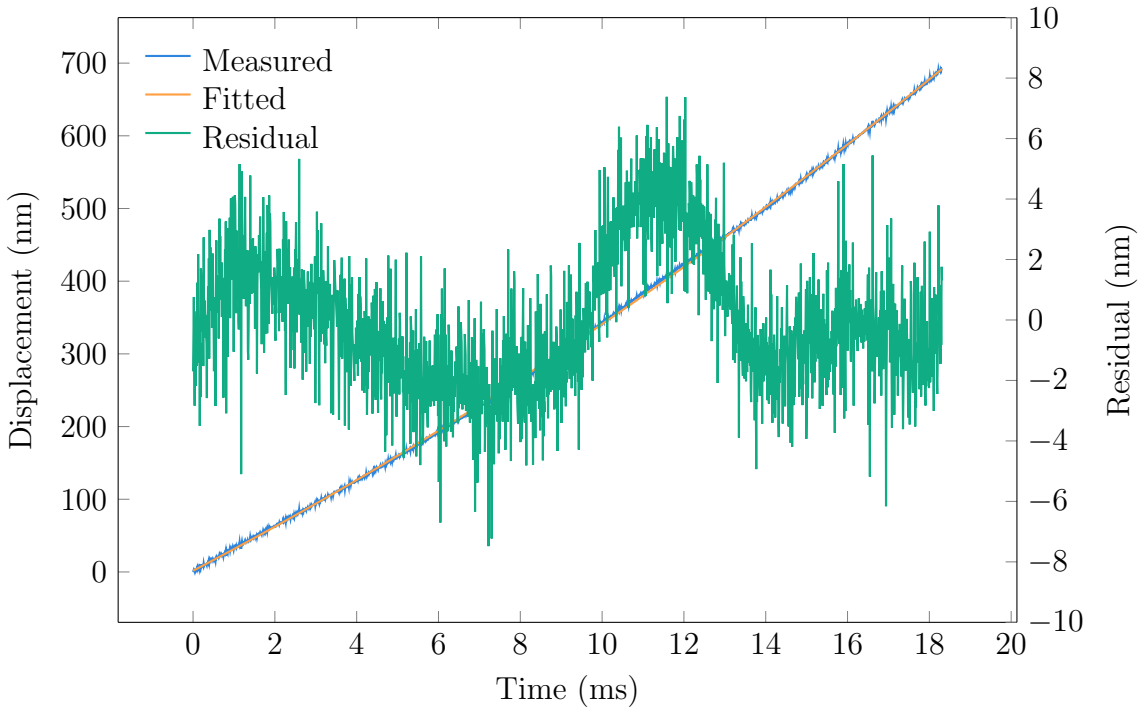

Figure 4.17: Differential three-phase cryogenic displacement accuracy measurement. The measured displacement of a translation stage at $< 4\,\mathrm{K}$ sampled at 10 kHz.

residual in Figure 4.17, which is 2.3 nm rms in mechanical path in a 55 Hz bandwidth. This error corresponds to $\sim 3^\circ$ error in the three-phase signals, based on the error approximation from Equation 4.30. Note that the right side of Equation 4.30 must be divided by 2 to account for the increase in the factor of 2 to 4 relating mechanical and optical paths in the differential design. Displacement is reported by the FPGA as a fixed-point value with an 8-bit fraction. With a 1550 nm laser and a factor of 4 relating mechanical to optical path, the least significant bit of the fraction represents $\sim 1.5\,\mathrm{nm}$ and does not limit the accuracy. The mechanical velocity is $\sim 39\,\mu\mathrm{m/s}$ and corresponds to a frequency of $\sim 100\,\mathrm{Hz}$ at each photodetector, which is sufficiently rapid for minimal $1/f$ contributions to the noise floor, showing that the noise in the measurement is the base noise level of the electronics.

4.3.3 Cryogenic Aluminum CTE Experiment

The DC performance of the differential three-phase interferometer was tested by measuring the CTE of aluminum 6061 as it was cycled from $\sim 300\,\mathrm{K}$ to $< 4\,\mathrm{K}$. The aluminum sample is shown in Figure 4.18, where it is installed in a differential testing mount on the 4 K plate of a cryostat. The testing mount was machined out of aluminum so that its contraction is similar to that of the sample. During testing the cryostat is inverted so that the sample is suspended to reduce vibration.

The overall length of the aluminum sample is $\sim 121\,\mathrm{mm}$, however, due to the differential nature of the measurement, only the contraction between the retroreflectors is measured. At $\sim 300\,\mathrm{K}$, the length between the retroreflectors was measured to be 105.9 mm.

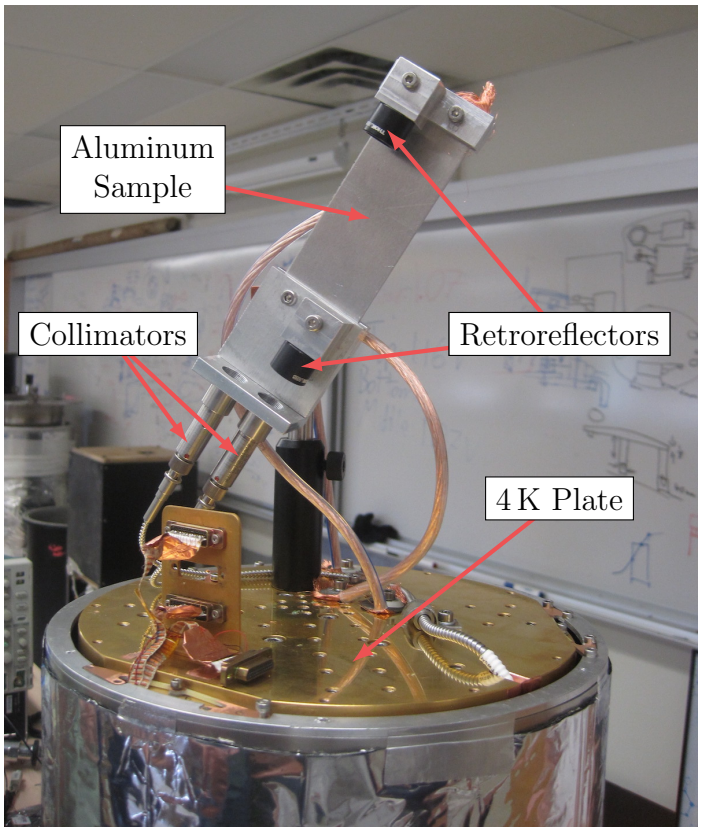

Figure 4.18: An aluminum sample in a differential cryogenic CTE testing mount. The mount is installed to the 4 K plate of a cryostat.

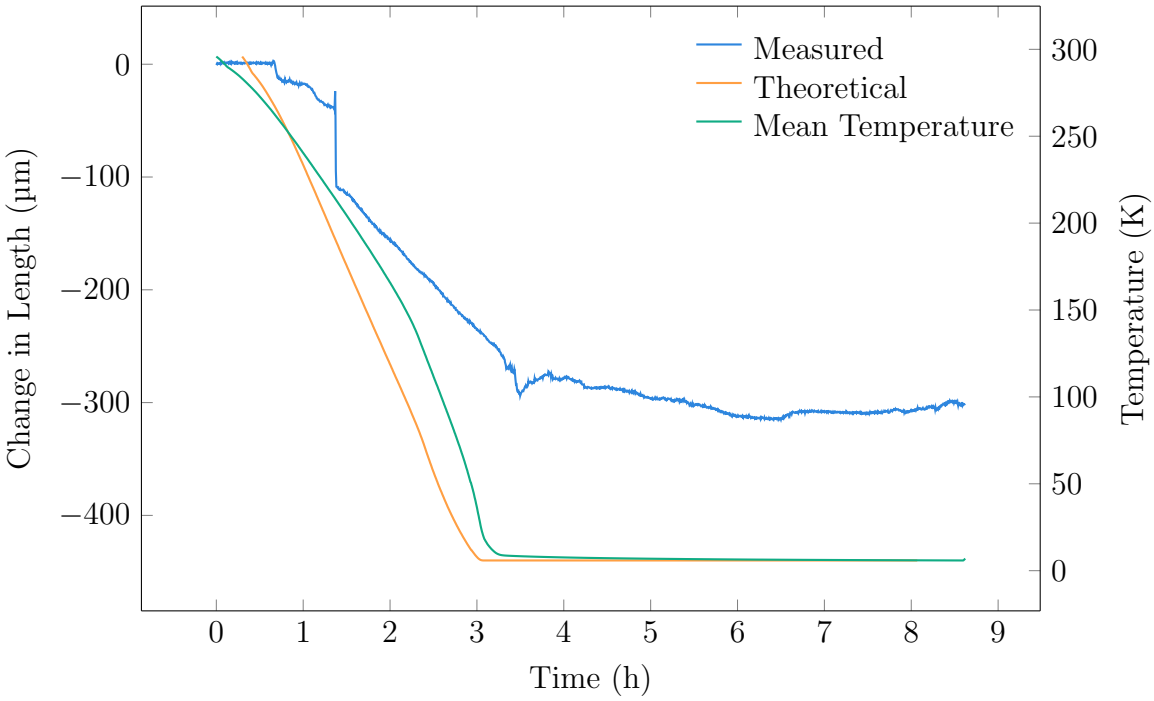

Figure 4.19: Cryogenic aluminum 6061 CTE measurements using the differential three-phase interferometer. The mean temperature of the sample is used to generate a theoretical contraction curve.

As the sample was cycled, the contraction was measured by sampling the displacement measurement from the three-phase FPGA at 27 Hz over USB serial. Four thermometers attached to the aluminum sample provided temperature measurements, which were averaged to obtain the mean temperature of the sample. The maximum standard deviation of the mean at any point was 1.5 K. A theoretical contraction curve was calculated using the aluminum 6061 CTE from the National Institute of Standards and Technology database [78] along with the mean temperature. The measured and theoretical contraction, as well as the mean sample temperature, are plotted in Figure 4.19. Although the measured contraction follows the theoretical shape, drifting is present, which is most noticeable after the 3 h mark where there should be no contraction as the temperature is constant. A rapid drift occurs near the 1.5 h mark, where a contraction of $\sim 75\,\mu m$ is measured over a period of ~ 60 s. The average contraction velocity in this interval is 1.25 µm/s, which is over 26 times greater than the

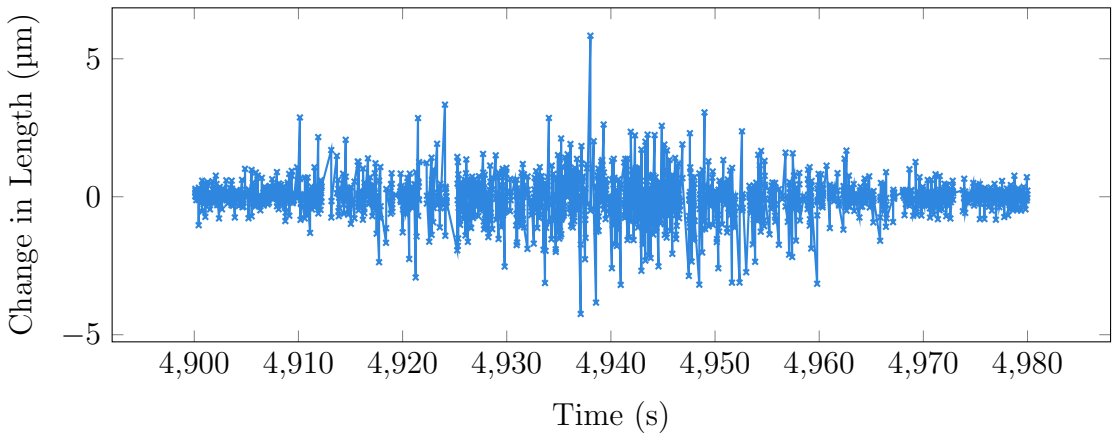

Figure 4.20: Point-to-point jumps in a select region of the differential aluminum CTE measurement shown in Figure 4.19.

0.046 µm/s average contraction velocity of the theoretical curve during the cooldown section.

The values of the point-to-point jumps in the region of extreme velocity near the 1.5 h mark are shown in Figure 4.20. The largest change in position in a sampling interval that the system can handle is $\lambda/2$ in OPD, which due to the factor of 2 relating mechanical displacement to OPD is 0.39 µm mechanical; however, the greatest observed point-to-point jump is 5.8 µm mechanical. An initial investigation into the possibility of phase unwrapping errors did not uncover a source for the extremely large jumps and does not explain why these jumps are only observed for low velocity measurements. Internally, the FPGA updates the displacement counter at 333 kHz, which is down sampled to 27 Hz when the displacement is read. During the interval between samples transmitted over USB serial, $1/f$ noise in the photodetection electronics causes "false" fringes, which are interpreted as a change in OPD by the FPGA, and lead to a drift in displacement.

4.4 Conclusions

In this chapter, the technique of three-phase laser interferometry has been presented, including experiments at room and cryogenic temperatures. The initial interferometer design employed a single probing beam and a fixed reference reflector. Room temperature testing showed that the design was prone to fibre thermal contraction, which causes a change in OPD and is falsely measured as a change in mechanical displacement.

The removal of the fixed reference reflector allowed for fully differential measurement by replacing it with a second probing beam. A custom armoured differential fibre transmitted the probing beams from room to cryogenic temperatures, which was capable of rejecting the effects of common-mode thermal expansion in the fibres. The displacement of a cryogenic translation stage was measured, and the accuracy of the interferometer was determined to be 2.3 nm rms at < 4 K. Subsequent cryogenic experiments to measure the CTE of aluminum demonstrated the poor DC performance of the system when the OPD was slowly varying or static.

Having gained experience in fibre-fed laser metrology concepts and given the poor observed performance of low velocity measurements, I decided to change direction to simplify the photonics and move the frequency outside of the low frequency band to avoid $1/f$ noise by adopting a frequency modulation approach.

Chapter 5

Frequency Modulation Cryogenic Interferometer

Results from three-phase interferometry experiments, presented in Chapter 4, demonstrated that $1/f$ noise in the photodetector circuitry is a limiting issue for practical use of the system. One way to minimize $1/f$ noise is to modulate the laser, which shifts the power spectral density of the signal away from 0 Hz. I have adopted and extended Kissinger's work in frequency modulation range-resolved interferometer [50] to applications at cryogenic temperatures.

5.1 Introduction

In this section, the foundations of frequency modulation range-resolved interferometry will be introduced based on the work of Kissinger [50]. Although Kissinger describes the technique for the simultaneous measurement of multiple OPDs, the theory presented in this section is restricted to single axis measurement involving only one OPD. Kissinger describes fibre segment interferometry, where the entire interferometer is fibre-based. I extend this design for free space operation in a cryogenic environment, using the interferometer design in Figure 5.1.

5.1.1 Modulation

A DFB laser is modulated about a centre optical frequency, ν_c, with an optical frequency modulation amplitude, ν_A, measured as the maximum departure from ν_c,

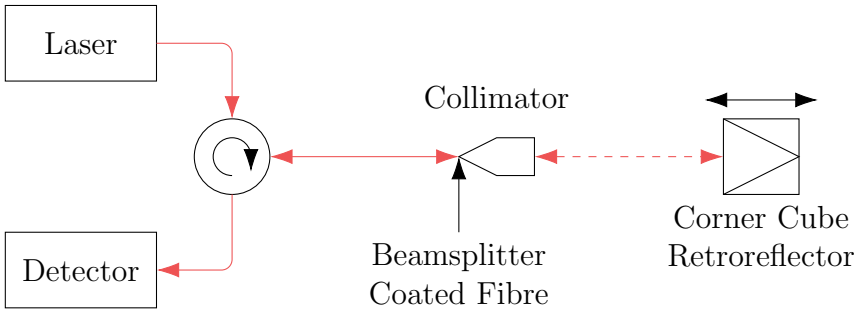

Figure 5.1: Schematic of the frequency modulation interferometer. A free space beam probes the displacement of a moving retroreflector.

at a modulation frequency of f_{m}, to produce a time dependent laser frequency

$$\nu\left(t\right) = \nu_{\mathrm{c}} + \nu_{\mathrm{A}} \sin 2\pi f_{\mathrm{m}} t. \qquad [\mathrm{Hz}] \quad (5.1)$$

In this interferometer, two separate frequencies, ν_1 and ν_2, arise due to the time of flight difference between the first and second interferometer arms. Assuming the first arm acts as a reference, a delay, $\tau_{\mathrm{f}}(t)$, must be considered for the beam in the second arm, which represents the time taken for the light to travel the OPD. The result is that ν_2 is a delayed copy of ν_1, according to

$$\nu_1\left(t\right) = \nu_{\mathrm{c}} + \nu_{\mathrm{A}} \sin 2\pi f_{\mathrm{m}} t, \qquad [\mathrm{Hz}] \quad (5.2a)$$

$$\nu_2\left(t\right) = \nu_{\mathrm{c}} + \nu_{\mathrm{A}} \sin\left(2\pi f_{\mathrm{m}}\left(t - \tau_{\mathrm{f}}(t)\right)\right). \qquad [\mathrm{Hz}] \quad (5.2b)$$

Since displacement is encoded as phase, it is more convenient to work with phase rather than frequency. Physically, the phase of some signal, ϕ, is 2π multiplied by the time integral of the frequency. Integrating the frequencies from Equation 5.2 leads to

the respective phases:

$$\phi_1(t) = 2\pi\nu_c t - \frac{\nu_A}{f_m}\cos 2\pi f_m t + \phi_0, \qquad \text{[rad]} \quad (5.3a)$$

$$\phi_2(t) = 2\pi\nu_c\left(t - \tau_f(t)\right) - \frac{\nu_A}{f_m}\cos\left(2\pi f_m\left(t - \tau_f(t)\right)\right) + \phi_0, \qquad \text{[rad]} \quad (5.3b)$$

where ϕ_0 is a constant of integration. Physically, ϕ_0 is the initial phase, and is common to both ϕ_1 and ϕ_2.

Recall the interference equation from Equation 3.34, which relates both signal intensity and phase. For this analysis, we are interested in the phase difference, $\Delta\phi = \phi_1 - \phi_2$, which from Equation 5.3 is

$$\Delta\phi = \frac{\nu_A}{f_m}\left[\cos\left(2\pi f_m\left(t - \tau_f(t)\right)\right) - \cos 2\pi f_m t\right] + 2\pi\nu_c\tau_f(t). \qquad \text{[rad]} \quad (5.4)$$

The trigonometric product-to-sum identity, $2\sin\alpha\sin\beta = \cos(\alpha-\beta) - \cos(\alpha+\beta)$, can be applied, but first each sinusoid in Equation 5.4 must be shifted by $+\pi f_m\tau_f$. Since both phases are shifted, $\Delta\phi$ is not affected. By phase shifting and applying the product-to-sum identity to Equation 5.4, we arrive at

$$\Delta\phi = \underbrace{\underbrace{\frac{2\nu_A}{f_m}\sin\left(\pi f_m\tau_f(t)\right)}_{\theta_A}\sin\left(2\pi f_m t\right)}_{\theta_m} + \underbrace{2\pi\nu_c\tau_f(t)}_{\phi_\Lambda}. \qquad \text{[rad]} \quad (5.5)$$

The phase difference is best described in two parts. First is the phase modulation function, which serves as a carrier wave. This is described by

$$\theta_m = \theta_A \sin 2\pi f_m t, \qquad \text{[rad]} \quad (5.6)$$

where θ_A is the phase modulation amplitude. The time of flight delay is related to

the interferometer OPD by $\tau_{\mathrm{f}}(t) = n\Lambda/c$, thus θ_{A} can be expressed as

$$\theta_{\mathrm{A}} = \frac{2\nu_{\mathrm{A}}}{f_{\mathrm{m}}} \sin \frac{\pi n f_{\mathrm{m}} \Lambda}{c}. \qquad \text{[rad]} \quad (5.7)$$

Since τ_{f} cannot be known exactly, as it is dependent on Λ. Instead, the approximation $\tau_{\mathrm{f}} \approx n\Lambda_0/c$, is used, where Λ_0 is the centre optical path difference. The interferometer in Figure 5.1 will have a minimum OPD, Λ_{min}, and maximum OPD, Λ_{max}, dictated by constraints on the range of motion of the corner cube. Λ_0 is defined as the midway point between the minimum and maximum OPDs, taking a value of $\Lambda_0 = (\Lambda_{\mathrm{min}} + \Lambda_{\mathrm{max}})/2$. Equation 5.7 can then be reformulated as the approximation,

$$\theta_{\mathrm{A}} \approx \frac{2\pi n \nu_{\mathrm{A}} \Lambda_0}{c} \quad \text{for} \quad \Lambda_0 \ll \frac{c}{\pi n f_{\mathrm{m}}}. \qquad \text{[rad]} \quad (5.8)$$

The validity of Equation 5.8 can be assessed using practical values for the modulated laser configuration. Consider a commercial infrared diode laser having a centre frequency of $\nu_{\mathrm{c}} = 193\,\mathrm{THz}$ ($\lambda = 1550\,\mathrm{nm}$) which is modulated at $f_{\mathrm{m}} = 10\,\mathrm{kHz}$ in vacuum. For these parameters, it should hold that $\Lambda_0 \ll 10\,\mathrm{km}$, which makes Equation 5.8 a reasonable approximation for experiments discussed in this thesis where $\Lambda_0 < 1\,\mathrm{m}$.

The second part of the phase difference in Equation 5.5 is the OPD dependent phase, ϕ_Λ. This phase encodes information about the displacement of the moving mirror in the interferometer. The phase difference from Equation 5.5 can then be expressed as

$$\Delta\phi = \theta_{\mathrm{m}} + \phi_\Lambda, \qquad \text{[rad]} \quad (5.9)$$

which highlights the fundamental principle of this technique. Of the two terms which contribute to the phase difference, we control one, θ_{m}, and the other is dependent on the interferometer OPD. By selecting an appropriate demodulation scheme, θ_{m} can

be eliminated, leaving ϕ_Λ, from which the displacement can be derived.

5.1.2 Photodetector Normalization

As with any photonic circuit, not all photons that enter will reach the output. Fringe visibility is reduced by a suboptimal beamsplitter transmittance to reflectance ratio, and losses in optical components attenuate the entire signal. A full analysis of these effects is complicated and unnecessary, as practical operation of the interferometer requires that the fringe visibility is maximized and the effective efficiency of the interferometer is known. When tuning the beamsplitter reflectance and transmittance to maximize fringe visibility, one must consider that the beamsplitter and the retroreflector form a low finesse Fabry-Pérot cavity, for which an analysis is presented in Appendix B along with a technique to experimentally determine the optimal beamsplitter reflectance and transmittance. All losses are consolidated into a single effective interferometer efficiency, η_{eff}, which is an approximation that is experimentally determined by modulating the laser and measuring the average output power as a fraction of the average input power while the OPD is is kept constant. Consequently, when a signal generated by a laser with a power envelope of P_{laser} enters the interferometer, η_{eff} relates it to the output power envelope seen at a photodetector, P_{pd}, by

$$P_{\text{pd}} = \eta_{\text{eff}} P_{\text{laser}}. \qquad \text{[W]} \quad (5.10)$$

A laser cannot be frequency modulated without introducing some degree of power modulation. Therefore, just as $\nu(t)$ is a function of time, the laser power envelope, $P_{\text{laser}}(t)$ is as well. Using a laser characterization procedure, such as the one discussed in Appendix C, a curve relating laser power to frequency can be obtained. It is not only time dependent, but also depends on the interferometer time of flight delay, τ_{f}, and the signal processing delay, τ_{sig}. The signal processing delay includes delays such as digital-to-analog conversions and analog-to-digital conversions. A curve relating

laser power to frequency can be obtained, and the expression for the theoretical laser power is then more accurately $P_{\text{laser}}(t-\tau_{\text{f}}-\tau_{\text{sig}})$. More conveniently, this is $P_{\text{laser}}(t-\tau_{\text{d}})$ where τ_{d} is

$$\tau_{\text{d}} = \tau_{\text{f}} + \tau_{\text{sig}}. \qquad [\text{s}] \quad (5.11)$$

Thus, a normalized frequency modulation signal, U_{fm}, can be obtained by

$$U_{\text{fm}} = \frac{2P_{\text{pd}}\,(t)}{\eta_{\text{eff}} P_{\text{laser}}(t-\tau_{\text{d}})} - 1, \quad (5.12)$$

which in practice will produce the normalized signal

$$U_{\text{fm}} = \cos\left(\theta_{\text{m}}\,(t-\tau_{\text{d}}) + \phi_{\Lambda}\right). \quad (5.13)$$

5.1.3 Demodulation

In order to demodulate U_{fm}, a complex carrier signal, $\mathcal{C}$, is generated, using a phase demodulation amplitude, θ_{D}. For correct demodulation, θ_{D} must be selected such that $\theta_{\text{D}} = \theta_{\text{A}}$, using either Equation 5.7 or the approximation Equation 5.8, producing the carrier:

$$\mathcal{C}\,(t, \theta_{\text{D}}, \tau_{\text{d}}) = \exp\big(j\theta_{\text{D}} \sin\left(2\pi f_{\text{m}}\,(t-\tau_{\text{d}})\right)\big). \quad (5.14)$$

Demodulation using $\mathcal{C}$ includes baseband components in the demodulated signal. To avoid unwanted baseband contributions, a windowing function, W_G, consisting of infinitely many tiled Gaussian kernels and shown in Figure 5.2c, is used. The kernels described by a width parameter, σ, are placed such that they are located where the frequency of U_{fm} is most rapidly changing, which are points centred on the zero crossings of ν in Equation 5.1, or equivalently, the zero crossings of θ_{m}, which can be seen in Figure 5.2a. Using the modulation period, $T_{\text{m}} = 1/f_{\text{m}}$, the window

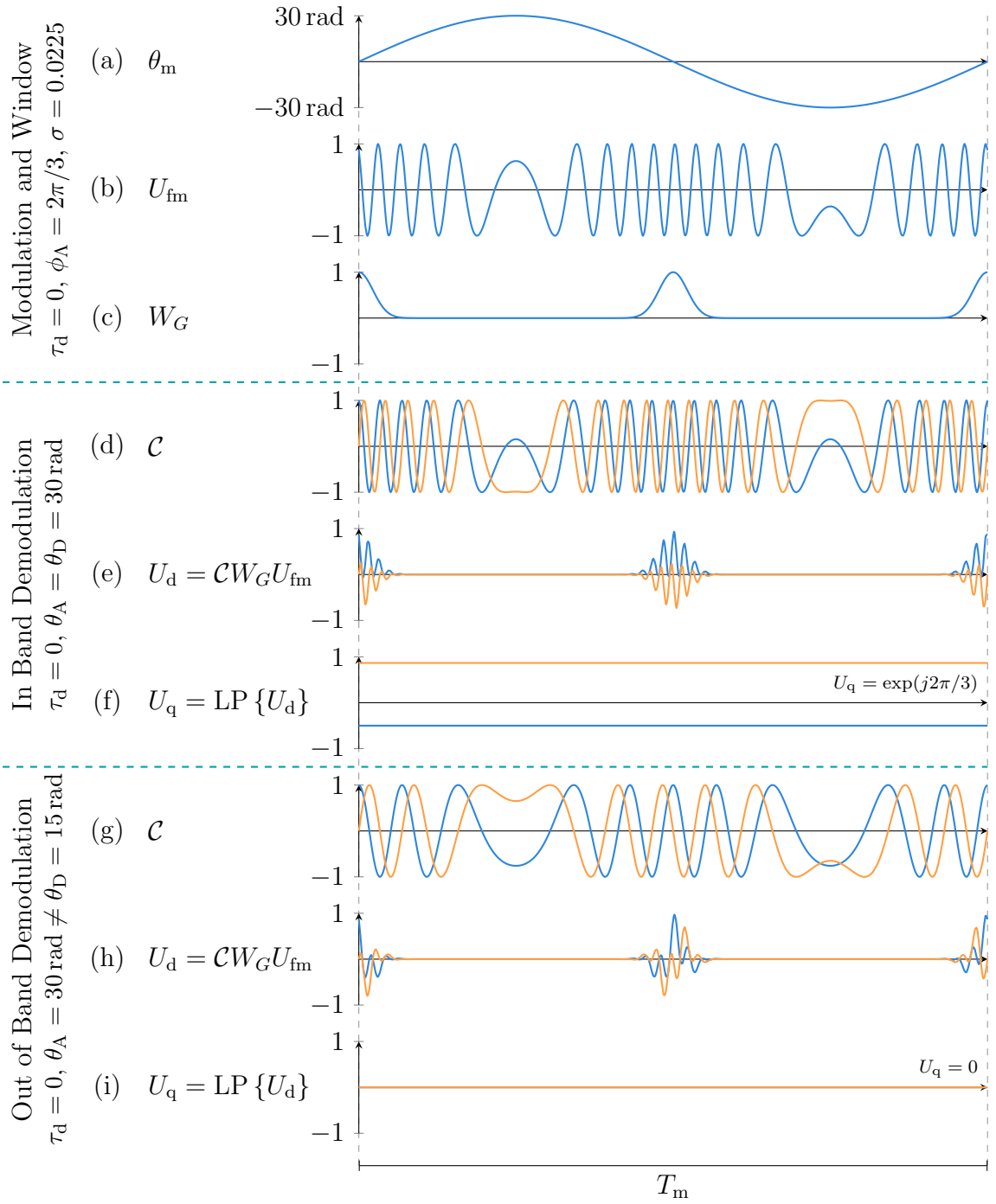

Figure 5.2: Simulated modulation and demodulation for both in and out of band signals for $\phi_\Lambda = 2\pi/3$. Real and imaginary parts of the signal are orange and blue, respectively. For simplicity, $\tau_d = 0$. In (a), phase modulation by $\theta_A = 30$ rad is shown which produces the normalized signal in (b). The window function in (c) is used for demodulation. In band demodulation where $\theta_A = \theta_D$ is shown in (d), (e), (f), while out of band demodulation where $\theta_A \neq \theta_D$ is shown in (g), (h), (i). ϕ_Λ is recovered as a complex quadrature signal for in band demodulation in (f). No quadrature signal is recoverable for out of band demodulation.

function is defined as

$$W_G\left(t,\sigma,\tau_\mathrm{d}\right)=\sum_{m=-\infty}^{\infty}\exp\left(-\frac{1}{2}\left(\frac{\left(t-\tau_\mathrm{d}\right)-mT_\mathrm{m}/2}{\sigma T_\mathrm{m}}\right)^2\right). \tag{5.15}$$

From Equations 5.12, 5.14, and 5.15, the complex demodulated signal, U_d, can be obtained by

$$U_\mathrm{d}=\mathcal{C}W_G U_\mathrm{fm}, \tag{5.16}$$

however, the demodulated signal does not give usable phase information in this form. A low-pass filter, LP, is used to recover a complex quadrature signal, U_q, from the complex demodulated signal, via

$$U_\mathrm{q}=\mathrm{LP}\left\{U_\mathrm{d}\right\}. \tag{5.17}$$

The demodulation process is graphically shown in Figure 5.2. The example phase modulation uses $\theta_\mathrm{A}=30\,\mathrm{rad}$. Quadrature encoding of the OPD dependent phase is recovered and shown in Figure 5.2f. The quadrature signal appears to be constant over a single modulation period because the selected low-pass filter in the example is a mean of the entire U_d signal. Regardless of the selected low-pass filter, the quadrature signal will always be slow moving within a single modulation period as it is the baseband component of the signal, which refers to signals $\leq f_\mathrm{m}$.

In cases for out of band demodulation, the phase amplitudes of the signal, U_fm, and the carrier, $\mathcal{C}$, differ, resulting in different frequencies for each signal. When demodulated, the result is a signal with a mean that tends to zero as the frequency difference increases. For this reason, any attempt to recover a quadrature signal via a lowpass filter will produce an output signal that tends to zero.

Assuming in band demodulation, the phase, ϕ_q, encoded by the quadrature signal,

U_q, is equal to the OPD dependent phase, ϕ_Λ. The displacement is then,

$$\Delta x = \frac{1}{2}\lambda_c \frac{\phi_q}{2\pi} = \frac{1}{4\pi}\lambda_c \phi_q, \qquad [\text{m}] \quad (5.18)$$

where $\lambda_c = c/\nu_c$ is the centre wavelength. The leading coefficient of 1/2 in Equation 5.18 is to compensate for the factor of 2 relating mechanical displacement to optical path length.

5.2 Cryogenic Implementation

In this section design and implementation of a frequency modulation interferometer in a cryogenic environment is presented. This discussion covers both the photonic and DSP design.

5.2.1 Interferometer

A fibre-based laser interferometer was constructed according to the schematic in Figure 5.3. The laser and detector are under vacuum at room temperature, while the beamsplitter, collimator, and moving mirror that form the interferometer are placed under vacuum at $< 4\,\text{K}$.

Inside the cryostat, a Thorlabs P5-SMF28ER-50-1 fibre patch cord with a 50:50

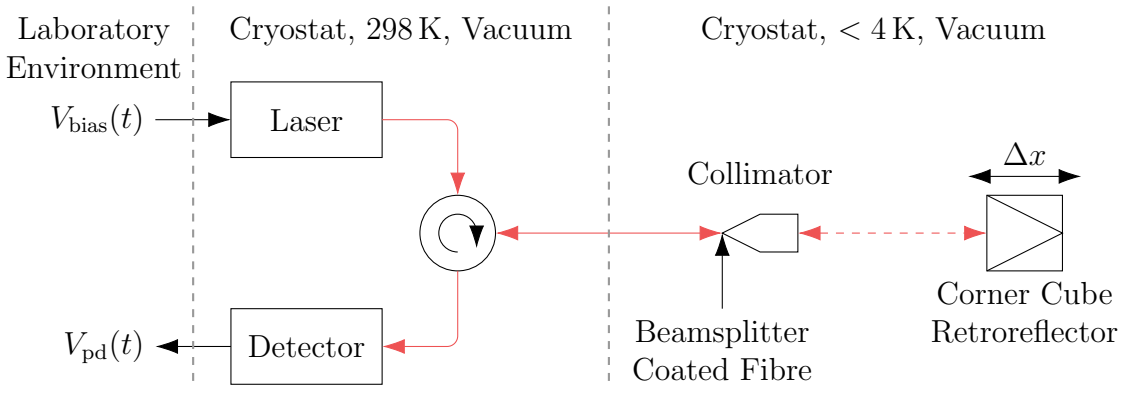

Figure 5.3: Schematic of the frequency modulation interferometer in a cryogenic environment.

beamsplitter coated FC/PC terminal [79] is mated to a custom aspheric Kovar collimator, $f = 18\,\text{mm}$, from Oz Optics. The collimator was designed to match the CTE of the lens to minimize stresses due to thermal cycling. The collimated beam probes a Thorlabs PS974M-C prism retroreflector [70] mounted to a translation stage. The selected collimator and retroreflector are the same models as the those used for the construction of the three-phase interferometer described in Section 4.2.

A 50:50 beamsplitter coating was selected because it is the most readily available commercial-off-the-shelf beamsplitter coated fibre. In principle, a better ratio can be selected to optimize fringe visibility, as discussed in Appendix B, however, only 50:50 coatings are commonly commercially available, and others require expensive custom manufacturing.

5.2.2 Laser Modulation

A modulation of the laser bias current results in both the laser power and wavelength to be modulated. The exact modulation is unique to each diode, as no two diodes are manufactured identically, and any laser used in the system must be individually characterized.

An Eblana DX1-DM DFB laser module [69] without bias input stabilization was selected, allowing it to be modulated at frequencies up to 80 kHz (see Appendix A for laser specifications). The diode bias current is modulated using a bias voltage input to the module, V_{bias}. Both the power and wavelength modulation were characterized as described in Appendix C, yielding the following empirical relations

$$P_{\text{laser}}\left(V_{\text{bias}}\right) = -2.47V_{\text{bias}}^2 + 15.66V_{\text{bias}} - 2.15, \qquad [\text{mW}] \quad (5.19a)$$

$$\lambda\left(V_{\text{bias}}\right) = -0.02V_{\text{bias}}^3 + 1.19V_{\text{bias}}^2 + 0.43V_{\text{bias}} + 1548.69. \qquad [\text{nm}] \quad (5.19b)$$

The frequency modulation amplitude, ν_{A}, can be determined from Equation 5.19b.

If V_{bias} is modulated between two voltages, V_1 and V_2, where $V_1 < V_2$, the wavelength of the laser will be modulated between wavelengths, λ_1 and λ_2, respectively. The laser frequencies corresponding to λ_1 and λ_2 are ν_1 and ν_2, allowing ν_{A} from Equation 5.1 to be expressed as

$$\nu_{\text{A}} = \frac{\nu_1 - \nu_2}{2} = \frac{c}{2}\left(\frac{1}{\lambda_1} - \frac{1}{\lambda_2}\right). \qquad \text{[Hz]} \quad (5.20)$$

5.2.3 Photodetection Circuit

The photodetector circuitry utilizes a single high slew rate op amp to amplify the signal from a high-speed Thorlabs FGA01FC InGaAs photodiode [71], as shown in Figure 5.4. The circuit is powered by a 5 V power supply, where V_{CC} is the positive supply rail. With $R_f = 1\,\text{k}\Omega$ and $C_f = 10\,\text{pF}$ the amplifier cut-off frequency is $f_{\text{co}} = 16\,\text{MHz}$. Unlike the three-phase interferometer, the cut-off frequency does not directly restrict the maximum translation velocity, but rather limits the maximum fringe rate, which is a function of OPD, laser modulation frequency, and velocity. In this particular implementation, the maximum fringe rate is governed by the sampling frequency of 1 MHz, as it is significantly less than the cut-off frequency.

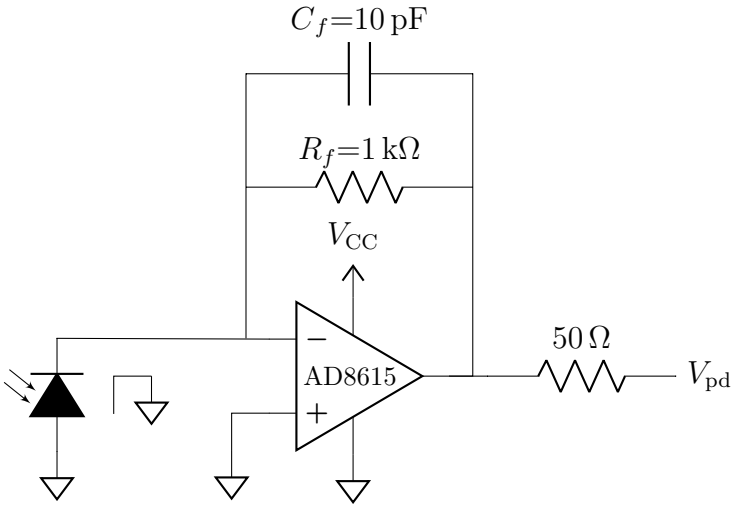

Figure 5.4: Schematic of the frequency modulation photodetection circuitry featuring an AD8615 op amp [80].

A transfer function for converting voltage from the photodetection circuitry, V_{pd}, to the optical power received by the photodetector, P_{pd}, was determined by a calibration procedure, outlined in Appendix D. The resulting function is

$$P_{\mathrm{pd}}\left(V_{\mathrm{pd}}\right) = 8.83V_{\mathrm{pd}} + 0.09, \qquad [\mathrm{W}] \quad (5.21)$$

which is used in Equation 5.12 to obtain a normalized signal, U_{fm}.

5.2.4 Low-Pass Filter

A brief introduction to digital filters is presented in Appendix E, and outlines an argument for preference of a finite impulse response (FIR) filter over an infinite impulse response (IIR) filter. An FPGA-based cascaded integrator-comb [81] configured as a low-pass filter was used, which is a simple hardware-efficient FIR filter. This filter is a discrete-time moving average described by

$$y\left[n\right] = \frac{1}{N}\sum_{m=0}^{N-1} x\left[n-m\right], \quad (5.22)$$

where x is the input signal, N is the number of points included in the average, y is the filter output, and n is an index. The filter schematic in Figure 5.5 illustrates why it is hardware efficient. A delay and a single three-way sum are the only operations involved, allowing an arbitrary N to be selected with the only modification to the filter being the number of delay stages.

The magnitude of the filter frequency response, $|H(j\omega)|$, (for which the full derivation is presented in Appendix E) is given by

$$\left|H\left(j\omega\right)\right| = \frac{1}{N}\left|\frac{\sin\left(\omega N/2\right)}{\sin\left(\omega/2\right)}\right|, \quad (5.23)$$

where ω is the normalized angular frequency. For a signal with a frequency f sam-

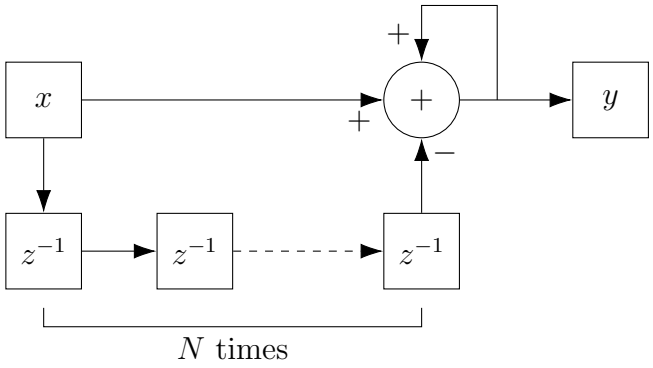

Figure 5.5: A schematic of a cascaded integrator-comb low-pass filter with an averaging width of N. The notation z^{-1} is a convention in signal processing to denote a delay by 1 sample. Scaling of the output by $1/N$ is omitted.

pled at a rate f_s, the normalized angular frequency is $\omega = 2\pi f/f_\mathrm{s}$. Using this ω, Equation 5.23 is plotted for a select set of N values in Figure 5.6.

Using $|H(j\omega)|$, there are many ways to select an appropriate N. For example, N can be selected for -3 dB cut-off, -6 dB cut-off, first side lobe null, second side lobe null, and so on. A value for N which satisfies both -3 dB cut-off with $f_\mathrm{co} \leq f_\mathrm{m}/2$ and first side lobe null conditions will be determined. The inclusion of the first side lobe null condition is so that periodic artifacts of the carrier present in the demodulated signal are removed.

The solution for N at the side lobe nulls, $|H(j\omega)| = 0$, requires that

$$\frac{\omega N}{2} = m\pi, \quad m = 1, 2, 3, \ldots \text{ and } N \nmid m, \tag{5.24}$$

where $N \nmid m$ means that N is not a divisor of m, or in other words, that m is not a multiple of N. This restriction is due to the lack of nulls when ω is a multiple of 2π, which is illustrated by Figure 5.6.

Since we are working at the modulation frequency, f_m, the normalized angular

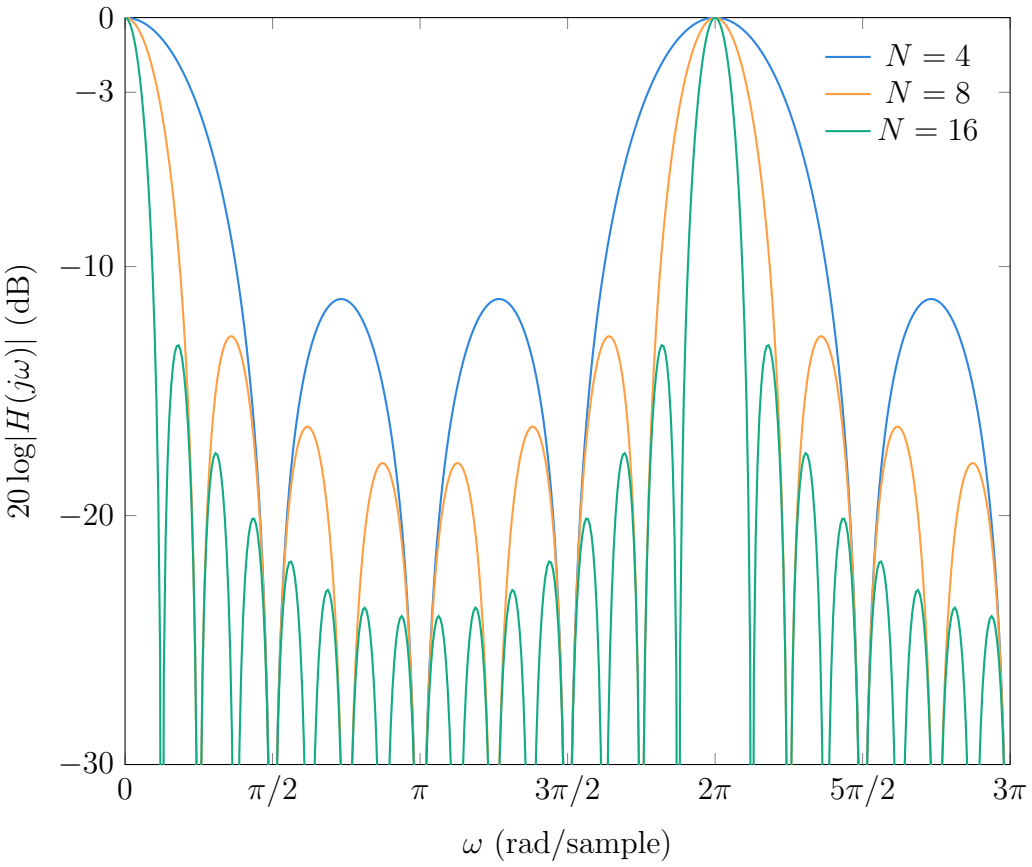

Figure 5.6: The magnitude of the filter frequency response for a select set of N values according to Equation 5.26.

frequency is $\omega = 2\pi f_\mathrm{m}/f_\mathrm{s}$. Solving Equation 5.24 using this ω leads to

$$N = m\frac{f_\mathrm{s}}{f_\mathrm{m}}, \quad m = 1, 2, 3, \ldots \text{ and } N \nmid m. \tag{5.25}$$

It should be noted that $f_\mathrm{s}/f_\mathrm{m}$ is the number of samples in a single modulation period. At the first side lobe null, $m = 1$, which gives an averaging width of

$$N = \frac{f_\mathrm{s}}{f_\mathrm{m}}. \tag{5.26}$$

When the $-3\,\mathrm{dB}$ cut-off is $f_\mathrm{co} = f_\mathrm{m}/2$, the averaging width is $N \approx 0.6 f_\mathrm{s}/f_\mathrm{m}$. This was found by simulation similar to the magnitude of the frequency response in

Figure 5.6, where N was varied until the $-3\,\mathrm{dB}$ point occurred at $f_\mathrm{m}/2$, corresponding to $\omega = 2\pi f_\mathrm{co}/f_\mathrm{s}$. Kissinger reports that the cut-off frequency should be selected such that $f_\mathrm{co} \leq f_\mathrm{m}/2$ [50], which guarantees Nyquist sampling of the quadrature signal. Selecting N according to Equation 5.26, which is equal to the number of samples in one modulation period, exhibits a cut-off frequency of $f_\mathrm{co} \approx 0.44 f_\mathrm{m} \leq f_\mathrm{m}/2$. This was found again through simulation, this time setting $N = f_\mathrm{s}/f_\mathrm{m}$ according to Equation 5.26, and determining the frequency at the $-3\,\mathrm{dB}$ point.

Since the cut-off frequency of the filter is that maximum frequency of the quadrature signal, the maximum translation velocity, v_max, that can be measured is

$$v_\mathrm{max} = \frac{1}{2}\lambda_\mathrm{c} f_\mathrm{co}. \qquad [\mathrm{m/s}] \quad (5.27)$$

5.2.5 MPSoC-based Signal Processing

The signal processing system is implemented using a Digilent Cora Z7-10 development board [64] which features a Xilinx XC7Z010 Zynq-7000 MPSoC [65]. The design of the processing hardware is shown in Figure 5.7, which includes external connections to and from the MPSoC. All signal values in the FPGA are represented by 32-bit signed fixed-points with the radix after the 16^th bit. The role of each subsystem of the design in Figure 5.7 is explained as follows:

Event Loop: The processor runs a custom bare-metal program which responds to events and dispatches jobs as needed, acting as an extremely lightweight real-time operating system (RTOS). As there are no hard real-time deadlines for jobs executed by the processor, scheduling does not require any of the sophisticated logic typically found in an RTOS, such as FreeRTOS [82] or µC/OS [83]. Each job is a very short lived process which has only one responsibility, such as updating a configuration value, communicating with the FPGA, or polling for events. The simplicity of this design allows the system to maintain a FIFO queue of jobs which are executed using a first-

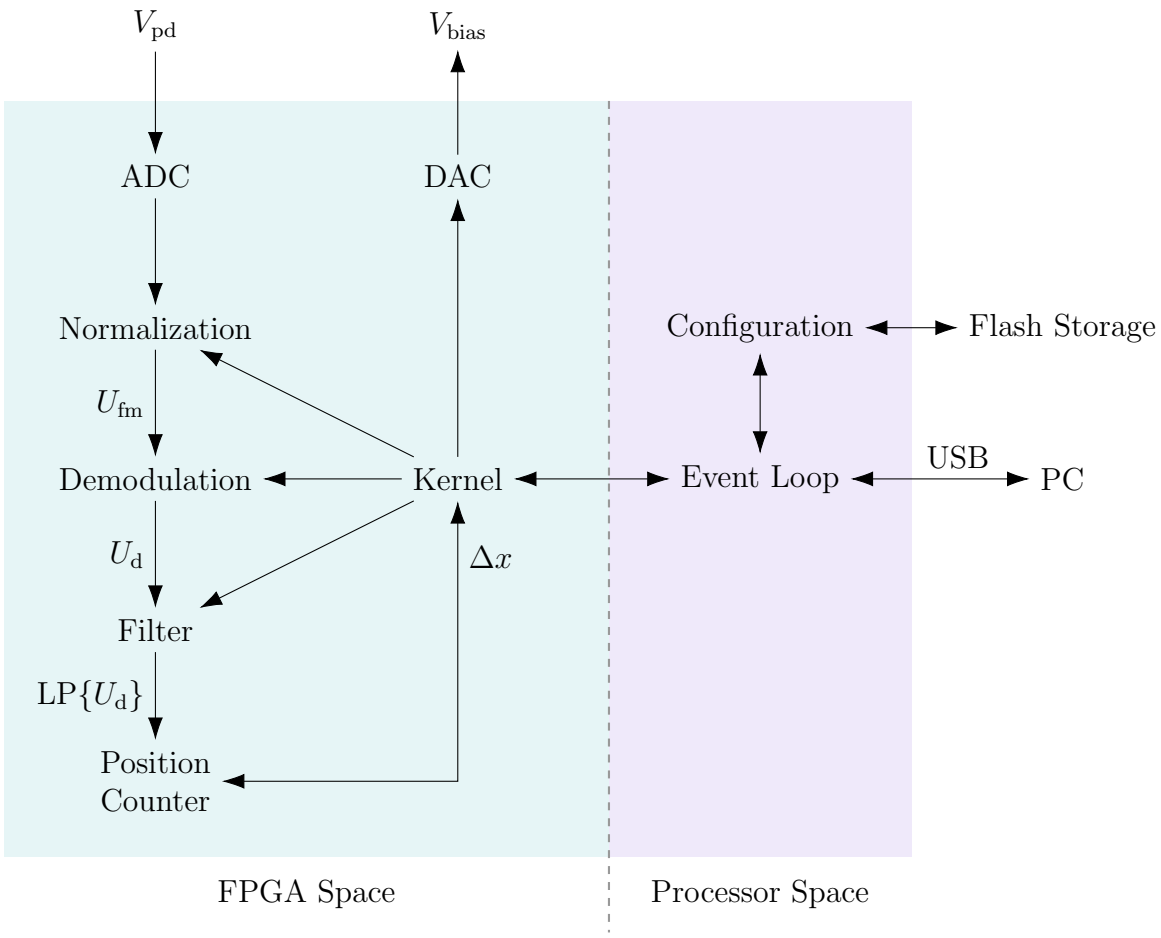

Figure 5.7: Data flow paths in the frequency modulation MPSoC design.

come first-serve scheduling algorithm [84]. The event loop facilitates communication with a PC through a job which parses commands received over USB serial and then builds new jobs to respond appropriately.

Configuration and Flash Storage: The configuration stores parameters used to modulate the laser and demodulate the signal. Modulation and demodulation waveforms are generated from these parameters and then transferred to the FPGA. Since these values are hardware specific, they are not hard-coded into the system, and are instead received over USB serial. Parameters used to generate modulation and demodulation can also be stored in, and loaded from, an external flash storage device, allowing standalone operation.

Kernel: The first responsibility of the kernel is to facilitate communication between the FPGA and processor to allow the transfer of data and control signals. Control signals are decoded by the kernel and dispatched to the appropriate subsystem. The second responsibility of the kernel is to provide each subsystem of the FPGA with data for processing. When modulation, normalization, and demodulation waveforms generated by the processor are transferred to the kernel, they are stored in individual buffers. Due to the volume of data in the buffers and concurrent access requirements, the buffers are based in a pool of multiplexed BRAMs, with each buffer at an assigned base address and addressable in 32-bit word sizes by the processor. However, BRAMs in Zynq-7000 MPSoCs only have two read/write ports [65], which is insufficient for our needs. The adopted solution is to construct a memory out of multiple BRAMs that presents itself to the processor as a single contiguous address space. The kernel stores data across multiple BRAMs, allowing for multiple simultaneous readers and writers in the address space while preserving a simple interface for the processor. The pre-generated $\mathcal{C}W_G$ waveforms are then streamed sample-by-sample from each buffer to the appropriate subsystems. Since only a single modulation period of each waveform is stored, buffers are treated as a cycle, and when the stream index reaches the end of the buffer it restarts from the base address.

DAC: The DAC is a Digilent Pmod DA3 16-bit, 1 MHz with a 2.5 V FSR [85]. A pre-generated sinusoidal waveform is used to modulate V_{bias} to the laser.

ADC: The Xilinx Zynq-7000 features an on-chip 12-bit, 1 MHz, 1 V FSR ADC [72] which is used to sample the photodetector voltage, V_{pd}, at the full 1 MHz rate. Although greater bit depths and higher speed sampling are preferred, attempts to implement a 16-bit 10 MHz ADC as part of the photodetection circuit board failed, and the slower built-in ADC was used as backup. Future versions will be implemented using a Digilent Eclypse Z7 development board which has commercially available 14-bit 100 MHz ADC and DAC expansion cards [86].

Normalization: Because the ADC simply digitizes V_{pd}, the output of the ADC subsystem is a digital approximation of a voltage in the interval $[0, 1]$ with an offset and an amplitude envelope. Normalization is implemented by Equation 5.12, where P_{laser} is computed from V_{bias} using Equation 5.19a and P_{pd} is computed from V_{pd} using Equation 5.21. The resulting U_{fm} signal, given by Equation 5.12, is visibility and power normalized to the interval $[-1, 1]$.

Demodulation: Using Equation 5.16, U_{fm} is demodulated by multiplication with the carrier, $\mathcal{C}$, and window, W_G, functions to produce U_{d}. By storing the product $\mathcal{C}W_G$, storage requirements are reduced by a factor of 2.

Filter: The low-pass filter is implemented using Equation 5.22. The synthesized design is true to the schematic shown in Figure 5.5. A delay of N is implemented by a variable-depth BRAM-based shift register, with the depth, N, tied to the number of samples in one modulation period, as determined by Equation 5.26. The filter transforms the input, U_{d}, into a complex quadrature signal, U_{q}.

Position Counter: A CORDIC arctangent [73] is applied to U_{q} to determine its phase, ϕ_{q}. The phase is converted into a displacement by Equation 5.18.

5.3 Proof of Concept Experiments

To test the frequency modulation technique, a Digilent Arty A7-100T FPGA was used was used to modulate an Eblana DX1-DM laser module [69] using a Digilent Pmod DA3 DAC [85]. The FPGA sampled the voltage from a photodetection circuit using its internal ADC, and the sampled and modulation data were transmitted to a PC over Ethernet to be processed offline by a signal processing procedure implemented in Python [87] using the NumPy library [88]. Additionally, the FPGA utilizes a second ADC channel to sample an analog output from a stage controller when available, which provides a signal proportional to the stage position.

5.3.1 Performance at Room Temperature in the Laboratory

The interferometer shown in Figure 5.11 was set up on an optical breadboard at room temperature. A Thorlabs PS974M-C [70] corner cube retroreflector is mounted to a PI P-628.1CD PIHera piezo linear precision positioner [89], which forms the moving arm of the interferometer. The photodetection circuitry and free space launching setup with piezo stage are shown up close in Figure 5.8. The FPGA and its electrical connections are shown in Figure 5.9.

The interferometer was initially configured to have a centre OPD of $\Lambda_0 = 26\,\mathrm{cm}$. Sinusoidal laser bias voltage modulation between 380 mV to 420 mV resulted in a laser frequency modulation amplitude $\nu_\mathrm{A} = 3.429\,\mathrm{GHz}$ about a centre optical frequency $\nu_\mathrm{c} = 193.537\,777\,\mathrm{THz}$ at a rate of $f_\mathrm{m} = 1\,\mathrm{kHz}$. The interferometer efficiency was not measured, since the offline processing program automatically power normalizes based on the expected laser output power.

The stage was driven with a sinusoidal motion profile, and the position monitor of the stage controller, which outputs an analog voltage proportional to the stage position, was sampled. Both the recovered displacement and the displacement reported by the stage controller are shown in Figure 5.10. The analog position monitor from the

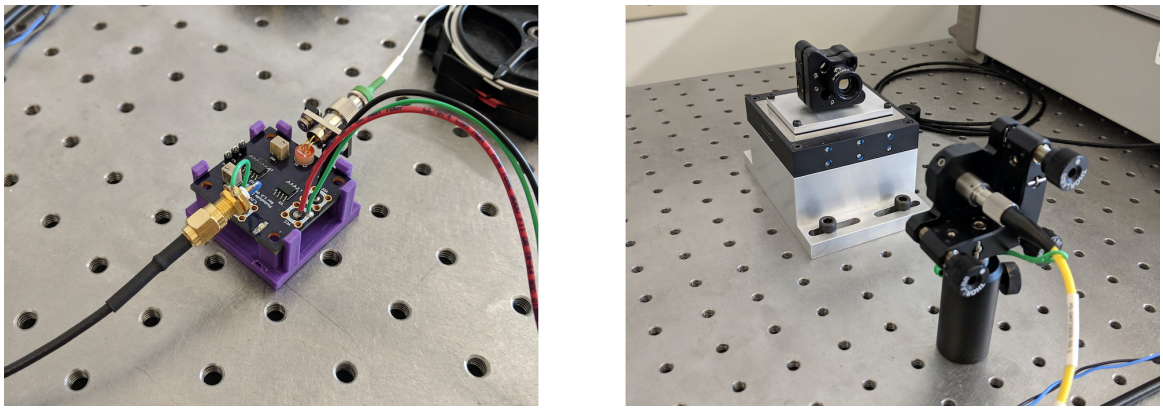

Figure 5.8: The photodetector circuit board (left) with the circulator connected to an InGaAs photodiode and an SMA connector which carries the photodetector signal to the FPGA. The launching setup (right) with the fibre beamsplitter connected to the collimator and corner cube retroreflector mounted to a linear piezo stage.

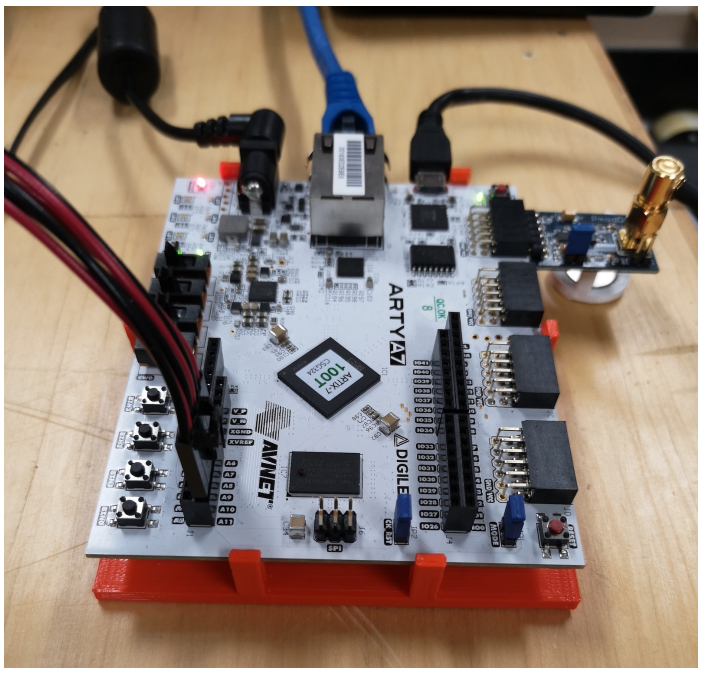

Figure 5.9: Digilent Arty A7-100T FPGA. The signal from the photodetection circuitry is carried by the wires plugged into the lower left header of the FPGA. A Digilent Pmod DA3 DAC is connected via the upper right Pmod port. The FPGA is connected to a PC by the USB serial and Ethernet connections on the top of the board.

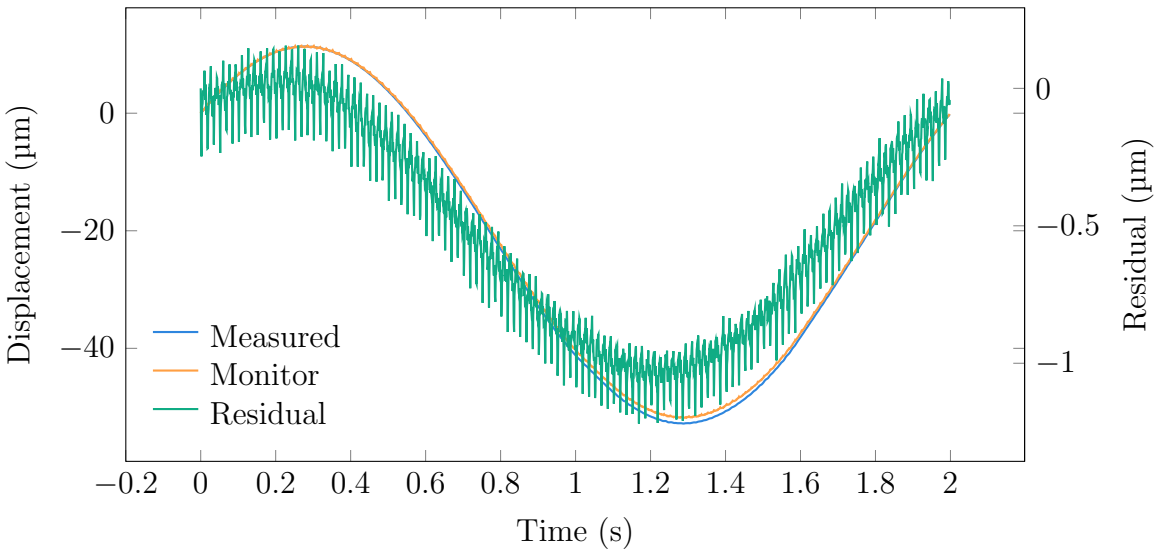

Figure 5.10: Measured and stage monitor displacements using the frequency modulation proof of concept. The residual shows 60 Hz electrical mains pickup on the stage position monitor signal.

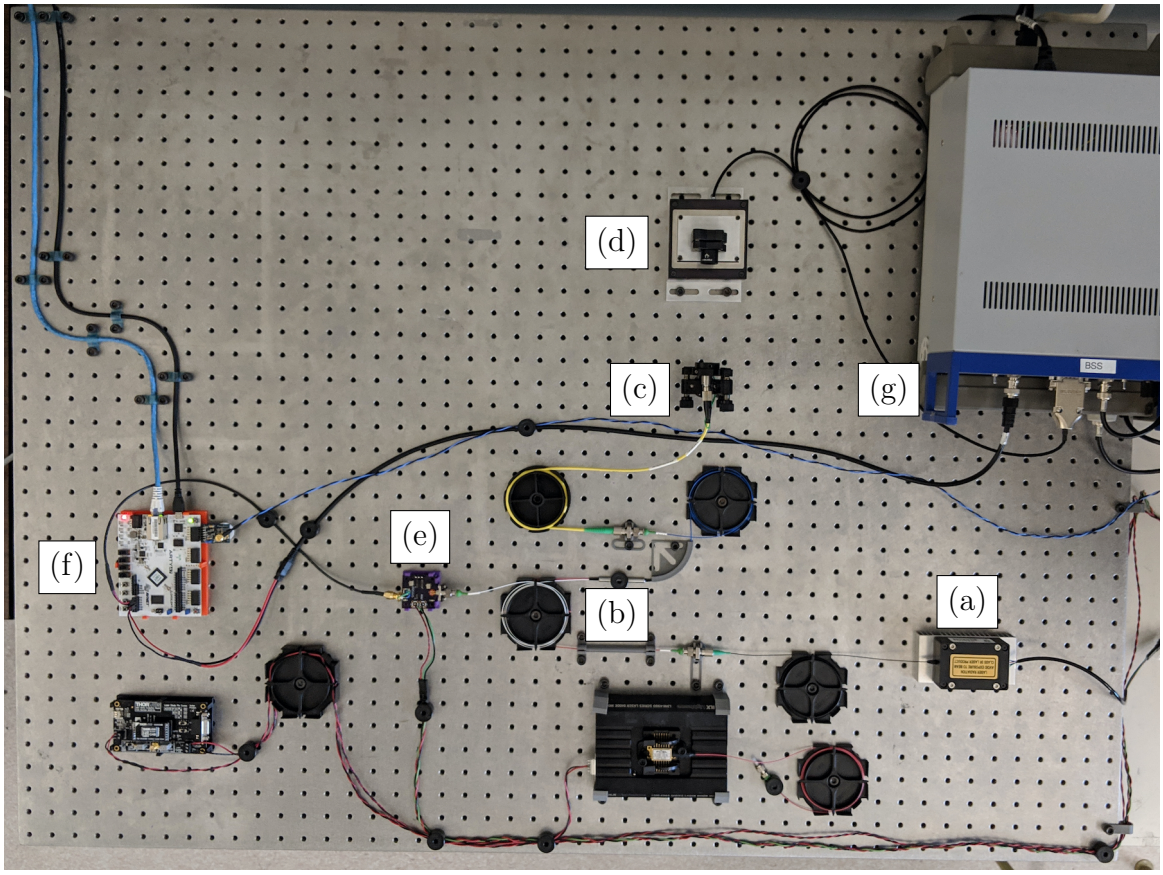

Figure 5.11: The proof of concept bench top room temperature experimental setup. The laser (a) emits light into the first arm of the circulator (b). A fibre optic patch cord connects the second arm of the circulator to a collimator (c), and the end of the fibre mated to the collimator has a 50:50 beamsplitter coating. The light coupled into the collimator is launched toward a retroreflector mounted on a linear piezo stage (d). The reflected beam is coupled back into the fibre by the collimator, where it is guided through the circulator to an InGaAs photodiode (e). The FPGA (f) digitizes the detector signal and the stage position monitor signal from the stage controller (g). The photodetector, FPGA, and some fibres are fitted with custom 3D printed components to secure them to the bench and reduce stress in the fibres at bend points.

stage controller was uncalibrated and serves as an approximate measure of the true stage position. The measured displacement agrees with the analog position monitor to 634 nm rms in a 0.5 Hz bandwidth, which corresponds to the length of the entire acquisition. The 60 Hz ripple in the residual is from the analog position monitor signal due to mains pickup from the stage controller, and not due to mechanical influences. A sinusoidal fit to the data shows a 535 nm rms error with the measured position in

a 20 Hz bandwidth, indicating that the presence of scaling in the uncalibrated position monitor signal and mains pickup has a significant impact on the disagreement between the measured and monitored displacements.

5.3.2 Performance at 4 K in Vacuum

The bench top interferometer from Subsection 5.3.1 was installed in a cryogenic test facility [90]. As the piezo stage cannot be operated in the cryostat, a rotary cryogenic stage was used instead and driven with a sinusoidal motion profile at 3.8 K [76]. For small displacements of $\ll 100\,\mu\text{m}$, the translation of the rotary stage can be considered approximately linear. The launching and stage configurations are the same as the cryogenic three-phase interferometer in Figure 4.16, but with one collimator-retroreflector pair instead of two.

Sinusoidal laser bias modulation at a frequency of $f_\text{m} = 1\,\text{kHz}$, with a V_bias over the range of 360 mV to 440 mV led to a laser frequency modulation amplitude $\nu_\text{A} = 6.859\,\text{GHz}$ about a centre optical frequency $\nu_\text{c} = 193.537\,602\,\text{THz}$, and the centre OPD was measured to be $\Lambda_0 = 14\,\text{cm}$. As with the previous bench top experiment, the interferometer efficiency was not measured, since the offline processing procedure automatically power normalizes based on the expected laser output power. Compared to the bench top experiment in Subsection 5.3.1, the modulation frequency band is approximately twice as wide to compensate for the OPD decreasing by a factor of ~ 2. This was done to keep the fringe rate at a similar value in both experiments, which is ~ 15 samples per modulation period. The fringe rate was chosen so that the data is sufficiently oversampled by a 1 MHz ADC with 1 kHz laser modulation.

The measured displacement is plotted in Figure 5.12, along with a sinusoidal fit. The residual of this fit, shown in Figure 5.12, exhibits a 32 nm rms error over the entire range and 31 nm rms error with a 20 Hz bandwidth. However, the residual has a strong 21 Hz component, which is apparent from its power spectrum shown in Figure 5.13.

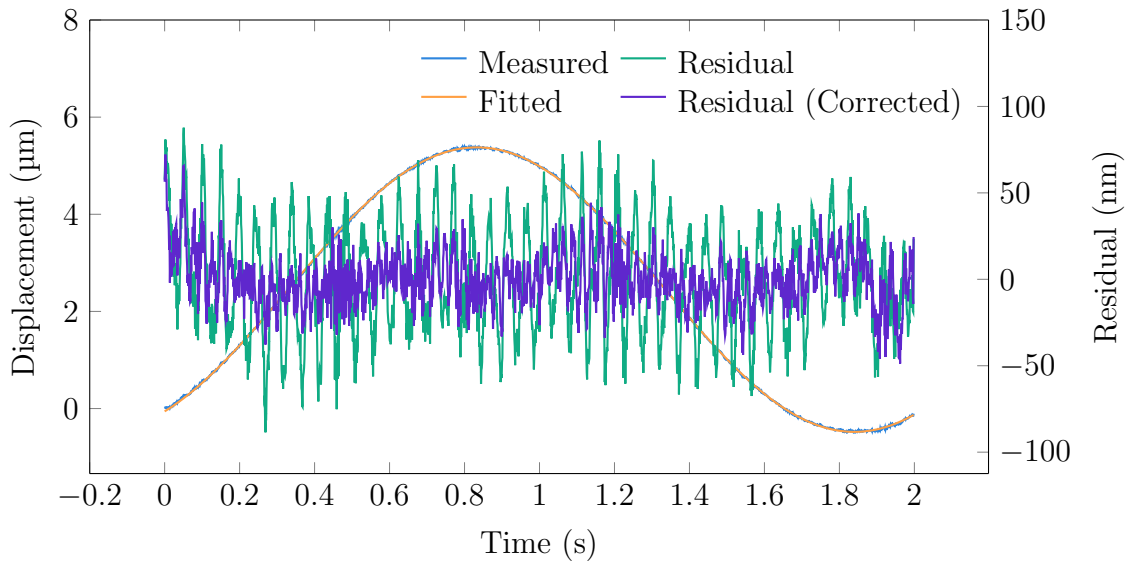

Figure 5.12: Measured and fitted displacement of a cryogenic stage using the frequency modulated technique at 3.8 K. The measured and 21 Hz corrected residuals are shown.

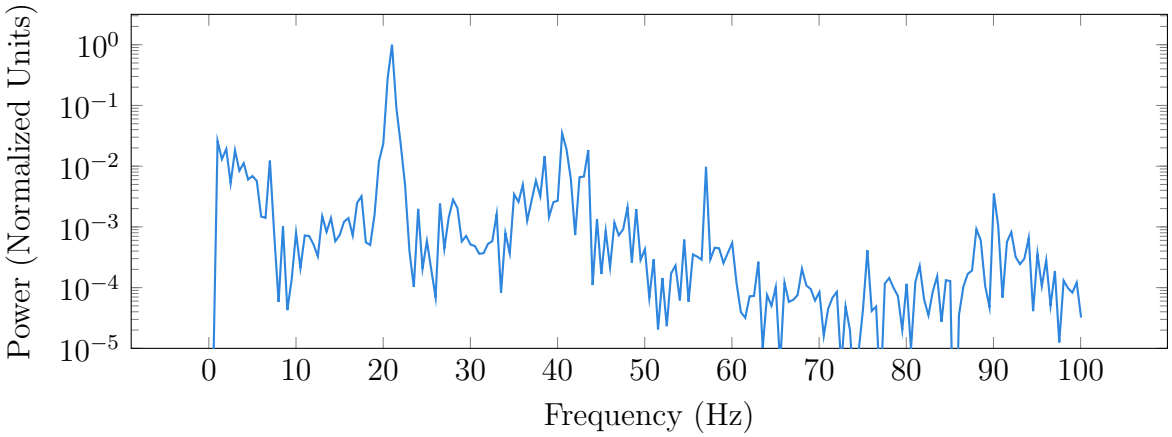

Figure 5.13: Power spectrum of the uncorrected cryogenic stage displacement measurement residual.

With the exception of the peak at 21 Hz, the power spectrum shows that the noise is white, and that $1/f$ noise is not dominant.

The source of the 21 Hz component is unknown but is believed to be due to some induced vibration. To visualize the effect of the noise on the overall performance, a Fourier transform of the residual was taken and the 19 Hz to 23 Hz band was flattened to produce a noise corrected residual, shown in Figure 5.12. The corrected residual has a 15 nm rms error over the full range and 14 nm rms error with a 20 Hz bandwidth.

5.4 MPSoC-based Processing Experiment

The final experiment presented in this thesis took place during the onslaught of the COVID-19 pandemic, and laboratory access was revoked as a preventative measure. In order to demonstrate the MPSoC-based signal processing system, I devised and performed an experiment at home with limited equipment.

The entire signal processing routine was implemented in a Digilent Cora Z7-10 development board [64], shown in Figure 5.15. A Digilent Pmod DA3 DAC [85] was used to modulate the bias of an Eblana DX1-DM laser module [69]

To demonstrate the ability of the system to track displacement for an extended period of time, thermal expansion of an optical breadboard shown in Figure 5.14 was measured. A launching collimator and retroreflector were mounted to a breadboard at a fixed distance from each other. A hair dryer was used to increase the temperature of the breadboard, causing the separation between the collimator and retroreflector to increase as the breadboard expands.

The laser was modulated at a frequency of $f_\mathrm{m} = 2.5\,\mathrm{kHz}$, with a sinusoidal bias modulation, V_bias, in the range of 240 mV to 300 mV. The modulation sweeps through an 8 GHz bandwidth of laser frequencies, with a laser frequency modulation amplitude $\nu_\mathrm{A} = 4.005\,\mathrm{GHz}$ about a centre optical frequency $\nu_\mathrm{c} = 193.557\,528\,\mathrm{THz}$. The OPD is twice the separation of the collimator and retroreflector, which was measured to be

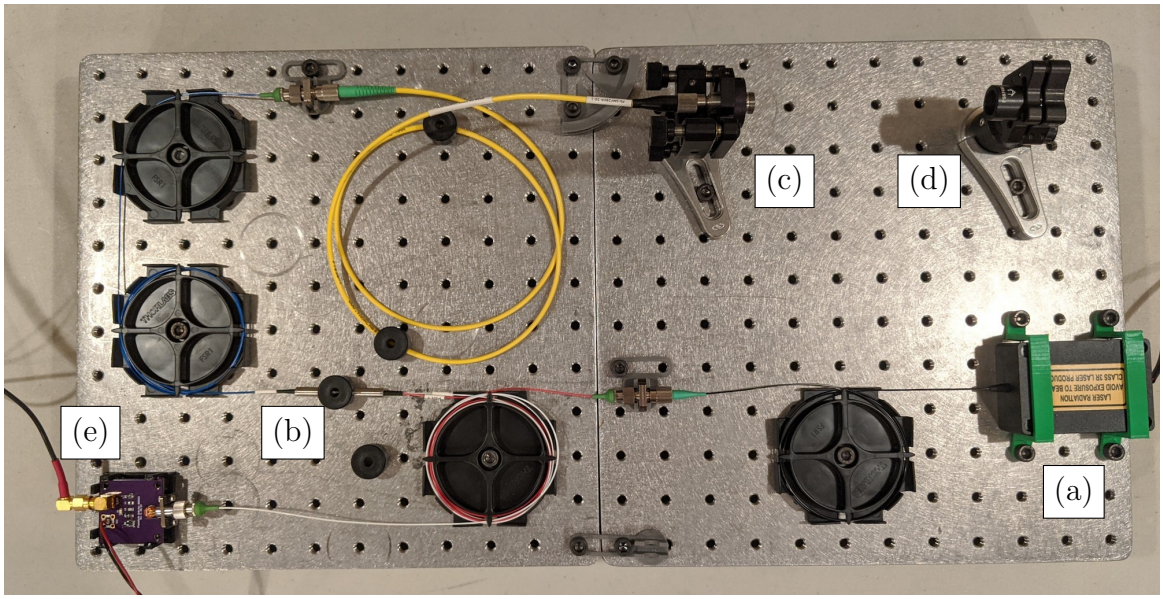

Figure 5.14: The MPSoC-based room temperature experimental configuration. The laser at (a) is modulated by an MPSoC (not pictured). Laser light travels to the circulator at (b), then to the collimator at (c), to which the beamsplitter coated fibre is inserted. A retroreflector is fixed to the post at (d). The reflected signals travel back through the circulator and to the photodetection circuit board at (e), where the signal is detected and transmitted to the MPSoC.

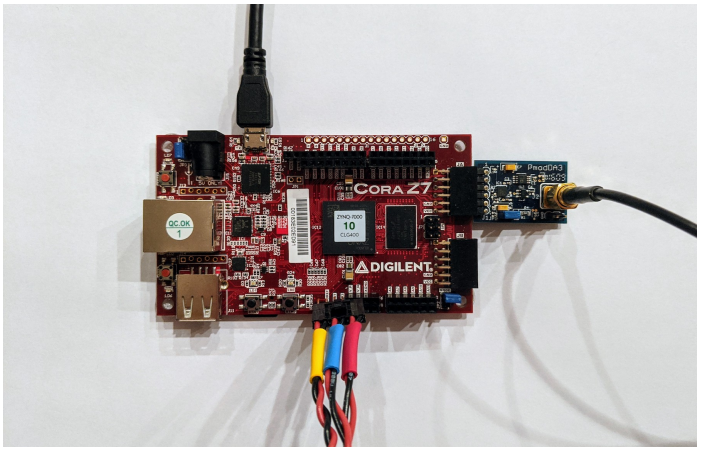

Figure 5.15: Digilent Cora Z7-10 with USB serial connection (top) to a PC, Pmod DA3 DAC (right) to modulate the laser, and analog signal from photodetector (bottom) to the internal ADC.

$\Lambda_0 = 30\,\text{cm}$. The interferometer efficiency, which is the ratio of the central laser output power to the central power reaching the detector, was measured to be $\eta_{\text{eff}} = 0.5$.

The displacement is computed by the MPSoC, which updates internally at 1 MHz, and is read out over USB serial at a rate of 62.5 Hz. Data were collected for a total of 15 minutes. Heating was applied to the bench for the first 30 s, and was then left to cool for the rest.

Without access to a precision stage, such as the linear piezo stage employed in the experiment presented in Subsection 5.3.1, I used thermal expansion to cause a change in OPD. From Fourier's law of thermal conduction, it is expected that the rate of heat transfer is exponential, and since the temperature change is small, the expansion will follow the temperature. As expected, both heating and the cooling exhibit an exponential shape, but with different growth and decay rates. Two functions were fitted, $\Delta x_{\text{heat}}(t)$ and $\Delta x_{\text{cool}}(t)$, for the heating and cooling sections, respectively. These fits are shown in Figure 5.16, and are described by the following equations:

$$\Delta x_{\text{heat}}(t) = -81.3 \exp\left(-\frac{t}{32.6}\right) + 66.7, \qquad [\mu\text{m}] \quad (5.28a)$$

$$\Delta x_{\text{cool}}(t) = 20.9 \exp\left(-\frac{t}{421}\right) + 0.595. \qquad [\mu\text{m}] \quad (5.28b)$$

Equation 5.28 shows that heating and cooling have two different time constants, which are 33.6 s and 421 s, respectively. Heat transfer due to active heating is more rapid than the slow convection to the ambient air during cooling, leading to a significantly greater time constant for cooling than heating.

An error of 168 nm rms was measured in a 20 Hz bandwidth for the measured position against the fit in the heating section, Δx_{heat}. However, this is not a particularly useful metric, as the heating process introduces noise due to vibrations caused by the hair dryer and changes in the refractive index of the optical path by moving air. For this reason, the error of the heating curve is largely ignored in this analysis, and the

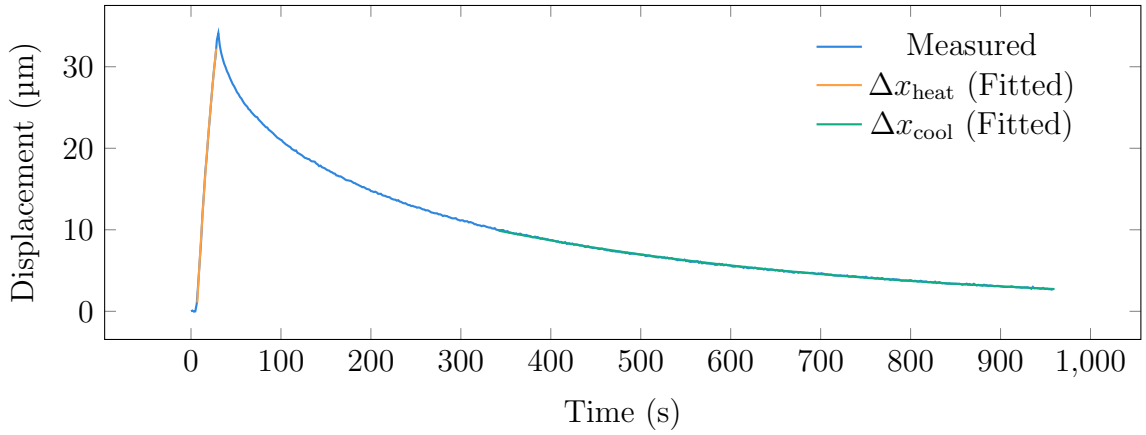

Figure 5.16: Measured displacement with exponential fits for the heating and cooling regions.

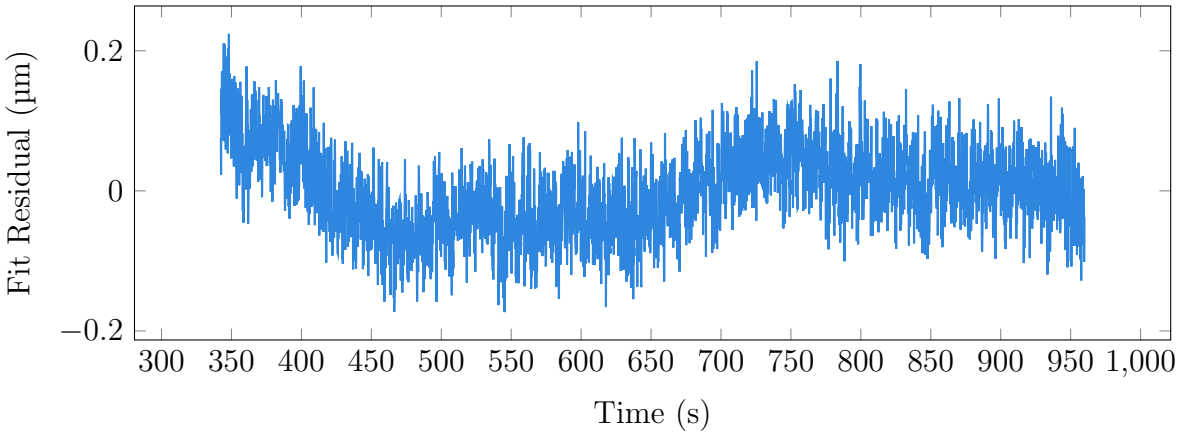

Figure 5.17: The fit residual for the cooling region.

less noisy cooling process is preferred to give a more realistic measure of accuracy.

The entire range of data in the cooling segment was not fitted, as can be seen in Figure 5.16. This is due to the curve not being entirely exponential. Heating by a hair dryer is non-uniform, which in turn introduces non-uniform expansion. The largest effects of non-uniform heating will be observed early on in the cooling process when the contraction of the material is most rapid, therefore, approximately the first 1/3 of the points were neglected and the remaining 2/3 were fitted.

The residual of the cooling fit, Δx_{cool}, which is the difference between the measured

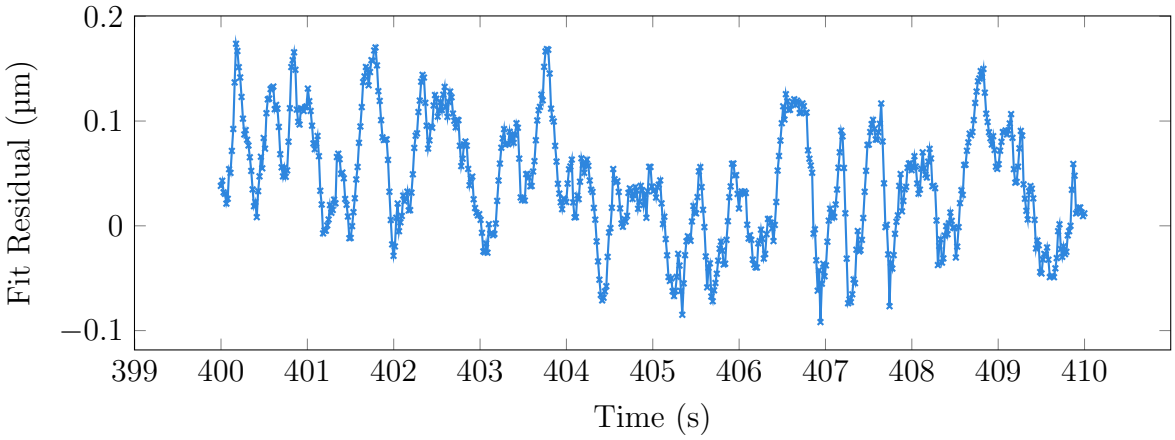

Figure 5.18: Select region of the cooling fit residual.

and fitted data, is shown in Figure 5.17, and exhibits an error of 51 nm rms in a 20 Hz bandwidth. The largest point-to-point jump in the residual is 106 nm, which is 212 nm in OPD. The laser wavelength is modulated around 1.55 µm so a jump of 775 nm or greater in OPD would represent a phase unwrapping error, and the maximum observed jump is far below this threshold. Figure 5.18 zooms in on an arbitrary section of Figure 5.17, so that the point-to-point jumps can be better observed. These data can then be compared with the three-phase interferometer discussed in Chapter 4, in which point-to-point jumps frequently exceeding $\lambda/2$ were frequent, as shown in Figure 4.20. The frequency modulation interferometer has demonstrably improved stability for long duration low velocity measurements.

The power spectrum of the residual is shown in Figure 5.19. Due to the sampling at 62.5 Hz and mains pickup of 60 Hz, the pickup is aliased and manifests as harmonics of 2.5 Hz with visible peaks in the power spectrum. There is a dramatic $1/f$ envelope showing that frequencies < 0.1 Hz dominate the power spectrum. Frequencies in this range carry over 100 times more power than the fundamental mains alias at 2.5 Hz. Since Parseval's theorem states that integral of the square of a signal in both time and frequency domains is equal, or physically, the energy in both domains is equal [91], removing a noise contribution in the frequency domain will improve performance in

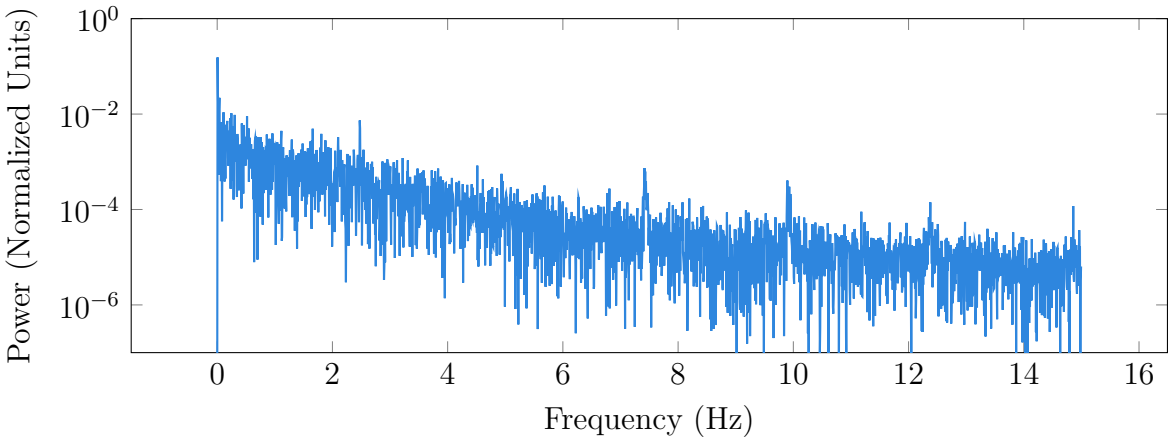

Figure 5.19: Power spectrum of the cooling fit residual.

the time domain.

In order to obtain an estimate of the true error, the low frequency components were artificially removed by taking the Fourier transform of the residual, zeroing the frequency bins less than 0.1 Hz, and then taking the inverse Fourier transform. The power at low frequencies is believed to be caused by two effects. First, there is a fitting error due to the curve not being entirely exponential. The fit intersects the measured position in the style of a secant line, where the fit begins as an underestimate, is an overestimate in the middle, and is an underestimate again at the end. Second, the low pass filter implementation does not decimate the output, which on the time scale of one modulation period, causes multiple small fluctuations around the true encoded phase during phase unwrapping. These fluctuations are difficult to study without a higher throughput readout channel that is faster than the modulation frequency. The lack of decimation allows the displacement to update at the same rate as the ADC, however, it is at the cost of additional noise. Removing the < 1 Hz frequencies is expected to suppress the effects of fitting errors, however, it is not known what frequencies are introduced due to a lack of filter decimation, and the full effects of filtering will need to be studied in future work. With the < 1 Hz band eliminated, the error improved from 51 nm rms to 36 nm rms in a 20 Hz bandwidth.

It is important to consider that the experiment was performed outside of a laboratory setting due to restrictions placed in response to the COVID-19 pandemic. Even under non-ideal conditions, nanometre scales were measured on the same order of magnitude as the optimal case experiment presented in Subsection 5.3.2, which was conducted in the laboratory under vacuum.

5.5 Conclusions

In this chapter, the technique of frequency modulation range-resolved laser interferometry has been presented, including experiments at room and cryogenic temperatures. Experimental results demonstrate that the advantage of frequency modulation laser interferometry over three-phase laser interferometry is the ability to largely avoid $1/f$ noise and associated phase jumps. The cryogenic experiment in Subsection 5.3.2 exhibits a flat power spectrum, where the dominating noise profile is white. A longer acquisition in the thermal expansion experiment with fully MPSoC-based processing demonstrated the ability for the system to track a slowly varying displacement over time with no evidence of phase jumps. However, in the MPSoC implementation, the lack of filter decimation was flagged as a potential issue to be explored in future work.

The frequency modulation technique has been shown to be superior to three-phase approach due to its stability over long duration measurements. In future work, the system will be implemented using a Digilent Eclypse Z7 [86], which features an MPSoC that is ~ 3 times larger than the current hardware. It will employ 100 MHz ADCs and DACs, allowing modulation rates up to 100 times faster than the current design. The improvement in hardware will lend itself to support demodulation of multiple axes, allowing the simultaneous measurement of multiple OPDs.

Chapter 6

Future Work

Two cryogenic range-resolved interferometer designs were presented, and the frequency modulation interferometer concept in Chapter 5 was demonstrated to be superior to the three-phase approach in Chapter 4. The frequency modulation interferometer will be adopted for future projects, not only for its improved low frequency performance, but also its lower power dissipation and simplicity. Table 6.1 provides a high-level comparison of three-phase and frequency modulation interferometric approaches as they pertain to implementation in a cryogenic space environment. As space missions require full redundancy, minimization of the interferometer mass and thermal load is critical. The following sections describe the future plans for further enhancements to the frequency modulation interferometer.

Table 6.1: Comparison of three-phase and frequency modulation interferometers for application in a cryogenic space environment.

Metric	Three-phase Interferometry	Frequency Modulation Interferometry
Number of components	Many	Few
Susceptible to $1/f$ noise	Yes	No
Laser power for 1 mW on detector	9 mW	1 mW
Fibres to < 4 K (parasitic)	2	1
Redundant load	Large	Small
Signal processing	Simple	Complex

6.1 Frequency Modulation Interferometry Improvements

Many lessons were learned through the implementation of the frequency modulation signal processing logic in hardware. Improvements to the system are based on both the future desired feature set and shortcomings that were identified in the initial implementation.

6.1.1 Hardware

A Digilent Cora Z7-10 [64] development board was selected for the initial implementation due to its low cost and ability to satisfy the speed requirements of the system. During development and testing, it became clear that the choice of hardware was suboptimal, as a significant portion of the logic was required for synchronization of signals originating from different clocks. The low speed ADC and DAC each required different clocks, which were themselves different from the master clock. Synchronization of this kind requires a complex effort to solve in logic, and an elegant solution is a change of hardware.

A Digilent Eclypse Z7 development board [86] featuring a Xilinx Zynq-7000 [65] that is $\sim$ 3 times larger than the current MPSoC, along with 100 MHz ADC and DAC expansion cards, was procured. The system operates on a single clock due to the 100 MHz rate of the ADC and DAC, eliminating the need for the current synchronization logic and allowing development to focus on signal processing. Additionally, the factor of 100 increase in speed from the 1 MHz ADC and DAC allows for faster laser modulation which enables the measurement of greater translation velocities according to Equation 5.27.

6.1.2 Real-Time Operating System

A bare-metal program running on the processing system of the MPSoC was used in the initial implementation. Due to the lack of any hard real-time deadlines, a custom cooperative task scheduler was built to avoid third-party dependencies. Such

a system is adequate for the needs of the initial design, but it falls short for future design plans. The next version will be built upon FreeRTOS [82], which is officially supported on Xilinx hardware. FreeRTOS will offer reduced development and maintenance overhead, as core features for multitasking are already implemented. A planned feature is to replace the USB serial with network communication through the 1 Gb Ethernet transceiver on the Eclypse Z7. Network access will allow for control of and data export from the system and is greatly simplified by FreeRTOS.

6.1.3 Digital Filters

Due to its simple and efficient hardware implementation, a cascaded integrator-comb was implemented to provide low-pass filtering of the demodulated signal. Noise in the recovered displacement was attributed to a lack of down sampling of the filter output, known as decimation, which affects the stability of the quadrature signal. Modelling how decimation affects quadrature signal stability may lead to the introduction of a new demodulation parameter, the decimation rate, which can be tuned to trade noise for higher cadence measurement or *vice versa*. Further exploration into more complex types of FIR filters, such Chebyshev and Butterworth, may offer a performance improvement, but must be considered alongside their complex hardware implementations. It may be that the transition from a simple cascaded integrator-comb filter to a more complex filter is not worth the cost in added complexity.

6.1.4 Extension to Multiple Axes

Kissinger describes the frequency modulation technique for the simultaneous measurement of multiple axes [50], and I have implemented it for a single axis. By leveraging that OPDs of different lengths are encoded in different frequency bands, it is possible to measure multiple axes simultaneously with a single laser, a single photodetector, and a simple interferometer design. The complexity of multiple axis demodulation arises in signal processing, which requires modification to the exist-

ing system. Adding support for multiple axis demodulation will not only increase the utility of the system, but also enable the development of new types of photonic instrumentation, such as the cryogenic accelerometer described in Section 6.4.

6.1.5 Automatic Parameter Discovery

The frequency modulation technique described in this thesis provides a relative displacement measurement. Other frequency modulation techniques provide absolute position measurements, such as the approach reported by Shi [92]. Shi employs linear frequency modulation, and through a Fourier transform of the detected signal, produces a distance spectrum encoding the lengths of all OPDs. The technique was able to achieve 50 µm resolution at > 8 m range.

Incorporating absolute displacement measurement will allow the system to automatically discover modulation and demodulation parameters. Currently, the user must manually provide as input initial estimates of the central OPD of the axis, Λ_0, the modulation frequency, f_{m}, the central laser frequency, ν_{c}, the laser frequency modulation amplitude, ν_{A}, and the interferometer efficiency, η_{eff}, all of which are described in Section 5.1. All of these parameters can be selected automatically — even on a multiple axis system — by performing an absolute distance measurement as a calibration step. Moving forward, automatic parameter discovery is an invaluable feature as it simplifies redeployment and lifts the knowledge burden from the user.

6.1.6 Error Analysis

A thorough error analysis of the frequency modulation interferometer was not performed as part of the initial implementation. The accuracy of the system is determined experimentally, with no theoretical lower bound established. A complete error analysis will provide a metric to allow optimization of the system design by identifying the limiting contributors to the error budget in different applications, such as laser stability, photodetector noise, and computational error sources.

6.2 Performance Verification

To provide an accurate experimental measure of cryogenic range resolved interferometer techniques, it is critical to have knowledge of the target position in the cryostat. The current verification strategy is to drive a stage with a known displacement profile, such as a linear or sinusoidal profile, and fit the appropriate curve to the measured displacement. A robust verification strategy would involve comparison against a second displacement reading from a verified position metrology system. In the past, attempts were made using a Renishaw interferometer built around a helium-neon (HeNe) laser. The Renishaw was operated at room temperature in the laboratory and probed through a cryostat window but, was unreliable due changes in alignment caused by unavoidable differential contractions during cooling [93].

HeNe lasers are considered the "gold standard" in metrology due to their wavelength stability, and a 632.8 nm fibre-fed HeNe laser interferometer will be constructed for verification. The interferometer will not produce a quadrature signal, only a single

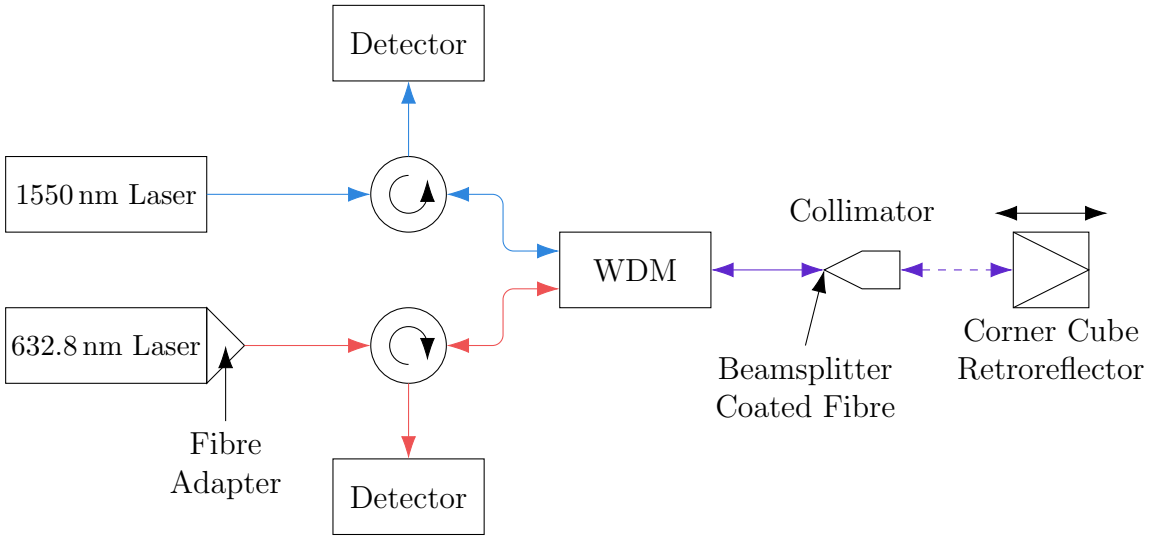

Figure 6.1: Schematic of a multiband 632.8 nm and 1550 nm fibre-based WDM interferometer concept. 632.8 nm HeNe laser light is shown in red, 1550 nm diode laser light in blue, and combined 632.8 nm and 1550 nm in purple. HeNe lasers are generally not fibre coupled, and fibre coupling is achieved by an optomechanical adapter.

sinusoid, which is capable of measuring a change in distance but not displacement. For testing purposes, the fibre-fed HeNe interferometer is sufficient for measuring a displacement when the translation is known to be unidirectional.

Adding a second laser introduces alignment issues, as demonstrated by attempts to couple an external Renishaw laser interferometer with a cryostat [93]. When two sources are used, it is unlikely that both beams will be perfectly parallel. Since the displacement measurements are on the nanometre scale, even a small deviation from parallelism will manifest as a cosine error. I propose a novel multiband fibre-fed interferometer, in which both the 632.8 nm and 1550 nm lasers share the same optical path by means of a multiband wave division multiplexer (WDM), as shown in Figure 6.1. Sharing the optical path eliminates cosine errors, and any effects due to vibration and thermal expansion are common to both signals so as to not artificially reduce the measured accuracy.

6.3 Cryogenic Materials Properties Testing

Cryogenic properties of common materials, such as the CTE of aluminum, are well understood [78]. With the increasing popularity of composites such as carbon fibre reinforced polymers (CFRP), their properties at cryogenic temperatures must be understood if they are to be considered for cryogenic applications. A potential cryogenic application for CFRPs is the construction of large space-based telescope mirrors, for which they offer a lightweight alternative to traditional materials, such as glass. With the densities of CFRP and borosilicate glass being $1.8\,\mathrm{g/cm^3}$ and $2.2\,\mathrm{g/cm^3}$, respectively, a CFRP mirror boasts an 18 % reduction in mass, however, one must also consider that CFRP is a sturdier material than glass. The construction of a CFRP mirror requires less material than a similarly sized glass mirror, which offers the potential for over an order of magnitude mass reduction.

Both the three-phase and frequency modulation interferometers have been used

to characterize cryogenic CTEs for CFRPs [56, 57], but other properties, such as Young's modulus, can also be measured using these interferometers. The frequency modulation interferometer, however, offers a number of advantages for cryogenic testing. With multiple axes demodulation, a number of samples can be simultaneously measured in a single thermocycle. As CFRPs are constructed with different fibre orientations, the CTE is expected to be directional. Consider a CFRP where all fibres are parallel. As it is cooled, the fibres contract less than the epoxy that binds them, and the CTE measured in the direction parallel to the fibres will be less than the CTE measured perpendicularly. With the frequency modulation interferometer, both of these directional CTEs can be found via simultaneous length measurements.

6.4 Cryogenic Accelerometry

Accelerometry at $< 4\,\mathrm{K}$ is challenging: commercially available accelerometers can operate in a cryogenic environment, but must be heated for the electronics to function properly. Due to the difficulty of reaching temperatures $< 4\,\mathrm{K}$, the addition of heat into the cryostat is undesirable, and in some cases, prohibitive. The ability of the frequency modulation interferometer to simultaneously provide measurements for multiple axes with little thermal power dissipation at cryogenic temperatures shows that it is an excellent candidate for a cryogenic accelerometer. Furthermore, with one laser and one detector being common to multiple axes [50], there is no need for the gain and offset adjustment of individual photodetectors, which is required for the three-phase interferometer in Chapter 4.

In addition to supporting multiple axis demodulation, a mechanism must be constructed to allow the interferometer to measure three independent axes. This can be achieved by duplicating the collimator and retroreflector for each axis to build three free space interferometer arms, similar to the one shown in Figure 5.3. The free space design can leverage commercially available components, but the mechanism is rela-

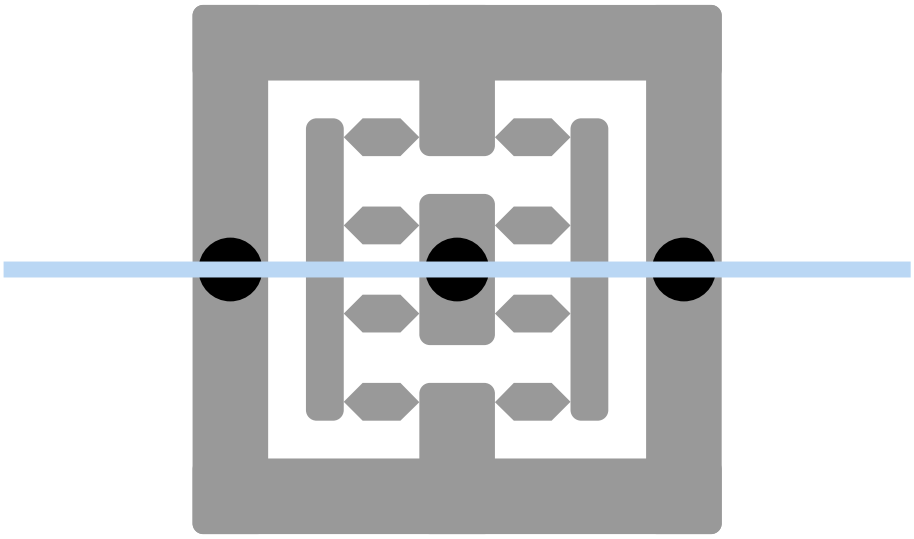

Figure 6.2: A single axis fibre-based accelerometer flexure mechanism concept. The fibre is bonded to the linear flexure at the locations of the black circles. The flexure stage can translate vertically. When the flexure stage departs from the equilibrium position, the lengthening of the fibre can be measured by fibre segment interferometry.

tively massive and will occupy a large volume. An alternative concept foregoes all free space optics, and instead, uses fibre segment interferometry by stretching fibres mounted to flexures, as shown in Figure 6.2. A further exploration of the feasibility of both design types will be conducted to determine the optimal cryogenic accelerometer construction.

6.5 Conclusions

Two cryogenic range-resolved laser interferometers utilizing three-phase and frequency modulation techniques were successfully constructed and tested. Thermal expansion of the fibres and $1/f$ noise were limiting to the performance of the initial three-phase design. Fibre thermal expansion was addressed through the introduction of a custom armoured differential fibre that could be sunk to different thermal sinks in a cryostat, which allowed the system to achieve high accuracy during cryogenic testing. $1/f$ noise was still an issue during low velocity translations, which led to the development of a frequency modulation interferometer. Although the frequency

modulation interferometer did not exhibit the same accuracy as the differential three-phase interferometer, it was shown to measure a very slowly varying displacement for an extended period, demonstrating that it does not experience similar adverse effects due to $1/f$ noise. Suggested improvements to the signal processing hardware and design enable multiple axis measurement and improved utility of the system. A proposed multiband interferometer will provide a technique for the verification of the frequency modulation interferometer against a second, well understood interferometer.

In continuing research, a range of applications of the frequency modulation interferometer will be explored, the most exciting of which is a low power cryogenic three axis accelerometer for lunar seismology. Building upon the success of seismometers placed during Apollo missions [94], NASA has proposed a lunar seismology campaign as part of the Lunar Geophysical Network mission [95]. During lunar night, which lasts over 13.5 earth days, the surface temperature of the moon can drop as low as 100 K — with even more extreme temperatures of ~ 25 K in polar craters. A seismometer deployed on the moon must not only able to survive lunar night, but also operate at extremely low temperatures with limited available power. It can be seen that virtually all aspects of a lunar seismometer are similar to those of the SAFARI metrology system, for which I have shown that a fibre-fed laser interferometer can provide precise, low power position metrology at < 4 K, making it a promising candidate for lunar deployment.

Bibliography

[1] P. R. Roelfsema, H. Shibai, L. Armus, D. Arrazola, M. Audard, M. D. Audley, C. M. Bradford, I. Charles, P. Dieleman, Y. Doi, et al. SPICA — a large cryogenic infrared space telescope: unveiling the obscured universe. *Publications of the Astronomical Society of Australia*, 35, 2018.

[2] D. van Loon, A. Cournoyer, and D. Naylor. SAFARI FTS development plan. Technical Report SRON-SAF-PL-2020-003, Netherlands Institute for Space Research, 2020.

[3] A. A. Ned and J. VanDeWeert. *Selecting Strain Gages Silicon vs Metal Foil*. Kulite Semiconductor Products, Inc.

[4] A. J. Fleming. A review of nanometer resolution position sensors: operation and performance. *Sensors and Actuators A: Physical*, 190:106–126, 2013.

[5] C. S. Smith. Piezoresistance effect in germanium and silicon. *Physical review*, 94(1):42, 1954.

[6] C. Ferrero, C. Marinari, and E. Martino. Calibration systems for strain gauges to be used at cryogenic temperatures. *Sensors and actuators. A Physical*, 31(1-3):125–129, 1992.

[7] HBM Test and Measurement. *HBM Strain Gauges*, 2019.

[8] T. R. Hicks, P. D. Atherton, Y. Xu, and M. McConnell. *The NanoPositioning Book*. Queensgate Instruments Torquay, Torbay, UK, 1997.

[9] Queensgate Instruments. *NanoSensors – NX Series*, 2018. Ver. 1.

[10] Capacitec, Inc. *4100-SC/4101-SC Specifications*, 2010.

[11] Micro-Epsilon. *capaNCDT 6110 Datasheet*. Available: `https://www.micro-epsilon.com/download/products/cat-capa/dax--capaNCDT-611x--en-us.html`.

[12] M. R. Nabavi and S. Nihtianov. A survey of eddy current displacement sensors: Imperfections and signal conditioning methods. In *Proc. Int. Sci. Appl. Sci. Conf*, pages 116–122, 2007.

[13] M. F. Kessler, J. A. Steinz, M. E. Anderegg, J. Clavel, G. Drechsel, P. Estaria, J. Faelker, J. R. Riedinger, A. Robson, B. G. Taylor, et al. The Infrared Space Observatory (ISO) mission. *Astronomy and Astrophysics*, 315:L27–L31, 1996.

[14] G. R. Davis, I. Furniss, W. A. Towlson, P. A. R. Ade, R. J. Emery, W. M. Glencross, D. A. Naylor, T. J. Patrick, R. C. Sidey, and B. M. Swinyard. Design and performance of cryogenic, scanning Fabry-Perot interferometers for the Long-Wavelength Spectrometer on the Infrared Space Observatory. *Applied Optics*, 34(1):92–107, 1995.

[15] P. E. Clegg, P. A. R. Ade, C. Armand, J-P Baluteau, M. J. Barlow, M. A. Buckley, J-C Berges, M. Burgdorf, E. Caux, C. Ceccarelli, et al. The ISO long-wavelength spectrometer. *Astronomy & Astrophysics*, 315(2):L38–L42, 1996.

[16] H. D. Young, R. A. Freedman, and A. L. Ford. *University Physics*. Pearson, Boston, 14 edition, 2016.

[17] Micro-Epsilon. *eddyNCDT Catalog*. Available: `https://www.micro-epsilon.com/download/products/cat--eddyNCDT--en-us.pdf`.

[18] Lion Precision. *ECL202 High-Resolution*, 2019. Available: `https://www.lionprecision.com/wp-content/uploads/2019/04/EddyCurrent-ECL202.pdf`.

[19] Keyence. *EV-108M Data Sheet*. Available: `https://www.keyence.com/products/sensor/proximity/ev/models/ev-108m/`.

[20] Kaman Precision Products. *SC-2440 Data Sheet*, 2014. Available: `https://www.kamansensors.com/wp-content/uploads/2017/03/Kaman_SC-2440_data_sheet_web.pdf`.

[21] S. Calcutt, F. Taylor, P. Ade, V. Kunde, and D. Jennings. The Composite Infrared Spectrometer. *Journal of the British Interplanetary Society*, 45:381–386, 1992.

[22] C. F. Hakun and K. A. Blumenstock. A cryogenic scan mechanism for use in Fourier transform spectrometers. 1995.

[23] P. Sagar, A. S. Gour, and R. Karunanithi. A multilayer planar inductor based proximity sensor operating at 4.2 K. *Sensors and Actuators A: Physical*, 264:151–156, 2017.

[24] D. S. Nyce. Linear position sensors. In *Theory and Application*, volume 4, pages 62–77. Wiley Online Library, 2004.

[25] Monitran. *Economy Series AC LVDT with Plain Core*, 2017.

[26] Honeywell. *Model DLB DC-DC Data Sheet*, 2008.

[27] S-T Wu, S-C Mo, and B-S Wu. An LVDT-based self-actuating displacement transducer. *Sensors and Actuators A: Physical*, 141(2):558–564, 2008.

[28] M. Martino, A. Danisi, R. Losito, A. Masi, and G. Spiezia. Design of a linear variable differential transformer with high rejection to external interfering magnetic field. *IEEE Transactions on Magnetics*, 46(2):674–677, 2010.

[29] M. W. Werner, T. L. Roellig, F. J. Low, G. H. Rieke, M. Rieke, W. F. Hoffmann, E. Young, J. R. Houck, B. Brandl, G. G. Fazio, et al. The Spitzer space telescope mission. *The Astrophysical Journal Supplement Series*, 154(1):1, 2004.

[30] R. D. Gehrz, T. L. Roellig, M. W. Werner, G. G. Fazio, J. R. Houck, F. J. Low, G. H. Rieke, B. T. Soifer, D. A. Levine, and E. A. Romana. The NASA Spitzer space telescope. *Review of Scientific Instruments*, 78(1):011302, 2007.

[31] G. H. Rieke, E. T. Young, J. Cadien, C. W. Engelbracht, K. D. Gordon, D. M. Kelly, F. J. Low, K. A. Misselt, J. E. Morrison, J. Muzerolle, et al. On-orbit performance of the MIPS instrument. In *Optical, Infrared, and Millimeter Space Telescopes*, volume 5487, pages 50–61. International Society for Optics and Photonics, 2004.

[32] R. M. Warden and G. B. Heim. Cryogenic scan mirror mechanism for SIRTF/MIPS. In *32nd Aerospace Mechanisms Symposium*, page 45, 1998.

[33] Heidenhain. *Exposed Linear Encoders*, 2014. Available: `https://www.heidenhain.us/lp/encoders/ExposedLinearEncoders.pdf`.

[34] K. J. King and S. J. Leeks. *SPIRE Instrument User Manual*, 2009. Issue 1.5.

[35] M. Kawada et al. Performance of an imaging Fourier transform spectrometer with photoconductive detector arrays: an application for the AKARI far-infrared instrument. *Publications of the Astronomical Society of Japan*, 60(sp2):S389–S397, 2008.

[36] G. L. Pilbratt et al. Herschel Space Observatory – an ESA facility for far-infrared and submillimetre astronomy. *Astronomy & Astrophysics*, 518:L1, 2010.

[37] M. J. Griffin et al. The Herschel-SPIRE instrument and its in-flight performance. *Astronomy & Astrophysics*, 518:L3, 2010.

[38] H. Murakami et al. The infrared astronomical mission AKARI. *Publications of the Astronomical Society of Japan*, 59(sp2):S369–S376, 2007.

[39] D. A. Naylor, J-P Baluteau, M. J. Barlow, D. Benielli, M. Ferlet, T. R. Fulton, M. J. Griffin, T. Grundy, P. Imhof, S. Jones, et al. In-orbit performance of the Herschel/SPIRE imaging Fourier transform spectrometer. In *Space Telescopes and Instrumentation 2010: Optical, Infrared, and Millimeter Wave*, volume 7731, page 773116. International Society for Optics and Photonics, 2010.

[40] B. M. Swinyard et al. Imaging FTS for Herschel SPIRE. In *IR Space Telescopes and Instruments*, volume 4850, pages 698–709. International Society for Optics and Photonics, 2003.

[41] D. B. Leviton. Image processing for new optical pattern recognition encoders. In *Algorithms and Systems for Optical Information Processing IV*, volume 4113, pages 32–40. International Society for Optics and Photonics, 2000.

[42] D. B. Leviton, T. Anderjaska, J. Badger, T. Capon, C. Davis, B. Dicks, W. Eichhorn, M. Garza, C. Guishard, S. Haghani, et al. Cryogenic optical position encoders for mechanisms in the JWST optical telescope element simulator (OSIM). In *Cryogenic Optical Systems and Instruments 2013*, volume 8863, page 886306. International Society for Optics and Photonics, 2013.

[43] J. B. Marion and W. F. Hornyak. *Physics for Science and Engineering*. Saunders College Publishing, 1982.

[44] A. Einstein. Näherungsweise integration der feldgleichungen der gravitation. 1916.

[45] B. P. Abbott et al. LIGO: the Laser Interferometer Gravitational-Wave Observatory. *Reports on Progress in Physics*, 72(7):076901, 2009.

[46] A. A. Michelson and E. W. Morley. On the relative motion of the earth and of the luminiferous ether. *Sidereal Messenger, vol. 6, pp. 306-310*, 6:306–310, 1887.

[47] E. Hecht. *Optics*. Addison-Wesley, 4th edition, 2002.

[48] B. E. A. Saleh and M. C. Teich. *Fundamentals of Photonics*. Wiley Series in Pure and Applied Optics. John Wiley & Sons, Inc., Hoboken, NJ, 2nd edition, 2007.

[49] Renishaw plc. *L-8003-3193-02 B Data Sheet: HS20 laser head*, 2015.

[50] T. Kissinger. *Range-Resolved Optical Interferometric Signal Processing*. PhD thesis, Cranfield University, 2015.

[51] Renishaw plc. *L-9904-2352-06-B Data Sheet: RPI20 parallel interface*, 2014.

[52] A. J. Christiansen, D. A. Naylor, I. T. Veenendaal, and B. G. Gom. A frequency-modulated laser interferometer for nanometer-scale position sensing at cryogenic temperatures. In *Photonic Instrumentation Engineering VI*, volume 10925, page 1092514. International Society for Optics and Photonics, 2019.

[53] Thorlabs, Inc. *SMF-28-J9 Datasheet*, 2015. Rev. H.

[54] I. Veenendaal, D. Naylor, B. Gom, T. Fulton, A. Christiansen, W. Jellema, M. Eggens, and P. Ade. A novel design for a cryogenic angle-scanned Fabry-Pérot interferometer. In *Advances in Optical and Mechanical Technologies for Telescopes and Instrumentation III*, volume 10706, page 107061C. International Society for Optics and Photonics, 2018.

[55] D. Naylor, I. Veenendaal, T. Fulton, B. Gom, A. Christiansen, W. Jellema, C. Feenstra, M. Eggens, and P. Ade. First light results from a novel cryogenic Fabry-Pérot interferometer. In *2019 44th International Conference on Infrared, Millimeter, and Terahertz Waves (IRMMW-THz)*, pages 1–2. IEEE, 2019.

[56] L. D. Spencer, I. T. Veenendaal, D. A. Naylor, B. G. Gom, G. R. H. Sitwell, A. I. Huber, A. Christiansen, et al. Composite material evaluation at cryogenic temperatures for applications in space-based far-infrared astronomical instrumentation. In *Advances in Optical and Mechanical Technologies for Telescopes and Instrumentation III*, volume 10706, page 107063R. International Society for Optics and Photonics, 2018.

[57] L. D. Spencer, A. Christiansen, I. T. Veenendaal, S. Gunuganti, D. A. Naylor, B. G. Gom, G. R. H. Sitwell, N. Zobeiry, and A. Poursartip. Evaluation of composite materials at cryogenic temperatures. In *Canadian International Conference on Composite Materials – CANCOM 2019*, Kelowna, British Columbia, Canada, July 2019. Oral presentation.

[58] M. Abramowitz and I. A. Stegun. Handbook of Mathematical Functions. *National Bureau of Standards Applied Mathematics Series*, 55:589–626, 85.

[59] H. Nyquist. Certain topics in telegraph transmission theory. *Transactions of the American Institute of Electrical Engineers*, 47(2):617–624, April 1928.

[60] S. M. Qasim, S. A. Abbasi, and B. Almashary. A review of FPGA-based design methodology and optimization techniques for efficient hardware realization of computation intensive algorithms. In *2009 International Multimedia, Signal Processing and Communication Technologies*, pages 313–316, 2009.

[61] J. J. Rodriguez-Andina, M. J. Moure, and M. D. Valdes. Features, design tools, and application domains of FPGAs. *IEEE Transactions on Industrial Electronics*, 54(4):1810–1823, 2007.

[62] Digilent Inc. *Arty A7 Reference Manual*. Available: `https://reference.digilentinc.com/reference/programmable-logic/arty-a7/reference-manual`.

[63] Xilinx, Inc. *Artix-7 FPGAs Data Sheet: Overview*, 2018. Ver. 2.6.

[64] Digilent Inc. *Cora Z7 Reference Manual*. Available: `https://reference.digilentinc.com/reference/programmable-logic/cora-z7/reference-manual`.

[65] Xilinx, Inc. *Zynq-7000 SoC Data Sheet: Overview*, 2018. Ver. 1.11.1.

[66] W. Wolf, A. A. Jerraya, and G. Martin. Multiprocessor system-on-chip (MPSoC) technology. *IEEE Transactions on Computer-Aided Design of Integrated Circuits and Systems*, 27(10):1701–1713, 2008.

[67] M. P. Knapp. Sines and cosines of angles in arithmetic progression. *Mathematics Magazine*, 82(5):371, 2009.

[68] E. Clarke. *Circuit analysis of AC power systems; symmetrical and related components*, volume 1. Wiley, 1943.

[69] Eblana Photonics. *DX1–DM EP-xxxx-DM-DX1 Laser Module with Current and TEC Control User Manual*, 2013. Rev. 0.1.

[70] Thorlabs, Inc. *PS974M-C Datasheet*, 2018. Rev. A.

[71] Thorlabs, Inc. *FGA01FC Datasheet*, 2012. Rev. C.

[72] Xilinx, Inc. *7 Series FPGAs and Zynq-7000 SoC XADC Dual 12-Bit 1 MSPS Analog-to-Digital Converter User Guide*, 2018. Ver. 1.10.1.

[73] J. E. Volder. The CORDIC trigonometric computing technique. *IRE Transactions on Electronic Computers*, EC-8(3):330–334, 1959.

[74] AZoM. *Stainless Steel - Grade 430 (UNS S43000)*, 2001. Available: `https://www.azom.com/article.aspx?ArticleID=996`.

[75] AZoM. *Silica Silicon Dioxide (SiO2)*, 2001. Available: `https://www.azom.com/article.aspx?ArticleID=1114`.

[76] I. Veenendaal, D. Naylor, B. Gom, A. Christiansen, W. Jellema, C. Feenstra, M. Ridder, M. Eggens, and P. Ade. An angle-scanned cryogenic Fabry-Pérot interferometer for far-infrared astronomy. *Review of Scientific Instruments*, 91(8):083108, 2020.

[77] PJRC. *Teensy++ USB Development Board*. Available: `https://www.pjrc.com/store/teensypp.html`.

[78] Material Properties: 6061-T6 Aluminum (UNS A96061). `https://trc.nist.gov/cryogenics/materials/6061%20Aluminum/6061_T6Aluminum_rev.htm`. Accessed: 26 June 2020.

[79] Thorlabs, Inc. *P5-SMF28ER-50-1 Datasheet*, 2019. Rev. F.

[80] Analog Devices. *AD8615/AD8616/AD8618: Precision, 20 MHz, CMOS, Rail-to-Rail Input/Output Operational Amplifiers Data Sheet*, 2014. Rev. G.

[81] E. Hogenauer. An economical class of digital filters for decimation and interpolation. *IEEE Transactions on Acoustics, Speech, and Signal Processing*, 29(2):155–162, 1981.

[82] Real Time Engineers Ltd. *The FreeRTOS^{TM} Reference Manual*, 2016. Ver. 9.0.0.

[83] Micrium. *µC/OS-III Reference Manual*. Available: `https://doc.micrium.com/display/osiiidoc/uC-OS-III+Reference+Manual`.

[84] A. Silberschatz, P. B. Galvin, and G. Gagne. *Operating System Concepts*. John Wiley & Sons, 7th edition, 2004.

[85] Digilent Inc. *Pmod DA3 Reference Manual*. Available: `https://reference.digilentinc.com/reference/pmod/pmodda3/start`.

[86] Digilent Inc. *Eclypse Z7 Hardware Reference Manual*. Available: `https://reference.digilentinc.com/reference/programmable-logic/eclypse-z7/reference-manual`.

[87] G. van Rossum and F. L. Drake. *Python 3 Reference Manual*. CreateSpace, Scotts Valley, CA, 2009.

[88] T. Oliphant. *Guide to NumPy*. January 2006.

[89] PI. *PIHera Piezo Linear Precision Positioner Datasheet*, 2019.

[90] I. Veenendaal, D. Naylor, B. Gom, S. Gunuganti, C. Winter, M. Jones, and D. Walker. Performance of a cryogenic test facility for 4 K interferometer delay line investigations. In *Space Telescopes and Instrumentation 2016: Optical, Infrared, and Millimeter Wave*, volume 9904, page 99045E. International Society for Optics and Photonics, 2016.

[91] R. E. Ziemer, W. H. Tranter, and D. R. Fannin. *Signals and Systems: Continuous and Discrete*. Macmillon Publishing, 1st edition, 1983.

[92] G. Shi, F. Zhang, X-H Qu, and X. Meng. High-resolution frequency-modulated continuous-wave laser ranging for precision distance metrology applications. *Optical Engineering*, 53(12):1–7, 2014.

[93] I. Veenendaal. A cryogenic test facility. Master's thesis, University of Lethbridge, 2016.

[94] N. R. Goins, A. M. Dainty, and M. N. Toksöz. Lunar seismology: the internal structure of the moon. *Journal of Geophysical Research: Solid Earth*, 86(B6):5061–5074, 1981.

[95] C. Shearer and G. Tahu. Lunar Geophysical Network (LGN). Planetary science decadal survey, mission concept study report, 2010.

[96] Eblana Photonics. *1550nm DM Laser EP1550-DM-B Datasheet*, 2015. Rev. 2.1.

[97] Thorlabs, Inc. *6015-3-APC Datasheet*, 2013. Rev. C.

[98] Keysight Technologies. *Keysight Technologies N7744A 4-Channel Optical Multiport Power Meter Datasheet*, 2017.

[99] Keysight Technologies. *Keysight E3631A Triple Output DC Power Supply User's Guide*, 2018.

[100] EXFO Electro-Optical Engineering Inc. *EXFO WA-1000/WA-1500 Wavemeter*, 2006.

[101] Tektronix, Inc. *Digital Phosphor Oscilloscopes MSO4000 Series, DPO4000 Series Data Sheet.* Available: `https://www.tek.com/datasheet/dpo4000-series-digital-phosphor-oscilloscopes-datasheet`.

[102] A. Antoniou. *Digital Filters: Analysis and Design.* McGraw-Hill, New York, 1979.

[103] L. Euler. *Introduction to Analysis of the Infinite.* Springer Science & Business Media, 2012.

Appendix A

Laser Specifications

The specifications for Eblana DX1-DM laser modules [69], featuring an Eblana EP1550-DM-B laser diode [96], are presented in this appendix. A DX1-DM module is shown in Figure A.1, and both the electrical and optical specifications of the modules are summarized in Table A.1. The DX1-DM module does not allow direct bias current control, and instead, exposes a bias voltage input. Internally, the module scales the bias voltage by 100 mA/V to generate a bias current to feed the diode. The diode temperature is controlled similarly, but is always left floating, which sets the temperature controller at 25 °C.

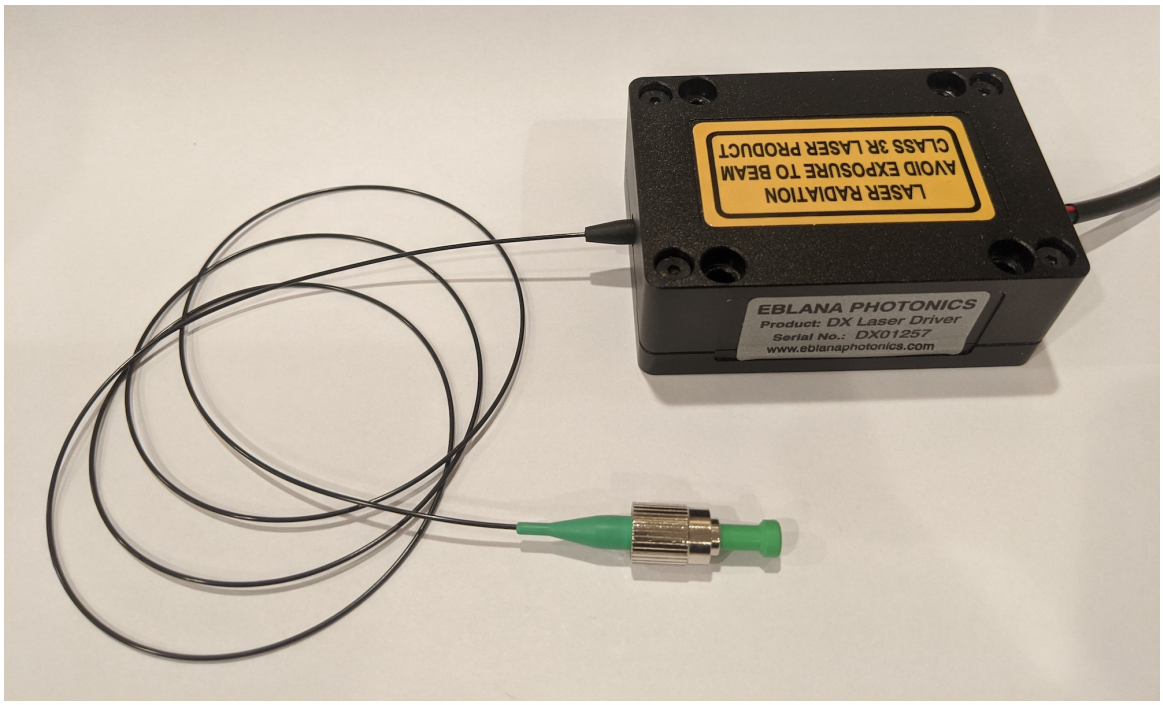

Figure A.1: An Eblana DX1-DM laser module. The laser output is coupled to an FC/APC terminated single-mode fibre.

Table A.1: Specifications of an Eblana DX1-DM laser module with an EP1550-DM-B laser diode [69, 96].

Parameter	Value
Bias voltage	0 V to 1.2 V
Bias current	0 mA to 120 mA
Bias current resolution	0.1 mA
Bias current accuracy	±0.2 mA
Bias current noise (10 Hz to 10 MHz)	< 2 µA
Bias current ripple (50 Hz rms)	< 2 µA
Bias current short-term fluctuations (15 s)	< 20 µA
Bias current drift (30 min, < 10 Hz)	< 50 µA
Optical power (maximum)	15 mW
Peak wavelength (typical)	1550 nm
Wavelength stability (CW)	< 10 pm
Spectral linewidth	< 800 kHz
Side mode suppression ratio (typical)	40 dB
Temperature tuning coefficient	0.1 nm/K
Current tuning coefficient	12 pm/mA
Slope efficiency	0.12 mW/mA
Modulation bandwidth	DC to 80 kHz
Operating temperature (submount)	15 °C to 35 °C

Appendix B

Ideal Interferometer Beamsplitter Ratio

Fringe visibility of the frequency modulation interferometer, presented in Chapter 5, can be optimized through the selection of beamsplitter ratio. Recall from Subsection 3.1.4 that the fringe visibility, $\mathcal{V}$, is described by

$$\mathcal{V} = \frac{I_{\max} - I_{\min}}{I_{\max} + I_{\min}} = \frac{2\sqrt{I_1 I_2}}{I_1 + I_2}, \tag{B.1}$$

where I_1 and I_2 are the intensities of the interfering beams, and $I_{\max}$ and $I_{\min}$ are the intensities of bright and dark interference fringes, respectively. The beamsplitter ratio, commonly reported as $\mathcal{R}$:$\mathcal{T}$, relates the intensity reflectance, $\mathcal{R}$, to the intensity transmittance, $\mathcal{T}$. When an interference signal is detected and digitized, the amount of information contained in the signal is governed by the fringe visibility. Through visibility optimization, the amplitude of the digitized signal can be maximized.

This analysis is based primarily around three quantities: the beamsplitter reflectance, $\mathcal{R}$, the beamsplitter transmittance, $\mathcal{T}$, and the efficiency of reflection in the interferometer, η_{r}, which is the fraction of intensity into the interferometer arm that returns to the beamsplitter. The beamsplitter absorption is assumed to be negligible, so that $\mathcal{R} + \mathcal{T} \approx 1$. η_{r} will be approximated by a constant, although in practice it varies with the traversed optical path length. If the beam is considered to be Gaussian, the beam radius increases approximately linearly along the beam axis, according to Equation 3.16, leading to a phenomenon known as beam dilution, which was introduced in Chapter 4 with Figure 4.2. Losses due to beam dilution of the beam are the dominant source of inefficiency, as only a fraction of the returning intensity can be collected when the beam radius exceeds the size of the collecting component.

Recall from Subsection 3.1.4 that the interference equation for monochromatic beams is:

$$I = I_1 + I_2 + 2\sqrt{I_1 I_2}\cos\phi, \qquad [\mathrm{W/m^2}] \tag{B.2}$$

where I_1 and I_2 are the intensities of the interfering beams, ϕ is the phase between the wavefronts of I_1 and I_2, and I is the resulting intensity. I_1 will be the intensity reflected by the beamsplitter, and I_2 the intensity transmitted through the beamsplitter, through the arm of the interferometer, and back through the beamsplitter a second time. However, a beamsplitter coating on an FC/PC terminated fibre is used,

which will split light that is either entering or exiting the fibre through the coated end, leading to the formation of a Fabry-Pérot cavity between the beamsplitter and the retroreflector. I_2 is then the interference of infinitely many beams, whose intensities decrease by a factor of $\eta_r\mathcal{R}$ from one to the next, and the phase of each beam is shifted by a constant, ϕ.

In modelling the Fabry-Pérot resonator, it will be assumed that the retroreflector is perfectly efficient does not introduce losses. As η_r decreases quadratically at each step due to beam dilution, the finesse of the cavity is low, resulting in large losses in the multiply reflected beams. For this reason, the effect can be approximated by only considering the beam which traverses the OPD once, and the multiply reflected beams are ignored. For an input intensity of I_0, I_1 and I_2 can then be expressed as

$$I_1 = \mathcal{R}I_0, \qquad [\mathrm{W/m^2}] \quad \text{(B.3a)}$$

$$I_2 = \frac{\eta_r\mathcal{T}^2 I_0}{\left(1-\sqrt{\eta_r\mathcal{R}}\right)^2 + 4\sqrt{\eta_r\mathcal{R}}\sin^2\left(\phi/2\right)} \approx \eta_r\mathcal{T}^2 I_0, \qquad [\mathrm{W/m^2}] \quad \text{(B.3b)}$$

where the exact form of Equation B.3b is the intensity when the interferometer is treated as a Fabry-Pérot resonator. For the rest of this analysis, the approximation of Equation B.3b will be used.

The visibility, which was covered in Subsection 3.1.4 and described by Equation 3.37, can be formulated using Equation B.3, as:

$$\mathcal{V} \approx \frac{2\mathcal{T}\sqrt{\eta_r\mathcal{R}}}{\mathcal{R}+\eta_r\mathcal{T}^2}. \qquad \text{(B.4)}$$

By squaring Equation B.4, η_r can be solved as a quadratic equation, having the two solutions:

$$\eta_r \approx \frac{\mathcal{R}}{\mathcal{V}^2\mathcal{T}^2}\left[2-\mathcal{V}^2+2\sqrt{1-\mathcal{V}^2}\right], \qquad \text{(B.5a)}$$

$$\eta_r \approx \frac{\mathcal{R}}{\mathcal{V}^2\mathcal{T}^2}\left[2-\mathcal{V}^2-2\sqrt{1-\mathcal{V}^2}\right]. \qquad \text{(B.5b)}$$

The second solution, Equation B.5b, is physically significant and provides an efficiency in the appropriate range of $[0, 1]$.

The transmission efficiencies for a Thorlabs 6015-3-APC fibre circulator [97] were measured using the experimental setup depicted in Figure B.1, where η_{12} and η_{23} are the efficiencies for transmission from the first to the second arm and the second to the third arm of the circulator, respectively. The input to first arm of the circulator was illuminated by a laser of known optical power, P, and the power received at the output of the second arm, $P_{12}$was measured. A Keysight N7744A power meter [98] was used to perform the measurements. The process was repeated with the second and third arms to measure P_{23}, and the measurements are summarized in Table B.1.

Two Thorlabs P5-SMF28ER-50-1 50:50 beamsplitter coated fibres [79] were tested by connecting the same laser to the first arm of the circulator, the uncoated tip to

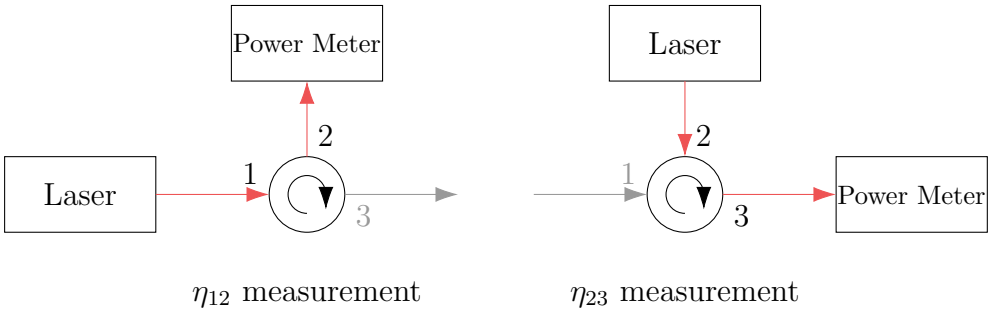

Figure B.1: Schematics of the experimental setups used to measure η_{12} and η_{23} of a Thorlabs 6015-3-APC fibre circulator. Arm 3 of the circulator is unconnected in the η_{12} measurement and arm 1 of the circulator is unconnected in the η_{23} measurement.

Table B.1: Efficiency measurements of a Thorlabs 6015-3-APC fibre circulator.

Parameter	Measurement	Unit
P	2.2272	mW
P_{12}	1.8885	mW
P_{23}	1.8195	mW
η_{12}	0.8479	—
η_{23}	0.8169	—

the second arm of the circulator, and the third arm of the circulator and beamsplitter coated tip to the power meter. The power transmitted through the beamsplitter was measured, as well as the power reflected by it that returned through the third arm of the circulator, as shown in Figure B.2.

The power measurements are corrected to account for the losses through the circulator. $P_{\mathcal{T}}$ only experiences losses through the first to second arms, while $P_{\mathcal{R}}$ experiences losses through the first to second and second to third arms, therefore, the corrected measurements, $P_{\mathcal{R},\text{corr}}$ and $P_{\mathcal{T},\text{corr}}$, respectively, are:

$$P_{\mathcal{R},\text{corr}} = P_{\mathcal{R}}/\eta_{12}\eta_{23}, \quad [\text{mW}] \quad \text{(B.6a)}$$

$$P_{\mathcal{T},\text{corr}} = P_{\mathcal{T}}/\eta_{12}. \quad [\text{mW}] \quad \text{(B.6b)}$$

The measured and corrected reflectance and transmittance of the 50:50 fibre beamsplitters are shown in Table B.2.

An interferometer was set up on the bench in the same fashion as the one presented in Chapter 5, with an OPD of $\sim 30\,\text{cm}$. The visibility was calculated with voltages measured by a photodetector, since the photodetector output is linear with the optical intensity. Bearing similarity to Equation 3.37, the visibility is expressed as

$$\mathcal{V} = \frac{V_{I,\text{max}} - V_{I,\text{min}}}{V_{I,\text{max}} + V_{I,\text{min}}}, \quad \text{(B.7)}$$

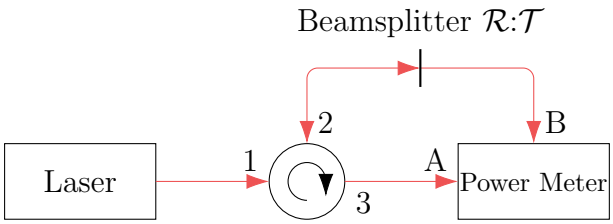

Figure B.2: Diagram of the testing setup for reflectance and transmittance measurements of a Thorlabs P5-SMF28ER-50-1 50:50 fibre beamsplitter. The reflected power is measured at port A of the power meter, and the transmitted power at port B.

Table B.2: Thorlabs P5-SMF28ER-50-1 50:50 fibre beamsplitter reflectance and transmittance measurements.

Beamsplitter	$P_{\mathcal{R}}$ (mW)	$P_{\mathcal{R},\text{corr}}$ (mW)	$P_{\mathcal{T}}$ (mW)	$P_{\mathcal{T},\text{corr}}$ (mW)	$\mathcal{R}$	$\mathcal{T}$
1	0.574	0.798	0.950	1.120	0.42	0.58
2	0.669	0.931	1.016	1.198	0.44	0.56

where $V_{I,\text{max}}$ and $V_{I,\text{min}}$ are the detector output voltages at the maximum and minimum intensities, respectively.

The fringe visibility measurements for each fibre are shown in table Table B.3. Using $\mathcal{R}$ and $\mathcal{T}$ from Table B.2 and solving Equation B.5b, the interferometer reflection efficiencies were found when each fibre beamsplitter was used.

Table B.3: Interferometer fringe visibility measurements using two fibres with 50:50 beamsplitters.

Beamsplitter	$V_{I,\text{max}}$ (V)	$V_{I,\text{min}}$ (V)	$\mathcal{V}$	η_r
1	11.95	2.09	0.70	0.11
2	10.71	2.07	0.68	0.10

To solve for the optical reflectance and transmittance which offer the best visibility, $\mathcal{R}_\text{opt}$ and $\mathcal{T}_\text{opt}$, respectively, $\mathcal{V} = 1$ was used along with $\mathcal{R}_\text{opt}$ and $\mathcal{T}_\text{opt}$ in Equation B.5b. The equation $\eta_\text{r} = \mathcal{R}_\text{opt}/\mathcal{T}_\text{opt}^2$ is found, which can be used to create the following system of equations:

$$\begin{cases} \eta_\text{r} \approx \mathcal{R}_\text{opt}/\mathcal{T}_\text{opt}^2 \\ 1 \approx \mathcal{R}_\text{opt} + \mathcal{T}_\text{opt}. \end{cases} \tag{B.8}$$

Solving Equation B.8 leads to Equations B.9 and B.10, whose solutions are sum-

Table B.4: Optimal fibre beamsplitter reflectance and transmittance. These values account for the reflection efficiency calculated using different 50:50 beamsplitter coated fibres.

Beamsplitter	$\mathcal{R}_{\text{opt}}$	$\mathcal{T}_{\text{opt}}$
1	0.09	0.91
2	0.08	0.92

marized in Table B.4.

$$\mathcal{R}_{\text{opt}} \approx \frac{2\eta_{\text{r}} + 1 - \sqrt{4\eta_{\text{r}} + 1}}{2\eta_{\text{r}}} \tag{B.9}$$

$$\mathcal{T}_{\text{opt}} \approx \frac{-1 + \sqrt{4\eta_{\text{r}} + 1}}{2\eta_{\text{r}}} \tag{B.10}$$

From the results presented in Table B.4, a beamsplitter of approximately 10:90 would result in optimal fringe visibility for this interferometer.

Appendix C

Frequency Modulation Laser Characterization

Frequency modulation interferometry requires a precise understanding of the laser diode behaviour. Since modulating the laser bias current changes both the laser output power and wavelength, calibration of both these two parameters as a function of bias current is necessary. A calibration procedure was established for measuring both of these curves, which are then approximated by polynomial fits.

The Eblana DX1-DM module [69] was powered by an Agilent E3631A DC power supply [99], and its bias voltage, V_{bias}, was swept through a range of values using a second port on the supply. The laser was stabilized to 25 °C using its internal temperature control circuitry. Power measurements were recorded with a Keysight N7744A optical power meter [98], and wavelength measurements were recorded with an EXFO WA-1500 wavemeter [100], to obtain P_{laser} and λ as functions of bias current, respectively, Wavelength measurements were only taken when the laser power was above 1 mW, due to minimum power requirements of the wavemeter. For both power and wavelength measurements, 5 values were recorded and the mean and standard deviation of the mean were reported, as summarized in Table C.1.

Eblana DX1-DM modules allow bias current injection via a voltage input which undergoes scaling and conversion in the module electronics. A factor of 100 mA/V is used to convert the bias voltage input to the module into the bias injection current to the laser diode [69].

A quadratic fit was applied to obtain laser power as a function of the bias voltage. The fit only considers the data points where the laser power is significantly greater than zero, which is the range of 0.150 V to 1.200 V in Table C.1, although in typical operation, the range of V_{bias} is limited to 250 mV to 400 mV. The resulting fit is

$$P_{\text{laser}}\left(V_{\text{bias}}\right) = -2.47V_{\text{bias}}^2 + 15.66V_{\text{bias}} - 2.15, \qquad [\text{mW}] \quad \text{(C.1)}$$

which is plotted in Figure C.1a. Generally, laser optical power is presented as a linear function of the bias voltage (or current), however, to improve signal processing accuracy, a second order fit was applied to capture the quadratic nature of the curve.

A third order polynomial was fit to the laser wavelength as a function of bias

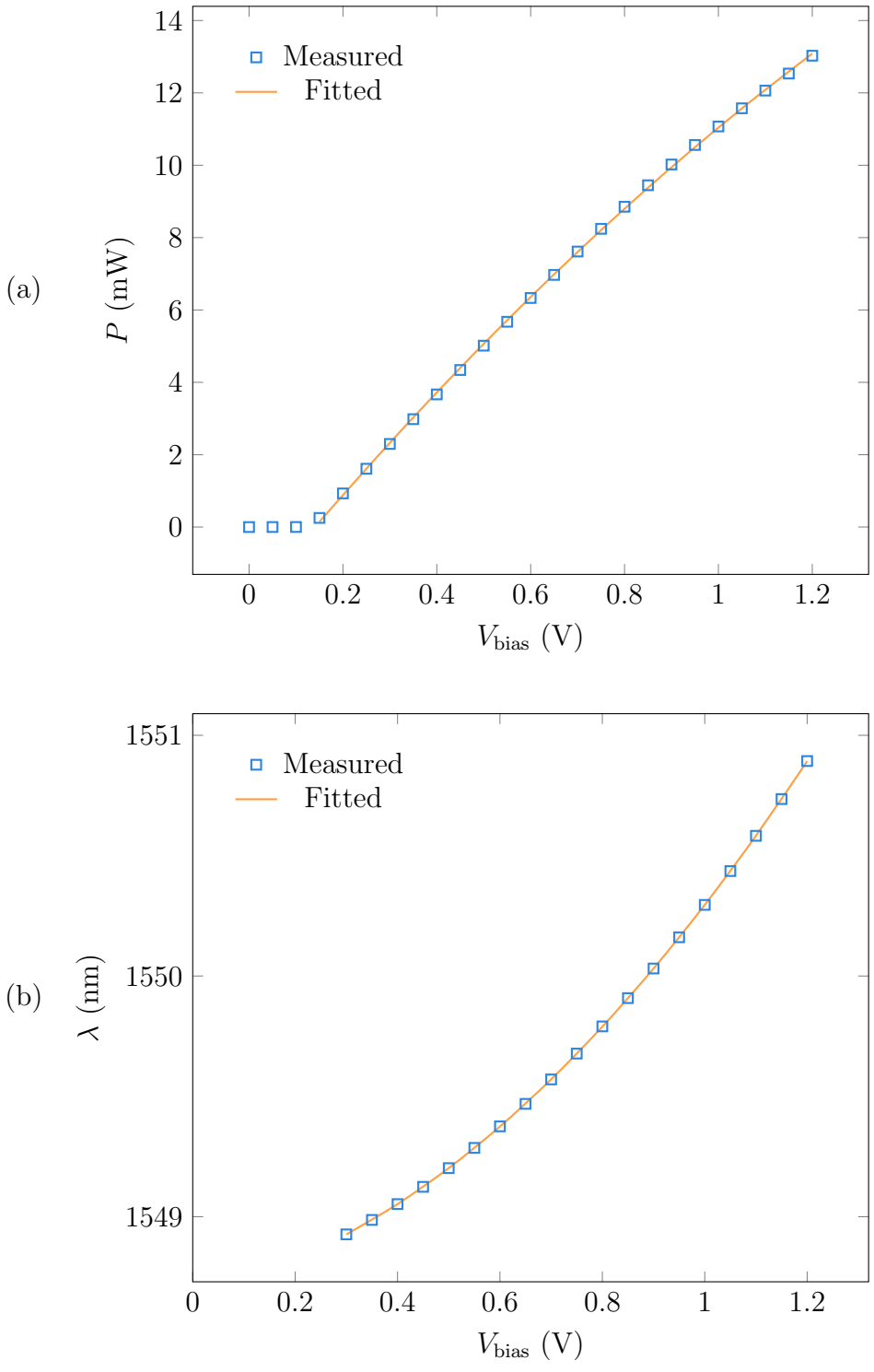

Figure C.1: Plots of the measured and fitted power (a) and wavelength (b) curves at 25 °C.

Table C.1: Eblana DX1-DM power and wavelength measurements. Power and wavelength errors are reported as standard deviation of the mean of 5 measurements for each bias.

V_{bias} ($\text{V} \pm 0.001\,\text{V}$)	P_{laser} ($\text{mW} \pm 0.002\,\text{mW}$)	λ ($\text{nm} \pm 0.0002\,\text{nm}$)
0.000	0.000	—
0.050	0.001	—
0.100	0.002	—
0.150	0.252	—
0.200	0.930	—
0.250	1.612	—
0.300	2.297	1548.9267
0.350	2.982	1548.9867
0.400	3.666	1549.0525
0.450	4.341	1549.1241
0.500	5.013	1549.2019
0.550	5.674	1549.2859
0.600	6.331	1549.3754
0.650	6.969	1549.4689
0.700	7.615	1549.5704
0.750	8.243	1549.6778
0.800	8.853	1549.7907
0.850	9.447	1549.9082
0.900	10.021	1550.0312
0.950	10.559	1550.1610
1.000	11.072	1550.2954
1.050	11.574	1550.4360
1.100	12.064	1550.5824
1.150	12.534	1550.7351
1.200	13.028	1550.8931

voltage, producing

$$\lambda\left(V_{\text{bias}}\right) = -0.02V_{\text{bias}}^3 + 1.19V_{\text{bias}}^2 + 0.43V_{\text{bias}} + 1548.69, \qquad [\text{nm}] \quad \text{(C.2)}$$

which is shown in Figure C.1. A third order fit was chosen for Figure C.1b by a matter of convention, as third order polynomials are typically used for approximating the relationship between wavelength and bias of a laser diode.

Appendix D

Frequency Modulation Photodetector Characterization

Correct demodulation of the interference signal in the frequency modulation interferometer requires knowledge of the optical power, P_{pd}, which reaches the photodetector. In practice, the photodetector circuitry produces a voltage, V_{pd}, which is a function of the optical power incident on the detector. A characterization of the photodetector circuitry presented in Subsection 5.2.3 is necessary to obtain a transfer function from which P_{pd} can be determined from V_{pd}.

The Eblana DX1-DM laser module [69], for which optical power as a function of bias voltage was characterized in Appendix C, was powered by an Agilent E3631A DC power supply [99] and connected directly to the photodetection circuit. The laser was stabilized to 25 °C using its internal temperature control circuitry, and its

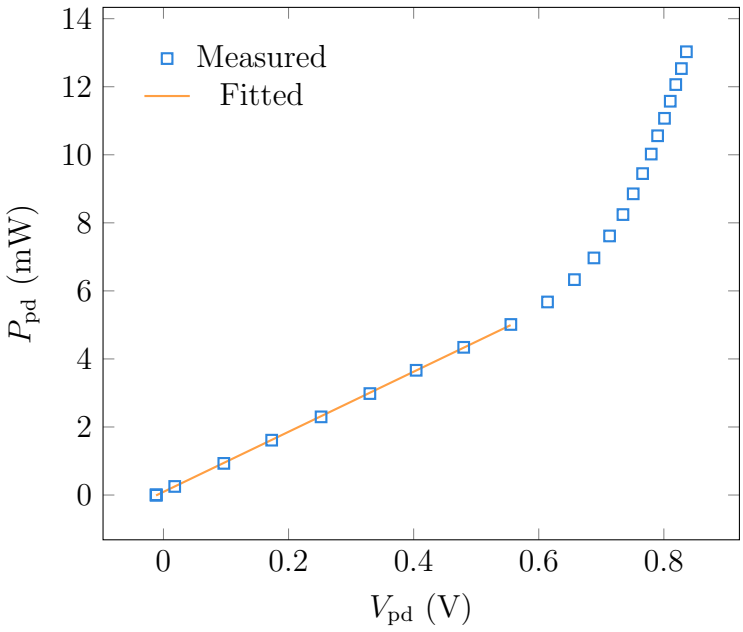

Figure D.1: Optical power at the photodetector versus the produced photodetector voltage.

Table D.1: Optical power at the photodiode and associated photodiode voltage. Power and wavelength errors are reported as standard deviation of the mean of 5 measurements.

P_{pd} ($\text{mW} \pm 0.0002\,\text{mW}$)	V_{pd} ($\text{V} \pm 0.0002\,\text{V}$)
0.0000	−0.0118
0.0005	−0.0116
0.0023	−0.0115
0.2522	0.0180
0.9303	0.0965
1.6121	0.173
2.2975	0.252
2.9822	0.330
3.6662	0.404
4.3412	0.480
5.0128	0.555
5.6743	0.614
6.3309	0.657
6.9687	0.688
7.6146	0.713
8.2428	0.735
8.8530	0.751
9.4472	0.766
10.0210	0.780
10.5591	0.790
11.0715	0.801
11.5740	0.810
12.0638	0.819
12.5336	0.828
13.0284	0.836

bias was controlled by a Digilent Pmod DA3 DAC [85] driven by a Digilent Cora Z7-10 MPSoC [64]. The bias voltages were stepped through all values of Table C.1, for which precise P_{laser} measurements were recorded in Appendix C. The detector output was measured using a Tektronix DPO 4034 oscilloscope [101]. $P_{\text{pd}} = P_{\text{laser}}$ under the assumption that there are negligible optical losses between the laser and photodetector. The detector output voltage was measured as a function of laser power, summarized in Table D.1.

Since V_{pd} is the output of a system to which P_{pd} is the only input, it may initially seem backwards that the data from Table D.1 is plotted in Figure D.1 such that V_{pd} is the dependent variable. The plot was constructed in this way to illustrate that P_{pd} is being to fit to V_{pd}. Figure D.1 illustrates that the detector response is linear over the domain of approximately 0 mW to 5 mW, which when fitted results in the transfer

function:

$$P_{\mathrm{pd}}\left(V_{\mathrm{pd}}\right) = 8.83V_{\mathrm{pd}} + 0.09. \qquad [\mathrm{W}] \quad \text{(D.1)}$$

In practice, this transfer function can only be applied for $P_{\mathrm{pd}} \leq 5\,\mathrm{mW}$ due to the domain of the fit. The advantage is that this linear transfer function can be efficiently computed in hardware, whereas a fit over the entire range of data requires at least a 5^{th} order polynomial to serve as a reasonable approximation, which would introduce extra complexity.

Appendix E

Low-Pass Filtering

E.1 Introduction to Digital Filters

Digital filters can be organized into two groups: infinite impulse response (IIR) and finite impulse response (FIR) [91,102]. The output of an IIR filter is a function of every previous sample, meaning that the filter output integrates an infinite number of samples as $n \to \infty$. Instead of using all past samples, FIR filters use a finite window of the signal to produce the output. For example, suppose that a signal x is filtered to produce y, where n is the index into the signal, then one possible pair of IIR and FIR filters are

$$y_{\text{IIR}}[n+1] = y_{\text{IIR}}[n] + x[n], \tag{E.1a}$$

$$y_{\text{FIR}}[n+1] = x[n] + x[n-1], \tag{E.1b}$$

respectively. It is clear that y_{IIR} is an IIR filter due to its recursive definition, which can be expanded to include all previous values of x. Since y_{FIR} depends on only the previous two x values, it is an FIR filter because any y_{FIR} value can be fully expressed as a function of a finite number of x values.

IIR and FIR filters will be compared using select key differences: stability, phase shift, and practical considerations for implementation — which are summarized by Table E.1.

A filter is said to be stable if the output is finite for any finite input. When a filter is stable, for any bounded input such that $|x[n]| \leq \infty$, the output must satisfy $|y[n]| \leq \infty$ for all n. An IIR filter may or may not be stable, and the filter in

Table E.1: Comparison of IIR and FIR filters.

IIR	FIR
Can be stable or unstable	Always stable
Phase shift not easily described	Constant phase shift
Low-order tapping	High-order tapping
Requires less memory	Requires more memory
Requires less computation	Requires more computation
Simple to implement in hardware	Difficult to implement in hardware

Equation E.1a is unstable. Consider a constant input of $x[n] = 1$, then $y_{\text{IIR}}[n] = n$, which can never be bounded by a finite value. Because FIR filters only consider a finite number of samples, they are always stable for a stable input.

The phase shift of an FIR is constant, since the filter introduces a delay that is the same for any input frequency. The FIR filter in Equation E.1b introduces a phase shift of 1 sample. This is not true for IIR filters, which will introduce frequency dependent phase shifts. For example, Equation E.1a will introduce a greater delay (measured in samples) for greater input frequencies because it cannot respond quickly enough.

Order-tapping (which refers to the number of inputs) and memory requirements are both related to the ease of implementation in hardware, specifically in an FPGA. The IIR filter in Equation E.1a is first order, as it uses only a single value of the input, x, however, the FIR filter in Equation E.1b is second order, as it uses two values of x. In general, IIR filters are lower order than FIR filters, which dictates their memory and computation requirements. Typically taps will be the last N samples of x, thus, a greater number of taps increases both the required memory and computation power, increasing the difficulty for a hardware implementation.

With the above considerations, an FIR filter was chosen to avoid complications with inconsistent phase shifts. The selected non-weighted moving average filter has a simple hardware implementation as a cascaded integrator-comb filter [81].

E.2 Frequency Modulation Filter Derivations

The implementation of the frequency modulation interferometer in Chapter 5 uses a low-pass filter, which was selected to be a discrete-time moving average. The discrete-time moving average is described by

$$y\left[n\right] = \frac{1}{N}\sum_{m=0}^{N-1} x\left[n-m\right], \tag{E.2}$$

where x is the input signal, N is the number of points included in the averaging window, y is the filter output, and n is an index.

The frequency response, $H(j\omega)$, of a discrete-time filter is the discrete-time Fourier transform (DTFT) of the unit pulse response [91]. The unit pulse response, $h[n]$, is the response to the unit pulse, δ_{k0}, also called the *Kronecker delta function* [91], which is defined as

$$\delta_{k0}\left[n\right] = \begin{cases} 1 & n = 0 \\ 0 & \text{otherwise.} \end{cases} \tag{E.3}$$

The unit pulse response of the moving average filter in Equation E.2 to an input of Equation E.3 is described by

$$h\left[n\right] = \frac{1}{N}\sum_{m=0}^{N-1} \delta_{k0}\left[n-m\right] = \begin{cases} 1/N & 0 \le n < N \\ 0 & \text{otherwise.} \end{cases} \tag{E.4}$$

As mentioned above, the frequency response to a discrete-time system is the DTFT

of the unit pulse response. The DTFT is defined as [91]

$$X_{2\pi}(\omega) = \sum_{n=-\infty}^{\infty} x[n]\, e^{-j\omega n}, \tag{E.5}$$

where ω is the normalized angular frequency. For a signal with a frequency f sampled at a rate f_s, the normalized angular frequency is $\omega = 2\pi f/f_s$ with units of rad/sample.

Equations E.4 and E.5 are combined to produce the frequency response,

$$\begin{aligned} H(j\omega) &= \sum_{n=-\infty}^{\infty} h[n]\, e^{-j\omega n} \\ &= \frac{1}{N} \sum_{n=0}^{N-1} e^{-j\omega n}, \end{aligned} \tag{E.6}$$

which is a finite geometric series. For some real or complex value, r, the sum of a finite geometric series is

$$\sum_{n=0}^{N-1} r^n = \frac{1-r^N}{1-r}. \tag{E.7}$$

Thus, by Equation E.7, Equation E.6 can be rewritten in the form of

$$\begin{aligned} H(j\omega) &= \frac{1}{N} \frac{1-e^{-j\omega N}}{1-e^{-j\omega}} \\ &= \frac{1}{N} \frac{e^{-j\omega N/2}}{e^{-j\omega/2}} \frac{e^{j\omega N/2} - e^{-j\omega N/2}}{e^{j\omega/2} - e^{-j\omega/2}}. \end{aligned} \tag{E.8}$$

From Euler's formula [103], it can be shown for any real a, that $e^{j\omega a} - e^{-j\omega a} = 2j\sin(\omega a)$, by which Equation E.8 can be rewritten as

$$H(j\omega) = \frac{1}{N} \frac{e^{-j\omega N/2}}{e^{-j\omega/2}} \frac{\sin(\omega N/2)}{\sin(\omega/2)}. \tag{E.9}$$

The magnitude of the frequency response, $|H(j\omega)|$, is simplified using $|e^{j\omega a}| = 1$ for any real a, which gives

$$|H(j\omega)| = \frac{1}{N} \left| \frac{\sin(\omega N/2)}{\sin(\omega/2)} \right|. \tag{E.10}$$